MOLECULAR DYNAMICS SIMULATION STUDIES OF IONIC LIQUID ELECTROLYTES FOR ELECTRIC DOUBLE LAYER CAPACITORS

by

Zongzhi Hu

A dissertation submitted to the faculty of
The University of Utah
in partial fulfillment of the requirements for the degree of

Doctor of Philosophy

Department of Materials Science and Engineering

The University of Utah

May 2015

The University of Utah Graduate School

STATEMENT OF DISSERTATION APPROVAL

The dissertation of **Zongzhi Hu**

has been approved by the following supervisory committee members:

Dmitro Bedrov	, Chair	**10/22/2014** Date Approved
Feng Liu	, Member	**10/24/2014** Date Approved
Ling Zang	, Member	**10/24/2014** Date Approved
Valeria Molinero	, Member	**10/24/2014** Date Approved
Jules J. Magda	, Member	**10/24/2014** Date Approved

and by **Feng Liu** , Chair/Dean of

the Department/College/School of **Materials Science and Engineering**

and by David B. Kieda, Dean of The Graduate School.

ABSTRACT

Molecular Dynamics (MD) simulation has been performed on various Electric Double Layer Capacitors (EDLCs) systems with different Room Temperature Ionic Liquids (RTILs) as well as different structures and materials of electrodes using a computationally efficient, low cost, united atom (UA)/explicit atom (EA) force filed. MD simulation studies on two 1-butyl-3-methylimidazolium (BMIM) based RTILs, i.e., [BMIM][BF_4] and [BMIM][PF_6], have been conducted on both atomic flat and corrugated graphite as well as (001) and (011) gold electrode surfaces to understand the correlations between the Electric Double Layer (EDL) structure and their corresponding differential capacitance (DC). Our MD simulations have strong agreement with some experimental data. The structures of electrodes also have a strong effect on the capacitance of EDLCs. MD simulations have been conducted on RTILs of N-methyl-N- propylpyrrolidinium [pyr_{13}] and bis(fluorosulfonyl)imide (FSI) as well as [BMIM][PF_6] on both curvature electrodes (fullerenes, nanotube, nanowire) and atomic flat electrode surfaces. It turns out that the nanowire electrode systems have the largest capacitance, following by fullerene systems. Nanotube electrode systems have the smallest capacitance, but they are still larger than that of atomically flat electrode system. Also, RTILs with slightly different chemical structure such as [$C_n$mim], n = 2, 4, 6, and 8, FSI and bis(trifluoromethylsulfonyl)imide (TFSI), have been examined by MD simulation on both flat and nonflat graphite electrode surfaces to study the effect of cation and anion's chemical structures on EDL structure and DC. With prismatic (nonflat) graphite electrodes, a transition from a bell-shape to a camel-shape DC dependence on electrode potential was observed with increase of the cation alkyl tail length for FSI systems. In contrast, the [$C_n$mim][TFSI] ionic liquids generated only a camel-shape DC on the rough surface regardless of the length of alkyl tail.

Dedicated to all my family members

CONTENTS

ACKNOWLEDGMENTS

The author would like to acknowledge the huge support from Dr. Dmitry Bedrov and Dr. Jenel Vatamanu for their guidance and help during the procedure of this work.

Also, the author would like to give great thanks to the Department of Materials Science and Engineering of University of Utah.

Thanks to the Department of Energy and Army Research Laboratory for financial support under the grants of DE-SC0001912 and W911NF-12-2-0023, respectively.

CHAPTER 1

INTRODUCTION TO ELECTRIC DOUBLE LAYER CAPACITORS

1.1 Electrochemical Energy Storage Devices

In the context of air pollution, global warming and increasing energy demands, the need for efficient, green, renewable (i.e., wind and solar), cheap energy sources and storage devices cannot be overstated, and research in these fields is currently a hot topic. In particular, supercapacitors and Li ion batteries (LIB) have proven to be efficient technologies for high energy density devices. Supercapacitors are typically used for applications requiring short bursts of high power, and the LIBs are more employed in providing long-term energy output. For instance, supercapacitors are used to power up the bass channel in an audio system (*1*) and to give power for emergency doors (*2*). LIBs are commonly used for powering up almost all portable devices (cell-phones, tablets, laser mouse, Bluetooth keyboard, etc.) (*3*), which are needed to last a long time. Furthermore, LIBs can also be utilized to power up larger scale devices such as electric cars or spacecraft components.

1.2 Supercapacitor

Conventional capacitors are comprised of three components: two conductive electrodes, which are usually made of metal, and a separator made by insulating dielectric material. This nonconductive/dielectric material can be glass, a semiconductor, or even vacuum. When electricity source is attached to a capacitor, an electric potential difference is generated between the two conductive plates. Thus a positive charge (+q) is collected across one conductor and a negative charge (-q) on the other. Therefore, unlike resistors, capacitors are a component/device used to store and release energy, not to dissipate energy. Another significant property of a capacitor is that it is able to block direct current while at the same time allowing alternating current (AC) to flow. That is why conventional capacitors are widely applied in the modern integrated circuit industry. The measure of a capacitors strength is called capacitance. Capacitance is defined as the ratio of electric charge (Q) and

potential differences (V) between the two conductive electrodes. The SI unit of capacitance is the Farad (F), and 1 F is equal to 1 coulomb (C)/volt (V).

Due to the fact that conventional capacitors have very low energy densities (*4*), they are usually used in small devices, such as integrated circuit boards. They generally do not meet requirements for large energy-demanding environments. For example, we cannot set up conventional capacitors in electric cars or emergency doors, etc. Therefore, scientists have begun to explore new ways to replace such low energy devices. Supercapacitors, also called Electrochemical Double-Layer Capacitors (EDLCs), in particular, have been introduced that have attracted much attention due to their high energy and power density compared to conventional capacitors. EDLCs can be classified into three kinds: Double-Layer capacitor, Pseudocapacitor, and Hybrid capacitor. In this research, all the EDLCs I refer to are Electric Double-Layer capacitors. Figure 1.1 displays a scheme of EDLCs (*5*).

EDLCs store electrical charge in a similar way to that of conventional capacitors, through accumulating charge near electrode surfaces and without any Faradic reactions (*6*). The difference is that inside an EDLC's cell a distinguishable interface structure between the conductive electrode surface and electrolytic solution is formed. Such interface structures consist of several layers, which are composed with both positive and negative ions, and they are known as Electric Double Layers (EDL). The separation between each layer of EDL is about 5 $\mathring{A}$, and the total thickness of EDL is around 10 to 25 $\mathring{A}$ (*7*), a demonstrated in Figure 1.1.

Such interface structures also create a much larger surface area than those in conventional capacitors, which allows these devices to accommodate more ions, more charge from bulk electrolyte. In other words, a much larger capacitance will be created in EDLCs. EDLCs can generate a much higher energy density than that of conventional capacitors and higher power density than rechargeable batteries (*8*). Figure 1.2 demonstrates the power density as a function of energy density for different electrochemical storage devices. Due to EDLC's many advantages such as higher power density (*9*), higher energy density (*10*), larger electrode surface area with cell voltage (*11*), a highly reversible change/discharge process (*12*), fast charging/discharging at power densities exceeding 1kW kg^{-1} (*13*), low volume change during operation (*14*), being environmentally friendly/safe (*15*), and having excellent low-temperature charge/discharging performance (*16*), they have been accepted as one of the most promising energy storage devices for daily usage.

The first electrochemical capacitors concept with high surface area porous carbon electrodes invented by Becker (*17*) were introduced in 1957. In 1969, SOHIO created another

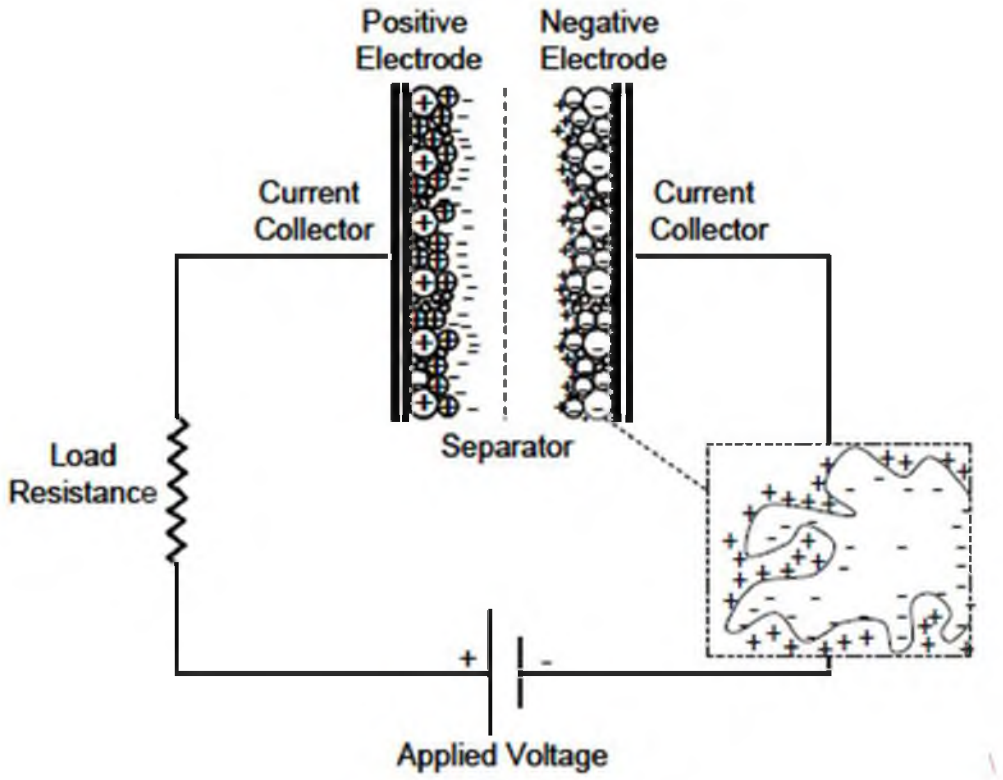

Figure 1.1. Scheme of Electrochemical Double-Layer Capacitor (EDLC).

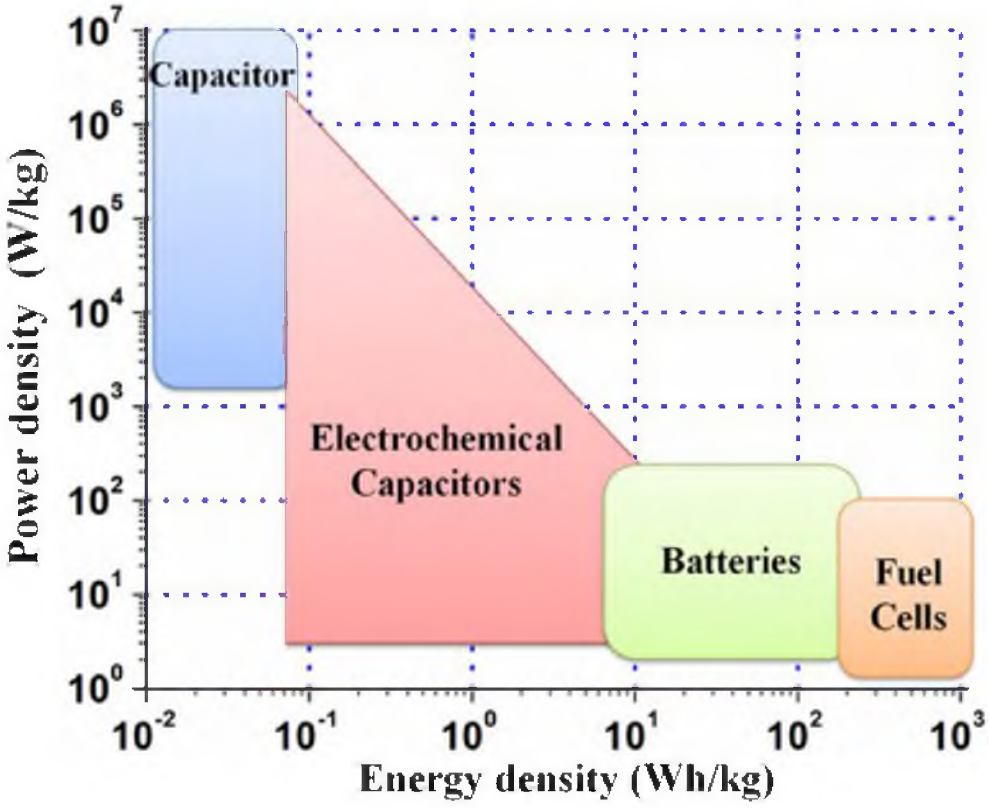

Figure 1.2. Power density as functions of energy density for conventional capacitor, supercapacitor, batteries, and fuel cell.

version of this device called an electric storage apparatus. However, there is no specific evidence to explain the working mechanism of this device in SOHIO's patent (*18*). While electrode materials were improved, electrolytes with better conductivity were synthesized. During 1982, the first EDLC was invented at Pinnacle Research Institute, and they successfully marketed this device under the brand of PRI Ultracapacitor (*19*). Recently, the U.S. Department of Energy (DOE) claimed the equal significance of EDLCs and batteries to underline the important status of EDLCs (*20*). During the past decade, EDLC technology has been extensively examined by scientists both in experimental and theoretical studies (*21,22*), and they have also been identified as the most developed form of the electrochemical capacitor since the mid-19th century (*23*). Also, many electrode materials for EDLCs have been tested by electrochemical communities. One of most popular electrode materials among them is carbon due to its many advantages, such as low cost, availability of raw materials, an easier structure to modify, and a large surface area of up to 2500 m^2/g (*24*).

1.3 Electrolyte: Ionic Liquid

The flammable and volatile conventional organic solvents caused many concerns for modern industries and for individual consumers. The rising safety issues are forcing engineers and manufacturers to find alternative materials, which can take the place of the unsafe organic electrolytes. Recently, Room Temperature Ionic Liquids (RTILs) or low temperature molten salts have attracted much attention. They are experiencing a renaissance in light of their multiple advanced properties as a new generation of electrolyte materials for electric storage devices. These properties include the fact that they possess nonvolatility (*25*), nonflammablity (*26*), high conductivity (*27*), negligible vapor pressure (*28*), high chemical/electrochemical thermal stability (*29*), lower viscosity (*30*), and in some cases hydrophobicity (*31*). Additionally, they have a large electrochemical window (*32*), a broad liquidus range (*33*), and a wide temperature range of operation (*34*). They are also considered to be, in principle, tunable solvents, which have many anions and cations that can be selected. Therefore, one can manage the microproperties of the target electrolytes to obtain the properties that they prefer. RTILs were first discovered in 1914, during World War I, when scientists were trying to explore certain new explosive materials. Instead, they found ionic liquid (*35*). Later, chloroaluminate based ionic molten salts were reported by Hurley, Wier, Wilke, et al. (*36,37*). Most recently, in 1992, Zaworotko has demonstrated some more hydrolytically stable anions that can be utilized in modern industry (*38*).

The reason why they are well-known as room-temperature ionic liquids is because their

liquefying temperatures (melting point) are usually much below 100 °C (*39*). The majority of them are around room temperature or 30 °C (*40*). RTILs usually consist of both organic and inorganic cations and anions such as [$C_n$mim] (imidazolium), [pyr_{13}] (pyrrolidinium), BF_4, PF_6, Bis(trifluorosulfonyl)imide (TFSI), Bis(fluorosulfonyl)imdie (FSI), BR, $B(CN)_4$, etc. Figure 1.3 shows some of the typical ionic cations and anions.

Because of RTILs excellent properties, they are widely utilized in various scientific fields. For example, they are used as green solvent for catalysts, separators, lubricants, and sensors in the textile industry and for heat-transfer fluids for thermal engines, etc., (*41–45*). However, the most well-known practical application for such elite liquids, in particular, is as electrolytes for electrochemical storage devices, such as lithium ion batteries (*46*), lithium polymer batteries (*47*), fuel cells (*48*), photoelectron chemical cells (*49*), and light-emitting electrochemical cells (*50*), and most significantly RTILs have become the most attractive candidate electrolyte materials for EDLCs.

The interfacial structures between RTILs electrolytes and electrodes of EDLCs have been under intense examination during the past decade. This is especially due to the fact that RTILs electrolytes do not consist of any molecules, which make RTILs more structured in bulk electrolytes and near electrodes than that of molecular liquids (*51*). Only ions (cations and anions) are moving around the cell, which are driven by Coulomb interaction, covalent bonds, hydrogen bonds, and van der Waals forces (*52*). Different ion pairs will endow EDLCs with totally different properties. Therefore, by modifying the combinations of different cations and anions, scientists can attain their desired thermodynamic and transport properties for specific applications.

1.4 Electric Double Layers

Due to the relatively large potential differences between the conductive electrode surface, and the "layer-by-layer" structures formed by the ions from electrolyte, they are known as Electric Double Layers (EDLs). Since there is an incomplete understanding of the correlations between EDL structures and capacitance, this field has become a major focus for the scientific community. Understanding the structures of EDL during the electrodes/RTILs interface and designing the best pairs of anions-cations have already become the most interesting parts in this research field. Differential capacitance (DC) as one major way to judge capacitance of EDLCs has been thoroughly studied by our group. DC is defined as

$$DC = \frac{dQ}{dV}$$

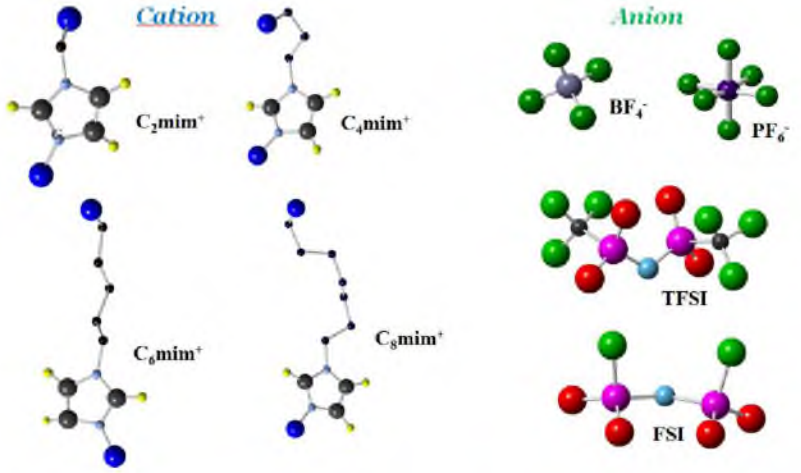

Figure 1.3. Molecular structures of typical ionic liquids.

This is the derivative of the electrode charge per unit of surface area dQ with respect to electrode potential dV. The DC dependence on applied potential between electrodes provides significant insight into and better understanding of the behavior of electrolytes near the conductive electrode surfaces. Each unique EDL structure will normally leave a signature shape of DC. Hence, DC became the main focus and has been widely measured in experimental studies as well as theoretical studies.

1.5 Theoretical Models

Despite the increase of experimental studies on EDLCs, nanoscale understanding of the structures of electrolyte/electrode interface are still constrained. With the increase in theoretical research, especially continuous MD simulation studies, some well-known simulation models have been frequently recited by much of the scientific literature (*50*–55) such as the Helmholtz model (*56*), the Gouy-Chapman model (*57*), and the Kornyshev model (*58*).

1.5.1 Helmholtz Model

In 1853 German scientist Helmholtz create the first simple model to describe charge separation between metallic electrodes and liquid electrolyte solutions. He proposed that the interface between metallic electrodes and solutions could store electric charge (*59*). He believed that the absolute value of charges on the surface of electrodes must be tantamount to the absolute value of charges of cumulated ions near the electrode surface. Such interfacial structures known as the compact layer or the Helmholtz layer are formed by electrostatic or Van der Waals force. Besides the Helmholtz layer, ion density is as same as the bulk density. Thus, there are huge density differences between the Helmholtz layer and the bulk electrolyte. This phenomenon is shown in Figure 1.4. However, such models cannot describe the distance from the electrode surface as a function of ionic charge density very well.

1.5.2 Gouy-Chapman Model

Between 1910 and 1913, Gouy and Chapman proposed that part of the ions beside the Helmholtz layer still need to be considered in the EDL (*60,61*). Therefore, EDL may be found in various thicknesses. In the Gouy-Chapman model, also known as the diffuse double-layer model, ions are treated as a hard sphere with the same radius r, and the charge is situated in the mass-center of the sphere. In bulk electrolytes, half of the ions have positive charge, and the other half have negative charge. Because of this EDL concept, the Gouy-Chapman model is more accurate than the Helmholtz model shown in Figure 1.4 (*62*).

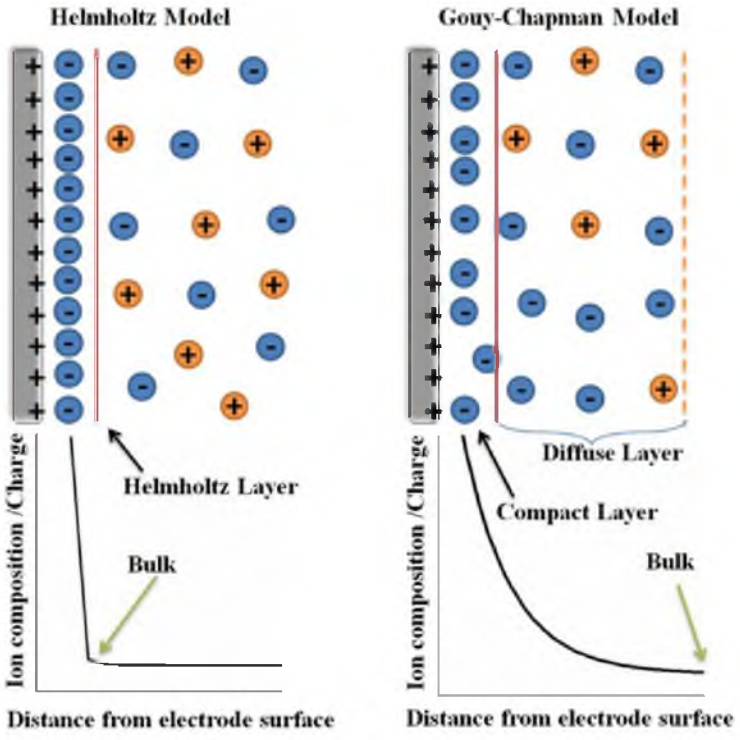

Figure 1.4. Helmholtz model and Gouy-Chapman model.

However, the Gouy-Chapman model has failed to demonstrate the actual capacity-potential curve for most concentrations and measured capacitances much lower than the predict capacitance.

1.5.3 Kornyshev Model

Kornyshev, in 2007, pointed out the shape of DC of RTILs is really different from dilute electrolyte and introduced a mean-field theory (MFT), which is a theoretical method based on the modified Poisson-Boltzmann theory to interpret the shape of the DC for EDLCs, and it demonstrated good agreement with MD simulation results. The main theory of Kornyshev's model is to show how the degree of compressibility in the EDL affects the shape of DC as a function of electrode potential(V). U-shaped DCs are possibly going to be exhibited when the electrolyte steric exclusion near is small (electrode surface is not overcrowded) and ions from the bulk electrolyte can still easily pack onto the surface with increasing potential such that the derivative of electrode charge as function of electrode potential is increasing with potential. That is going to lead to DC having a minimum point (decrease first and then increase). A bell-shaped DC will be the result, when the ions are overcrowded on surface, which when the repulsive Van der Waals force is very strong will make it hard for ions in the electrolyte to pack into clusters (overcrowd electrode surface diminished the exclusion effects). Figure 1.5 shows the mechanism of how the U-shaped DC and bell-shaped DC curves are formed. Additionally, Kornyshev also pointed out that when the number of the cations is much larger than the number of anions, the DC maximum value will shift positively from the PZC (*63*).

1.6 Molecular Dynamics (MD) Simulation

There are countless possibilities of cation-anion combinations (ionic pairs) that can be made for RTILs electrolytes. However, utilizing experimental methods/characterizations to study the very thin, several angstroms thickness of EDL formed by electrolytes is quite challenging. Therefore, detailed, atomic level MD simulation studies can help scientists determine the complexity of nanoscale physics happening inside the EDL.

1.6.1 MD Simulation Methodology

Molecular Dynamics (MD) simulation is a promising theoretical tool. It is well suited for exploring structure, transport, thermodynamics, interfacial behaviors, and other properties for various ionic liquids (ILs) and their mixtures. Numerous ILs have been investigated, during the past 2 decades, including imidazolium, pyrrolidinium, triazolium, tetraalkylphos-

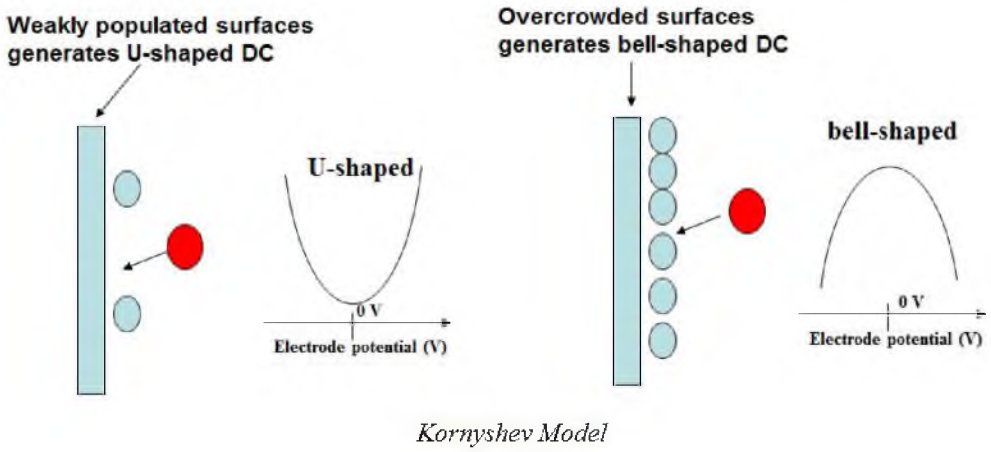

Figure 1.5. U-shaped DC and bell-shaped DC in Kornyshev model.

phonium, phosphonium, and tetraalkylammonium, cations, BF_4, PF_6, FSI, TFSI, and anions. MD simulation studies have provided many insights and evidence to help the research community to fundamentally understand what is going on inside EDL.

Typically, at a constant temperature, simulations are conducted with constant voltage between two conductive electrodes. We modified the electrostatic energy and electrode charge such that each atom on the electrodes' dialed in electrostatic potentials are remain constant (*64*). The value of charge on each atom on the electrodes is simulated as a Gaussian distribution located on the center of each atom (*65*).

$$\rho_i(r - R_i) = q_i(\frac{\epsilon_i^2}{pi})^{3/2} exp(-\epsilon_i^2 |r - R|^2)(1)$$

where ρ_i(r- R_i) is the electric charge density on the atom i of electrode situated at the position R_i, and $1/\epsilon_i$ is the width of distribution. The total electrostatic energy of the system that consists of the left and right electrode and conductive electrolyte in the middle is given by

$$U = \frac{1}{2}\sum_k \sum_{ij} \frac{q_i q_j}{|R_{ij} + kL|} - \frac{1}{2}\sum_k^* \sum_{ij} \frac{q_i q_j}{|R_{ij} + kL|} erfc(\epsilon_{ij} |R_{ij}| + kL) + \sum_i (q_i^2/\sqrt{\pi})\epsilon_{ij}\delta(i, G)(2)$$

where R_{ij} s the vector of distance between the atom i and atom j in the initial box, k is the multiplicity of the initial box which the initial box k equal to 0, and kL is the multiplicity factor for the distance vector R_{ij}. The * over the summation is a restriction label that demonstrates the summation over ion pairs i and j and is constrained as i j when they are in the initial box (k = 0). The Gaussian cross-widths $1/_{ij}$ is define as

$$\frac{1}{\epsilon_{ij}^2} = \frac{1}{\epsilon_i^2} + \frac{1}{\epsilon_j^2}(3)$$

In the last term of equation 2, the (i,G) is zero for the charge follow Gaussian distribution or point charge, and Gaussian self-interactions $\sum_i (q_i^2/\sqrt{\pi})\epsilon_{ij}$will be excluded if the charges are not follow Gaussian distribution. Usually we solve the electrostatic energy, which is the first term of equation 2 by applying the standard Ewald summation method specific for a 2D-periodic box system of point charge with an expedient Smooth Particle Mesh Ewald (SMPE) version (*66–69*). When the distance between two ions is beyond the cut-off value, 9 to 10, the second term of equation 2 can be essentially neglected; hence, the error function of equation 2 was approximately as a short range (*70*).

$$\frac{1}{2}\sum_k \sum_{ij} \frac{q_i q_j}{|R_{ij} + kL|} - \frac{1}{2}\sum_k \sum_{ij} \frac{q_i q_j}{|R_{ij} + kL|} erfc(\epsilon_{ij} |R_{ij}| + kL)$$

$$\approx \frac{1}{2}\sum_{k}\sum_{ij}\frac{q_i q_j}{|R_{ij}+kL|} - \frac{1}{2}\sum_{k}\sum_{ij}\frac{q_i q_j}{|R_{ij}+kL|}erfc(\epsilon_{ij}\,|R_{ij}|)(4)$$

Equation 4 indicates that the electrode charge following Gaussian distribution contributes to the total electrostatic energy with an extra short term as shown in the right side of equation 4, but if the Gaussian width is more than 1/3 of the short-ranged cut-off, the left side of the equation 4 cannot be considered as short-ranged, and the Ewald summation procedures can be utilized to calculate its long-ranged contribution.

For each time step, we have to modify the electrode charge such that atoms on the electrode receive the same electrostatic potential V_i^0dialed on the conductive electrodes. Therefore, during the simulation, we can control the electrostatic potential difference. Modifying electrode charges are achieved by changing the total electrostatic energy as

$$U_t = U - \sum_{i=1}^{v} q_i V_i^0(5)$$

where $\sum_{i=1}^{v} q_i V_i^0$ is the required work to generate the electrode charge q_i, i = 1 to v (*71*). When k = 1 to v, the following system equations are given by

$$\sum_{i=1}^{v}\frac{q_i}{|R_{ik}|}(erfc(1/\gamma_{ik}^2 - 1/\epsilon_{ik}^2)^{-1/2}\,|R_{ik}|) - erfc(\epsilon_{ik}\,|R_{ik}|))$$

$$+\frac{1}{A}\sum_{i=1}^{v} q_i \sum_{k}\int \mathrm{d}h\Gamma(k,h)exp(ikR_{xy,i} + ihZ_i)$$

$$-\sum_{i=1}^{v} q_i\frac{2\alpha}{\sqrt{\pi}} + \sum_{i=1}^{v} q_i\frac{2\epsilon_{ii}}{\sqrt{\pi}}\delta(i,G)+$$

$$\frac{1}{A}\sum_{i=1}^{v} q_i(-\frac{\sqrt{\pi}}{\alpha}exp(-(\alpha Z_{ik})^2)) - Z_{ij}\pi erf(\alpha Z_{ik})$$

$$= -\sum_{j=v+1}^{N}\frac{q_j}{|R_{jk}|}(erfc(1/\gamma_{ik}^2 - 1/\epsilon_{ik}^2)^{-1/2}\,|R_{ik}|) + erfc(\epsilon_{ik}\,|R_{ik}|))$$

$$-\frac{1}{A}\sum_{i=1}^{v} q_i \sum_{k}\int \mathrm{d}h\Gamma(k,h)exp(ikR_{xy,i} + ihZ_i)$$

$$-\frac{1}{A}\sum_{i=1}^{v} q_i(-\frac{\sqrt{\pi}}{\alpha}exp(-(\alpha Z_{ik})^2)) - Z_{ij}\pi erf(\alpha Z_{ik}) + V_i^0(6)$$

where α is the Ewald screening parameter, A is the cross section of the system, k is the Fourier space vector, h is the integration step along the nonperiodic z-direction, and indices i and k run over the variable charges while j runs for fixed non electrode charges. Z_i is the

location charge i along the z-direction, and Z_{ij} is the distance between charge i and j along the z-direction. Electrode charges q_i, i = 1 to υ, are the unkowns; γ_{ij} is defined as

$$\frac{1}{\gamma_{ik}^2} = \frac{1}{\alpha^2} + \frac{1}{\epsilon_i^2} + \frac{1}{\epsilon_j^2}$$

and the Fourier factor Γ(k,h) is defined as

$$\Gamma(k,h) = \frac{1}{|k|^2 + h^2} exp(-\frac{|k|^2 + h^2}{4\alpha^2})$$

1.6.2 Polarizability

Electric polarizability is the property of a given electrostatic distribution (such as the 1s of an electron cloud) to modify itself in response to interaction with an external charge or field. For example the electron cloud distribution in a 1s orbital is spherical. If we bring a test charge (e.g., positive) close to the 1s electron cloud, we expect that the symmetry of the 1s cloud will be perturbed by the test charge, such that a net displacement of the electron cloud toward the positive charge is expected. This kind of perturbation of the electron cloud is called polarization. Figure 1.6 demonstrates that the initial charge distribution of spherical symmetry is polarized by the presence of a test charge.

In MD simulations, the polarizabilities introduced in the expression of energies and forces, a many-body term, and the polarizabilities are modeled in 3 different approaches: i) induced dipoles, ii) drude oscillators, and iii) fluctuating charges.

In the case of induced dipoles, on each polarizable atom we attach a fluctuating dipole, which can change its direction and magnitude as a response to the total electrostatic field. The electrostatic energy is given by

$$E = \frac{1}{2}\frac{1}{4\pi\epsilon_0}\sum_{k}\sum_{i\neq j if k=0,i,j=1}^{N}(q_i + \mu_i\bigtriangledown_i)\cdot(q_j + \mu_i\bigtriangledown_i)\frac{1}{r_{kij}} - \frac{1}{2}\sum_{i\neq 1}^{N}(\frac{\mu_i\cdot\mu_i}{\alpha_i})$$

The first term is the electrostatic energy of a system with point charges and dipoles, and the second term is the polarization energy given by the magnitude of induced dipoles. The dipoles in the first term are induced dipoles.

The indexes i and j are labeling the atom identity, while the index k = (kx,ky,kz) is labeling the replicated periodic boxes constructed to mimic a bulk-like system. The q_i is the point charge on atom i, the i is a 3D vector representing the induced dipole on atom i, ε_0 the vacuum permittivity, and r_{kij} the distance between atoms i and j. The α_i is the electronic polarizability of a given atom i, and it is defined as the ratio between the induced dipole generated and the required electrostatic field E to generate the induced dipole: $\mu_i = \alpha_i E$.

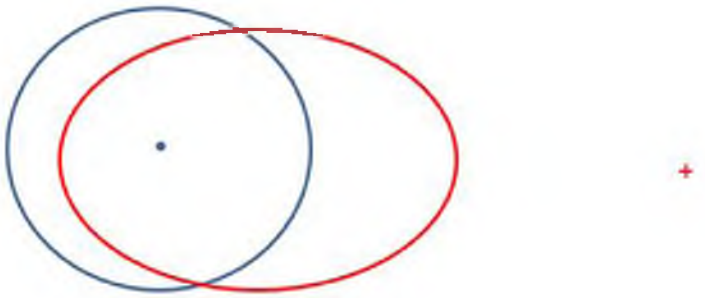

Figure 1.6. The initial charge distribution of spherical symmetry (blue circle) is perturbed (or polarized) by the presence of a test charge (see red ellipse).

The induced dipoles are computed at each MD simulation step by minimizing the electrostatic energy with respect to the induced dipoles.

$$\frac{\delta U}{\delta d_i^x} = 0; \frac{\delta U}{\delta d_i^x} = 0; \frac{\delta U}{\delta d_i^z} = 0(3)$$

Therefore, in order to compute the induced dipoles, we need 3*N equations, where N is the number of atoms with nonzero polarizability. The system of equations above are solved iteratively, and typically they require up to 6 to 12 iterations to converge, and therefore the polarizable force fields are computationally more expensive than nonpolarizable ones.

Drude oscillation represents polarization by inducing a massless auxiliary charged particle attached to every polarizable atom through a harmonic spring (*72*). The position of the charged particle is adjusted to its local energy minima for any configuration of atoms in a certain system.

Part of the total energy associated with the induced dipoles generated as the molecule is under the effect of an external field is depicted in this way:

$$U = U_{self} + U_{el}$$

where

$$U_{self} = \frac{1}{2kd_2}$$

Fluctuating charges (FQ) use flexible/fluctuant point charges to represent the polarizabilities. The charges are located on atomic sites in the molecule, and their value is calculated such that it minimizes the electrostatic interaction energy. For the isolated molecule, the energy of this molecule is expanded to a second order in the partial charge:

$$U(Q_i) = U(0) + x_i^{\sim o} Q_i + \frac{1}{2} J_{ii}^o Q_i^2(5)$$

where U0(r) provides the charge independent contribution, x_i^0 is the electronegativity, and J_i^0 is the hardness of the electronegativity; both x_i^0 and J_i^0 are in principle characteristic of the atomic site i. Within the FQ model, the electrostatic energy of the system is formed by many interacting molecules and is defined as

$$U = \sum_{\alpha=1}^{M} \sum_{i \in \alpha} U_{0i} \sum_{\alpha=1}^{M} \sum_{i \in \alpha} x_i^0 q_i + \frac{1}{2} \sum_{\alpha=1}^{M} \sum_{i \in \alpha} J_{ii}^o Q_i^2 + \frac{1}{2} \sum_{\alpha=1}^{M} \sum_{i \in \alpha} \sum_{\beta=1}^{M} \sum_{i \in \beta}^{i \neq j} J_{ij}(r_{ij}) q_i q_j(6)$$

where α and β label the molecule identity, i and j label the atomic identity, and J_{ij} (r_{ij}) is the coulomb overlap integral, given by

$$J_{ij}(r_{ij}) = \int dr_i dr_j |\varphi_{ni}(r_i)|^2 \frac{1}{|r_{ij}|} |\varphi_{ni}(r_i)|^2(7)$$

φ_{ni} (r_i) is Slater [?]*73*) ns atomic orbitals of atom i, rij is the distance between atoms i and j. The overlap integrals J_{ij} (r_{ij}) quickly decay to classical electrostatic term 1/rij if rij is

larger than a few Angstroms (i.e., beyond 2 to 3). The term J_{ij} (r_{ij}) can either be calculated from ab-initio at shorter distances (while considered equal to 1/rij at larger distances) or approximated by from the self-terms J_{ii} (0) according to the Patel expression:

$$\lambda = J_{ii}^2 + J_{jj}^2$$

$$J_{ij}(r_{ij}) = \frac{1}{2}\lambda/\sqrt{1+\lambda^2 r_{ij}^2} \quad (8)$$

The electronegativities x_i^0 and the hardness of the electronegativity J_i^0 are computed either from ab-initio computations or fitted from empirical data. The constant term

$$\sum_{\alpha=1}^{M}\sum_{i\in\alpha} U_{0i}$$

can be set to zero (i.e., define our level of zero for energy). Then all we need in order to compute the flexible charges q_i is to optimize the total electrostatic energy with respect to the fluctuant charges q_i.

It has been previously shown that nonpolarizable force fields can fairly accurately reproduce some structural properties in bulk or interface, such as density and heat of vaporization (*74*).

Then why do we need polarizable force fields in simulations? At a qualitative level, polarizablities capture a more realistic description of the charge distribution around atoms/molecules, specifically, if it shows that the charge distribution is not fixed, but rather it can be modified, as a result of the electrostatic environment. There could be problems when the polarizablities must be included in order to capture the physics, even at a qualitative level. For example in order to describe the behavior of a nonpolar molecule in the electric field, we must account for the polarizabilities.

At a quantitative level, the polarizabilities improve the predictions of dynamic properties and local structure. For example, the previous work (*75*) conducted by Oleg Borodin on Li salts in various solvents proved that the dynamic properties (i.e., diffusion coefficients) could be reproduced accurately with polarizable force fields. Typically, nonpolarizable force fields predict smaller diffusion coefficients than the polarizable force fields. Also, in the case of small radius ions (such as Li^+ or even Na^+), which strongly polarize their environment, the correct local structure around Li^+ (i.e., coordination number) can be reproduced only with polarizable force fields (*76*). Nonpolarizable force fields produce larger coordination numbers of solvents or anions around Li^+. Faster diffusion and lower coordination numbers observed with polarizable force-fields could be intuitively understood as follows: if the charge fluctuates, then there could be instances when the effective electrostatic attractions

could be weakened, as compared to fixed (nonpolarizable) charges. In such instances, the atoms can more easily escape their first coordination shell effectively increasing the diffusion coefficient and decreasing the 1st shell coordination numbers.

1.7 MD Simulation Force Field

There are two major force fields for MD simulations; one is the nonpolarizable force field, the other is the polarizable field. The main difference between these two is that the nonpolarizable force field does not consider electron polarizations during the calculation and thus loses the accuracy of describing the physics that occurred inside the system. Therefore, nonpolarizable models are much faster than polarizable models. With years of effort, our group has developed and validated a transferable Atomistic Polarizable Potential for Liquids, Electrolytes, and Polymers (APPLE&P) (*77*) force field database, which can accurately predict a wide set of commonly use RTILs properties. During the developing of APPLE&P, our group used the same repulsion-dispersion, nonbonded parameters for identical atoms between various complexes and chemical conditions and demonstrated that this force field has a higher degree of transferability to much of our work. However, the polarizable model needs a long time to run the simulations and is not economical. Therefore, in order to seek a more efficient and accurate way to predict the properties of EDLCs, a computationally efficient united atom/explicit atom (UA/EA) force field was tested and developed by our group. Such models combine both nonpolarizable force fields and polarizable force fields, in which the alkyl $-CH_2-$ and CH_3- groups are represented as united atoms (one atom), while all the other atoms, such as imidazolium cyclic structure and anion, are described explicitly with data from APPLE&P. All the work in this thesis use the united atom/explicit atom force field.

1.8 MD Simulation Details

The simulation's setup consisted of RTILs electrolyte confined between two electrodes, which are treated as conductors as shown in Figure 1.7(a). The electrostatic potentials were imposed on the electrodes. The value on one electrode is $\pm\Psi_0/2$, which is allowing to constrain the total potential difference between two electrodes to be Ψ_0. The dialed potential only act over short distances near the electrode, which is around 10 $\mathring{A}$ to 30 $\mathring{A}$. The electrolyte near the electrode surface tries to screen out the influence of the field, as a result a series of layer formed near the electrode. We called it electric double layers (EDL). Figure 1.7(b) showed the EDL structures near the electrode surface. There are strong oscillations happened for the layers of EDL near the conductive electrodes. With the

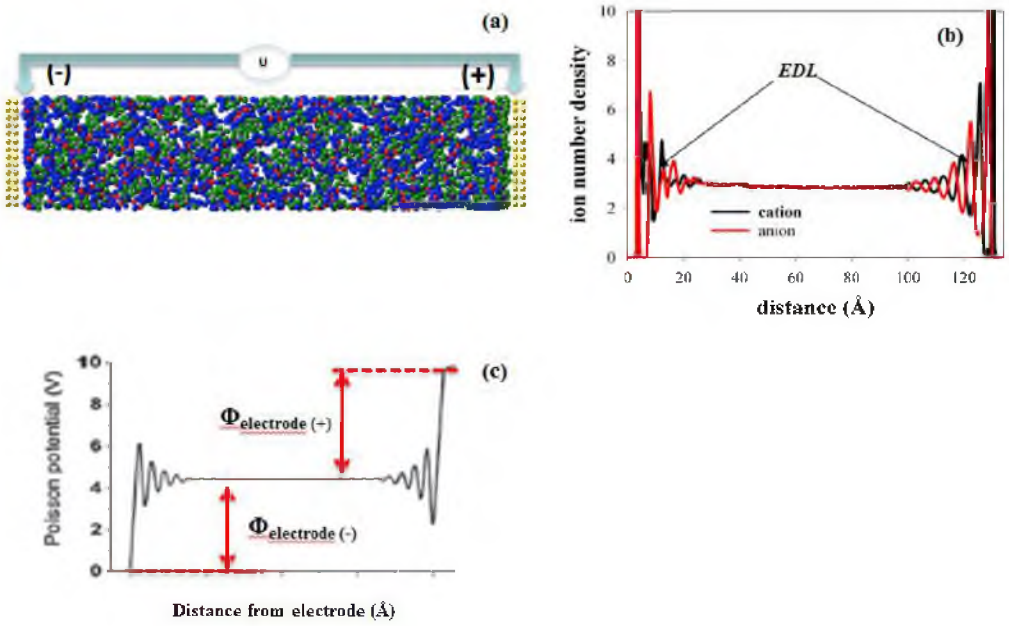

Figure 1.7. Simulation details (a) simulation box setup, (b) EDL formation, (c) Poission potential.

layers become thinker, the oscillations are starting to get weak. In the bulk electrolyte the oscillations are mostly diminished. The degree of bulk electrolyte oscillation also provides us the evidence to justify whether the system is received enough equilibrium times or not. The smoother the bulk density is, the closer a system achieves equilibrium. The electrolyte is represented by 300 to 500 ionic pairs, which is large enough to allow bulk electrolyte phase in the middle of the simulation cell. The electrode potential is defined as the difference in Poisson potential between the electrode surface and in the middle of the bulk electrode (Figure 1.7(c)). The formula for electrode potential is below

$$U_{electrode} = U_{EDL} = \Phi_{electrode} - \Phi_{bulk}$$

The electrode charges and the spatial distribution of charge in electrolyte were calculated. From the profiles of spatial charge distribution $\rho(z)$ across the simulation box where z is the length of the simulation box (the direction perpendicular to electrode surfaces), we calculated the Poisson potential $\phi(z)$:

$$\frac{d^2\phi(z)}{dz^2} = -\rho(z)/\varepsilon_0$$

where ε_0 is the vacuum permittivity.

Electrode charges were modeled as Gaussian distributed with widths of 0.5A. The nonbonded van der Waals interaction were calculated within a spherical cut-off of 10 A. The temperatures of my research were controlled by the Nose-Hoover thermostat with a coupling time constant of 0.1 ps. The equations of motion were integrated with a reversible multiple time step r-RESP algorithm (*78*).

Figure 1.8(a) shown a comparison of electrode charge as a function of electrode potential for three independent trajectories at 393 K of [C_2mim][FSI] system on prismatic graphite surface. These trajectories are 12.5 ns, 25 ns, and 50 ns, respectively. They generated virtually identical curved for electrode charge. However, the differential capacitance (DC), the numerical derivatives of the data in Figure 1.8(a), is the value we are interesting in. Figure 1.8(b) shown the corresponding DC of Figure 1.8(a) data within these three independent trajectories. The longer the simulation run, the better EDL formation near the charge electrode which lead to a more realistic DC.

1.9 DC Results from Experiments

There are many factors, such as electrolyte chemical structures, conductive electrode surface topography, shape of electrodes (nanotube, fullerene, nanowire, etc.), and electrode-electrolyte polarizabilities. Even temperatures can potentially alter the overall shape of DC.

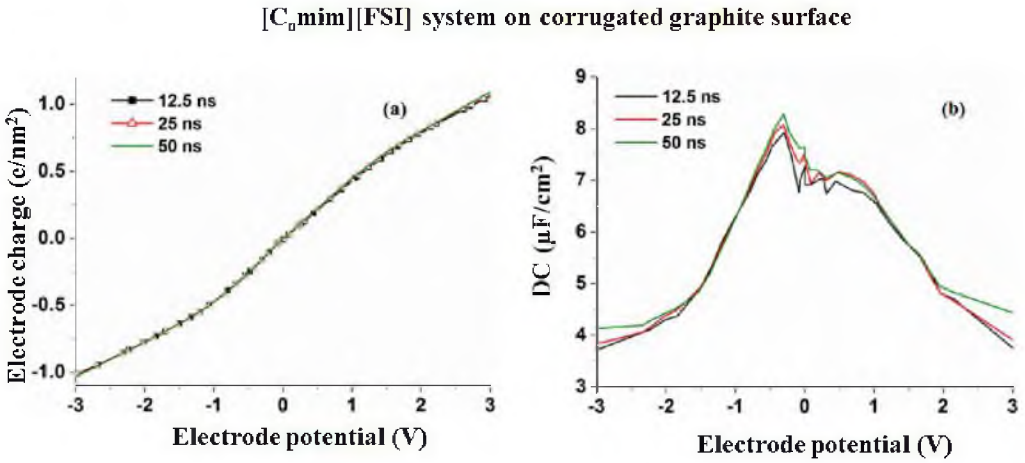

Figure 1.8. Electrode charge/DC as a function of electrode potential for three independent trajectories at 393 K of C_2mim/FSI system on prismatic graphite surface.

While some experimental DC results can be explained and interpreted through theoretical models, several current experimental studies demonstrate some disagreements with other theoretical studies. For example, Su et al. reported their study on [BMIM][BF_4] RTILs on gold (001) electrode surfaces with a very large value of bell-shaped DC of 25 μF cm^{-2} (*79*). However, with similar RTILs of [BMIM][PF_6] near the same gold electrode, Lockett et al. reported their DCs value to be only 6 to 7 μF cm^{-2} (*80*). Lin et al. studied the same RTIL on a gold (111) surface and found that it only has a maximum DC value of 2.2 μF cm^{-2} (*81*). High DC was also observed by Silver et al. with [BMIM][PF_6] electrolyte near a glassy carbonate electrode and Alam et al. with [EMIM][BF_4] on gold (111) surface (*82,83*). In contrast, a system with same electrolyte and gold electrode, Lockett et al. reported their DC only to be around 4 to 8 μF cm^{-2} (*84*), and Lewandowski et al. reported an even lower DC with a value of 3.1 μF cm^{-2} (*85*).

As I mentioned previously, the value of DC is determined by a couple of factors. According to previous work (*86*) and simulation models, such huge DC differences cannot be attained only through changing the structure of the electrodes or replacing ions with similar cations or anions. Those inconsistent phenomenon from experimental results are introducing many questions in the research community, and proper theoretical studies to verify those contradictory experimental works are required.

1.10 Overview of Previous Simulation Studies

Dr. Dmitry Bedrov's group has examined many RTILs with different configurations of electrodes, such as atomically flat, corrugated graphite at different temperatures. Popular RTILs such as pyr_{13}^+, $C_n mim^+$ (n = 2, 4, 6, 8), BF_4^-, PF_6^-, TFSI, FSI have been systematically studied, and how they affect the performances of EDLCs were demonstrated in many our previous works (*63,68,80,85–88*). For example, during the study of [pyr_{13}][FSI] and [pyr_{13}][TFSI] RTILs on atomically flat graphite electrodes, we found that the smaller size of FSI did not significantly enhance DC. It was only 30% higher than that of [pyr_{13}][TFSI], even if FSI anion was closer to the electrode surface than TFSI anion, when they are attracted by the opposite electrode potential. Also, the rate of the absorption is much faster for FSI anions than that of TFSI.

The electrode surface topography has a huge effect on EDLCs capacitance (*87,88*). We found that DC for atomically flat graphite electrode surface systems have similar, almost constant values. In contrast, prismatic or corrugated graphite electrode systems usually resulted in signature bell-shaped DCs with a larger enhanced value of up to 9.5 μF cm^{-2}.

How do the various materials influence EDLCs capacitance? We discussed this in Chapter 2. Graphite electrodes (basal and prismatic topography) and gold electrodes were used in this study for comparison purposes. EDL structures were analyzed and their correlations with DC were illustrated. Also, the comparison of electrode surfaces with and without chemisorption has been investigated.

Besides the effects of different materials as electrodes on capacitance, different structures/shapes of electrodes are another significant factor that can influence the capacitance of EDLCs. This topic was thoroughly discussed in Chapter 3. Different structures, such as single carbon nanowires, fullerenes (C_{20}, C_{60}) and nanotubes were examined, and their corresponding integral capacitance (IC) was compared with atomically flat electrode systems, and correlation between EDL structures and IC was demonstrated in this chapter.

Finally, in Chapter 4, after we learned the effect of different materials and shapes of electrodes on the EDLCs capacitance, we focused on another significant part of the EDLC, the electrolytes. In this chapter, a systematic comparative study of DC and the EDL structures formed near atomically flat and corrugated surfaces with two similar series of electrolytes: [$C_n$mim][FSI] and [$C_n$mim][TFSI] (n = 2, 4, 6, 8) has been conducted. How the length of the alkyl tail of a cation affects the capacitance as well as how the different chemical structures of an anion with the same cation influences their corresponding DC was demonstrated. The correlation between EDL structures and the shape of DC was investigated as well.

1.11 References

[1] Liu, Y.; Zhang, Y.; Ma, G.; Wang, Z.; Liu, K.; Liu, H. *Electrochim. Acta* **2013**, *88*, 519–525.

[2] Aedo, I.; Yu, S.; Daz, P.; Acua, P.; Onorati, T. *Sensors (Switzerland)* **2012**, *12* (6), 7804–7827.

[3] Rosciano, F.; Pescarmona, P. P.; Houthoofd, K.; Persoons, A.; Bottke, P., Wilkening, M. T. *Phys. Chem. Chem. Phys.* **2013**, *15* (16), 6107–6112.

[4] Fukuhara, M.; Sugawara, K. *Nanoscale Res. Lett.* **2013**, *9* (1), 1–6.

[5] Lee, T.; Yun, T.; Park, B.; Sharma, B.; Song, H. K.; Kim, B. S. *J. Mater. Chem.* **2012**, *22* (39), 21092–21099.

[6] Nozu, R.; Iizuka, M.; Nakanishi, M.; Kotani, M. *J. Power Sources* **2009**, *186* (2), 570–579.

[7] Salitra, G.; Soffer, A.; Eliad, L.; Cohen, Y.; Aurbach, D. *J. Electrochem. Soc.* **2009**, *147* (7), 2486–2493.

[8] Xiong, S.; Yang, F.; Jiang, H.; Ma, J.; Lu, X. *Electrochim. Acta* **2012**, *85*, 235–242.

[9] Yin, Y.; Liu, C.; Fan, S. *J. Phys. Chem. C* **2012**, *116* (50), 26185–26189.

[10] Brown, B.; Swain, B.; Hiltwine, J.; Brooks, D. B.; Zhou, Z. *J. Power Sources* **2014**, *272*, 979–986.

[11] Staiti, P.; Lufrano, F.; *J. Electrochem. Soc.* **2005**, *152* (3), A617–A621.

[12] Bakhmatyuk, B. P.; Venhryn, B.Ya.; Grygorchak, I.I.; Micov, M. M.; *J. Power Sources* **2008**, *180* (2), 890–895.

[13] Ranjusha, R.; Sajesh, K. M.; Roshny, S.; Lakshmi, V.; Anjali, P.; Sonia, T. S.; Sreekumaran, N. A.; Subramanian, K. R. V.; Nair, S. V.; Chennazhi, K. P.; Balakrishnan, A. *Microporous Mesoporous Mater.* **2014**, *186*, 30–36.

[14] Zhou, G. M.; Wang, D. W.; Li, F.; Zhang, L. L.; Weng, Z.; Cheng, H. M.; Tan, X. *New Res. Carbon Mater.* **2011**, *26* (3), 180–186.

[15] Brandt, A.; Pohlmann, S.; Varzi, A.; Balducci, A.; Passerini, S. *MRS Bull.* **2013**, *38* (7), 554–559.

[16] Lv, Y.; Zhang, F.; Dou, Y.; Zhai, Y.; Wang, J.; Liu, H.; Xia, Y.; Tu, B.; Zhao, D. *J. Mater. Chem.* **2012**, *22* (1), 93–99.

[17] Pang, H.; Shi, Y.; Du, J.; Ma, Y.; Li, G.; Chen, J.; Zhang, J.; Zheng, H.; Yuan, B. *Electrochim. Acta* **2012**, *85*, pp. 256-262.

[18] Zhang, S. W.; Chen, G. Z. *Energy Mater.* **2008**, *3* (3), 186–200.

[19] FDK, Corporate Information, FDK Historie 2000s. http://www.fdk.com/company_e/ayumi2000-e.html

[20] Liu, H.; Gan, W. P.; Huang, B.; Shi, X.; Liu, J. Y.; Zheng, F. *J. Cent. South Univ.* **2009**, *40* (6), 1546–1551.

[21] Dai, S.; Xi, Y.; Hu, C.; Liu, J.; Zhang, K.; Yue, X.; Cheng, L. *J. Mater. Chem. A* **2013**, *1* (48), 15530–15534.

[22] Shim, Y.; Jung, Y.; Kim, H.J. *J. Phys. Chem. C* **2011**, *115* (47), 23574–23583.

[23] Huang, Y.; Candelaria, S. L.; Li, Y.; Li, Z.; Tian, J.; Zhang, L.; Cao, G. *J. Power Sources* **2014**, *252*, 90–97.

[24] Ma, M.; Zhao, Q.; Tong, Z. *J. Fiber Bio. Info.* **2013**, *6* (3), 277–283.

[25] Santhosh B. S.; Nakanishi, T. *Chem. Commun.* **2013**, *49* (82), 9373–9382.

[26] Sivakkumar, S. R.; Howlett, P. C.; Winther. J. B.; Forsyth, M.; MacFarlane, D. R. *Electrochim. Acta*, **2009**, *54* (27), 6844–6849.

[27] Shaplov, A. S.; Goujon, L.; Vidal, F.; Lozinskaya, E. I.; Meyer, F.; Malyshkina, I. A.; Chevrot, C.; Teyssie, D.; Odinets, I. L.; Vygodskii, Y. S. *J. Polym. Sci., Part A: Polym. Chem.* **2009**, *47* (17), 4245–4266.

[28] Lakshmi, B. A.; Sindhu, S.; Venkatesan, S. *Int. J. ChemTech Res.* **2013**, *5* (3), 1129–1137.

[29] Ignat'ev, N. V.; Willner, H.; Sartori, P. *J. Fluorine Chem.* **2009**, *130* (12), 1183–1191.

[30] Strehmel, V.; Wishart, J. F.; Polyansky, D. E.; Strehmel, B. *ChemPhysChem* **2009**, *10* (17), 3112–3118.

[31] Tanimura, A.; Kovalenko, A.; Hirata, F. *Langmuir*, **2007**, *23* (3), 1507–1517.

[32] Wang, W.; Guo, S.; Bozhilov, K. N.; Yan, D.; Ozkan, M.; Ozkan, C. S. *Small* **2013**, *9* (21), 3714–3721.

[33] Chen, R.; Wu, F.; Li, L.; Xu, B.; Qiu, X.; Chen, S. *J. Phys. Chem. C* **2007**, *111* (13), 5184–5194.

[34] Liang, L. H.; Gan, Q.; Nancarrow, P. *Appl. Mech. Mater.* **2014**, *448*, 765–770.

[35] Garcia, B.; Lavalle, S.; Perron, G.; Michot, C.; Armand, M. *Electrochim. Acta* **2004**, *49* (26), 4583–4588.

[36] Hurley, F. H.; Wier, T. P. *Electrochem. Soc.* **1951**, *98*, 203.

[37] Wilkes, J. S.; Levisky, J. A.; Wilson, R. A.; Hussey, C. L. *J. Chem. Soc. Commun.* **1982**, *21*, 1263.

[38] Wilkes, J. S.; Zaworotko, M. J. *J. Chem. Soc. Commun.* **1992**, 965.

[39] Plaquevent, J. C.; Levillain, J.; Guillen, F.; Malhiac, C.; Gaumont, A. C. *Chem. Rev.* **2008**, *108* (12), 5035–5060.

[40] Ooue, R.; Oosaki, S.; Yajima, S.; Kimura, K. *Bunseki Kagaku* **2008**, *57* (8), 619–624.

[41] Raula, M.; Biswas, M.; Mandal, T.K. *RSC Adv.* **2014**, *4* (10), 5055–5064.

[42] Fang, L. F.; Shi, J. L.; Zhu, B. K.; Zhu, L. P. *J. Membr. Sci.* **2013**, *448*, 143–150.

[43] Heller, I.; Chatoor, S.; Mnnik, J.; Zevenbergen, M. A. G.; Dekker, C.; Lemay, S. G. *J. Am. Chem. Soc.* **2010**, *132* (48), 17149–17156.

[44] Pingale, N. D.; Jawale, L. S. *Int. Dyer,* **2006**, *191* (4), 13–15.

[45] Xu, K.; Ruan, B.; Meng, H. *Appl. Therm. Eng.* **2014**, *73* (1), 349–354.

[46] Cao, J.; Wang, L.; Fang, M.; Shang, Y.; Deng, L.; Yang, J.; Li, J.; Chen, H.; He, X. *Electrochim. Acta* **2013**, *114*, 527–532.

[47] Daz, M.; Ortiz, A.; Ortiz, I. *J. Membr. Sci.* **2014**, *469*, 379–396.

[48] Ratieuville, V.; Fatyeyeva, K.; Chappey, C.; Rogalskyy, S.; Tarasyuk, O.; Marais, S. *Adv. Mater. Res.* **2013**, *747*, 477–480.

[49] Harati, M.; Jia, J.; Giffard, K.; Pellarin, K.; Hewson, C.; Love, D. A.; Lau, W. M.; Ding, Z. *Phys. Chem. Chem. Phys.* **2010**, *12* (46), 15282-15290.

[50] Sunesh, C. D.; Chandran, M.; Ok, S.; Choe, Y. *Mol. Cryst. Liq. Cryst.* **2013**, *584* (1), 131–138.

[51] Konig, D.; Richter, K.; Siegel, A.; Mudring, A. V.; Ludwig, A. *Adv. Funct. Mater.* **2014**, *24* (14), 2049–2056.

[52] Strehmel, V.; Berdzinski, S.; Rexhausen, H. *J. Mol. Liq.* **2013**, *192*, 153–170.

[53] Maffeo, C.; Bhattacharya, S.; Yoo, J.; Wells, D.; Aksimentiev, A. *Chem. Rev.* **2012**, *112* (12), 6250-6284.

[54] Chen, M.; Chen, Y.; Zhong, W.; Yang, J. *Sci. China, Ser. E: Technol. Sci.* **2008**, *51* (7), 921–931.

[55] Kornyshev, A. A.; *J. Phys. Chem. B* **2007**, *111* (20), 5545–5557.

[56] Grahame D. C. *Chem. Rev.* **1947**, *41*, 441–501.

[57] Liu, J. L.; Eisenberg, B. *J. Phys. Chem. B* **1947**, *117* (40), 12051–12058.

[58] Kornyshev, A. A.; Vorotyntsev, M. A. *J. Phys. C: Solid State Phys.* **1979**, *12* (22), 4939–4946.

[59] Helmholtz, H. L. F. *Ann. Physik* **1853**, *89*, 211.

[60] Gouy, G. *Compt. Rend.* **1910**, *149*, 654.

[61] Chapman, D. L. *Phil. Mag.* **1913**, *25*, 475.

[62] Oldham, K. B., J. *Electroanal. Chem.* **2008**, *613*, 131.

[63] Fedorov, M. V.; Kornyshev, A. A. *J. Phys. Chem. Lett.* **2008**, *112*, 11868.

[64] Vatamanu, J.; Borodin, O.; Smith, G. D. *Phys. Chem. Chem. Phys.* **2010**, *12* (1), 170–182.

[65] Spohr, E. *Electrochim. Acta* **1999**, *44* (11), 1697–1705.

[66] Reed, S. K.; Lanning, O. J. *J. Chem. Phys.* **2007**, *126* (8), No. 084704.

[67] Marsili, S.; Signorini, G. F.; Chelli, R.; Marchi, M.; Procacci, P. *J. Comput. Chem.* **2010**, *31* (5), 1106–1116.

[68] Siepmann, J. I.; Sprik, M. *J. Chem. Phys.* **1995**, *102* (1), 511–524.

[69] Heyes, D. M. *Phys. Rev. B* **1994**, *49* (2), 755–764.

[70] Parry, D. E. *Surf. Sci.* **1975**, *49* (2), 433–440.

[72] Masia, M.; Probst, M.; Rey, R. *J. Chem. Phys.* **2004**, *121*, 7362–7378.

[73] Guseinov, I. I. *J. Math. Chem.* **2007**, *42* (3), 415-422.

[74] Borodin, O.; Smith, G. D. *J. Phys. Chem. B* **2006**, *110*, 11481–11490.

[75] Borodin, O.; Smith, G. D. *Macromol.* **2007**, *40* (4), 1252–1258.

[76] Borodin, O.; Smith, G. D. *J. Phys. Chem. B* **2009**, *113* (6), 1763–1776.

[77] Borodin, O.; Smith, G. D.; Douglas, R. *J. Phys. Chem. B* **2003**, *107* (28), 6824–6837.

[78] (a) Hoover, W. G. *Phys. Rev. A.* **1985**, *31*, 1695–1697. (b) Martyna, M. E.; Tuckerman, D. J.; Klein, M. L. *Mol. Phys.* **1996**, *87*, 1117–1157.

[79] Su, Y. Z.; Fu, Y. C.; Yan, J. W.; Chen, Z. B.; Mao, B. W. *Angew. Chem. Int. Ed.* **2009**, *48*, 5148.

[80] Lockett, V.; Horne, M.; Sedev, R.; Rodopoulos, T.; Ralston, J. *Phys. Chem. Chem. Phys.* **2010**, *12*, 12499–12512.

[81] Lin, L. G.; Wang, Y.; Yan, J. W.; Yuan, Y. Z.; Xiang, J.; Mao, B. W. *Electrochem. Commun.* **2003**, *5* (12), 995–999.

[82] Silva, F.; Gomes, C.; Figueiredo, M.; Costa, R.; Martins, A.; Pereira, C. M. *J. Electroanal. Chem.* **2008**, *622*, 153.

[83] Alam, M. T.; Masud, J.; Islam, M. M.; Okajima, T.; Ohsaka, T. *J. Phys. Chem. C* **2011**, *115* (40), 19797–19804.

[84] Lewandowski, A.; Galiski, M.; Krajewski, S. R. *J. Phys. Sci.* **2007**, *62* (3–4), 187–190.

[85] Vatamanu, J.; Borodin, O.; Bedrov, D.; Smith, G. D. *J. Phys. Chem. C* **2012**, *116*, 7940–7951.

[86] Vatamanu, J.; Borodin, O.; Smith, G. D. *J. Phys. Chem. B* **2011**, *115*, 3073–3084.

[87] Vatamanu, J.; Cao, L.; Borodin, O.; Bedrov, D.; Smith, G. D. *J. Phys. Chem. Lett.* **2011**, *2*, 2267–2272.

[88] Vatamanu, J.; Borodin, O.; Bedrov, D.; Smith, G. D. *J. Phys. Chem. C* **2012**, *116*, 7940–7951.

CHAPTER 2

A MOLECULAR DYNAMICS SIMULATION STUDY OF THE ELECTRIC DOUBLE LAYER AND CAPACITANCE OF BMIM PF_6 AND BMIM BF_4 ROOM TEMPERATURE IONIC LIQUIDS NEAR CHARGED SURFACES

Hu, Z.; Vatamanu, J.; Borodin, O.; Bedrov, B. *Phys. Chem. Chem. Phys.* **2013**, *15*, 14234–14247.

PCCP

RSC Publishing

PAPER

View Article Online
View Journal | View issue

Cite this: *Phys. Chem. Chem. Phys.*, 2013, **15**, 14234

A molecular dynamics simulation study of the electric double layer and capacitance of [BMIM][PF_6] and [BMIM][BF_4] room temperature ionic liquids near charged surfaces

Zongzhi Hu,[a] Jenel Vatamanu,*[a] Oleg Borodin[b] and Dmitry Bedrov[a]

Received 20th March 2013,
Accepted 24th June 2013

DOI: 10.1039/c3cp51218e

www.rsc.org/pccp

A molecular dynamics simulation study of electric double layer (EDL) structure and differential capacitance (DC) of two 1-butyl-3-methylimidazolium (BMIM)-based room temperature ionic liquids, *i.e.* [BMIM][BF_4] and [BMIM][PF_6], has been conducted on basal and prismatic graphite as well as (001) and (011) gold electrode surfaces. The influence of the electrode surface and electrolyte structure on electrode capacitance and EDL structure are discussed. For a given electrode surface both the [BMIM][BF_4] and [BMIM][PF_6] electrolytes generate very similar DC and EDL structures. The DC for these ionic liquids in contact with atomically flat surfaces (*i.e.* basal graphite and (001)Au) shows very small variations within the electrolyte chemical stability potential window and fluctuates around an average value of $\sim 5\ \mu F\ cm^{-2}$. On atomically more corrugated surfaces (*i.e.*, Au(011) and prismatic graphite) the DC shows more variation with electrode potential and depends on the correspondence between dimensions of the surface roughness and electrolyte ion sizes. The trends and dependencies obtained for DC are used to discriminate between mutually contradictory experimental data reported in the literature for related systems.

1. Introduction

The behavior of room temperature ionic liquids (RTILs) near charged surfaces is attracting great interest due to potential utilization of these electrolytes in energy storage devices such as Li-batteries[1–13] and supercapacitors.[14–27] In particular, the small vapor pressure,[28–33] low flammability,[34] high ionic conductivity,[35–40] relatively low melting temperature,[41–51] high thermal[52–61] and electrochemical[57,62–70] stability make RTILs excellent candidates for electrolytes in these applications. In supercapacitors, the energy storage is due to electrostatic interactions between electrode surfaces and the restructured electrolyte layer near those surfaces, which is often referred to as the electric double layer (EDL). The absence of the Faradaic reactions provides supercapacitors several unique advantages compared to electrochemical batteries. For example, supercapacitors can be charged/discharged faster,[71–80] deliver more power,[81] cannot be overcharged and can tolerate virtually millions of charge–discharge cycles.

Understanding the EDL structure and its correlation with differential capacitance (DC) is important both from theoretical and practical points of view. The DC, defined as a derivative of electrode surface charge density (σ) with respect to electrode potential ($U_{electrode}$), DC = $d\sigma/dU_{electrode}$, indicates the amount of energy that can be stored by the electrode at corresponding applied potential. The DC dependence on applied voltage provides important insight into the understanding of electrolyte interactions with the surface because many changes in EDL structure typically leave a signature in the DC shape. Therefore, the DC is usually a central focus of experimental studies of supercapacitors as well as every theoretical model that correlates EDL structure with capacitance.

Several theoretical models have focused on prediction and explanation of correlations between EDL structure and trends in DC.[82–99] These models found that on a flat surface, in general, the DC can be either a U-shaped with a minimum at low potentials (near the potential of zero charge, PZC), or a bell-shaped with a maximum at low potentials. The U-shaped DC typically has a low voltage minimum flanked by two maxima at higher electrode potentials and therefore, in a wider potential

[a] *Department of Materials Science and Engineering, University of Utah, 122 S. Central Campus Dr, Salt Lake City, UT 84112, USA. E-mail: jenel.vatamanu@utah.edu*
[b] *Electrochemistry Branch, Army Research Laboratory, 2800 Powder Mill Rd, Adelphi, MD 20783, USA*

range, becomes a camel-shaped. These trends were explained by the analytical model of Kornyshev[100] as arising primarily from steric exclusion effects. Specifically, on surfaces where at PZC the EDL structure has relatively low density and, hence, can accommodate more ions without significant free energy penalty, the rate of charge accumulation as a function of electrode potential ($d\sigma/dU_{electrode}$) is high, leading to increase in DC with increasing electrode potential. However, at higher potentials the electrode surface eventually becomes overcrowded with counterions and $d\sigma/dU_{electrode}$ (*i.e.* DC) begins to decrease with further increase of electrode potential, hence, reflecting the fact that it is difficult to bring more counterions to the surface. Therefore on surfaces that at PZC do not cause significant densification of electrolyte in the interfacial layer or a strong preferential partitioning of one type of ions, a U-shaped DC is expected. In contrast, if at PZC the EDL is already crowded by the counterions and/or has a high overall density due to van der Waals interaction with the surface, *i.e.* the EDL is sufficiently incompressible, further increase in applied potential will not lead to increase in electrode charge sufficiently fast, therefore leading to decrease in DC and, hence, a bell-shaped DC dependence can be expected.

Recent experiments[101–103] and simulations[104,105] showed that both types of DC are observed in RTIL electrolytes. These studies also showed that electrode surface topography,[106,107] electrode porosity,[108–114] electrolyte and electrode polarizabilities,[115] strength of electrode–electrolyte dispersion interactions,[116] details of electrolyte chemical structure,[117] and temperature[97] can substantially alter the shape of DC, often to an unexpected extent. While many simulation and experimental data can be qualitatively understood/interpreted within a framework of the Kornyshev model,[100] a careful examination of several recent experimental studies show some apparent inconsistencies between them as well as qualitative disagreements with predictions from basic theoretical models. For example Fig. 1 illustrates this by comparing several experimentally reported DCs on Au and glassy carbon electrodes. For example, Su *et al.*[118] studied [BMIM][BF_4] RTIL on an Au(001) electrode and reported a bell-shaped DC with a surprisingly large maximum near PZC ($\sim$25 μF cm^{-2}). Alam *et al.*[119] also reported large changes in DC for similar RTILs. In contrast, for a very similar electrolyte [BMIM][PF_6] Lockett *et al.*[120] found essentially a constant DC ($\sim$6–7 μF cm^{-2}) as a function of electrode potential. Similarly large differences in DC were observed for [BMIM][PF_6] on glassy carbon as measured by Lockett *et al.*[120] who reported DC changing between 4 and 8 μF cm^{-2} and Silva *et al.*[121] who obtained DC in the 18–27 μF cm^{-2} range. Because the nature of the electrode surfaces (*i.e.* atomically flat) and electrolytes used in the above-mentioned experiments are similar, consideration of these systems from the point of view of basic EDL models suggests that very similar values and dependence of DC should be expected. On the other hand, as we mentioned above and showed in our previous simulations, the DC and its dependence on the potential can significantly depend on the surface structure and small variations in the ion chemical structure (see *e.g.* comparison of [C_{2-8}mim][TFSI] series or [pyr_{13}][FSI] *vs.* [pyr_{13}][TFSI] in our previous studies[104]). Recent careful experimental measurements and analysis of broadband capacitance spectra[101] showed that extracting DC from single-frequency impendence measurements, which have been employed in most of the experimental studies mentioned above, can lead to artifacts and incorrect DC values. In single-frequency experiments it could be difficult to differentiate between two capacitive processes: the fast process, which corresponds to a true EDL formation process, and a slow process which could be associated with metal electrode surface restructuring.

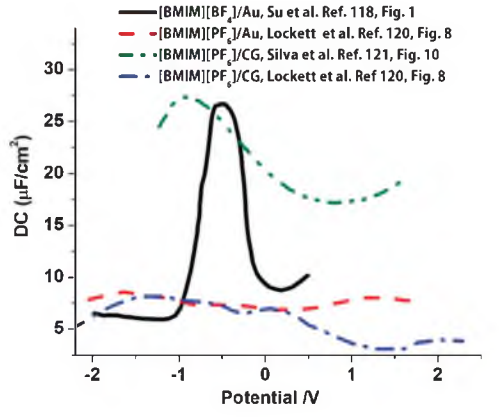

Fig. 1 Differential capacitance as a function of electrode potential from several experimental studies reported in the literature. The electrode potential is relative to a reference electrode as indicated in ref. 118, 120 and 121.

Therefore, to better understand various factors influencing the DC and EDL structure as well as to test whether the large disparities in experimental DC shown in Fig. 1 can be a consequence of small variations in anion chemical structure (PF_6 *vs.* BF_4) or surface topography, we have undertaken a molecular dynamics (MD) simulation study of these systems. Specifically, we studied both the [BMIM][PF_6] and [BMIM][BF_4] electrolytes on graphite and Au surfaces as a function of applied potential.

2. Simulation details

2.1. System set up and simulation methodology

The simulation cell was comprised of the electrolyte confined between two conductive electrodes as illustrated in Fig. 2. The electrode surfaces were graphite (basal or prismatic) or Au with (001) or (011) crystallographic orientations exposed to the electrolyte. As illustrated in Fig. 2, the graphite basal surface and the Au(001) surface are atomically flat, while prismatic graphite and Au(011) have some corrugation on a length scale of 1–2 Å. The distance between electrodes was around between 120 to 135 Å (depending on the system), which ensured that the EDLs formed on two electrodes are separated by a sufficient

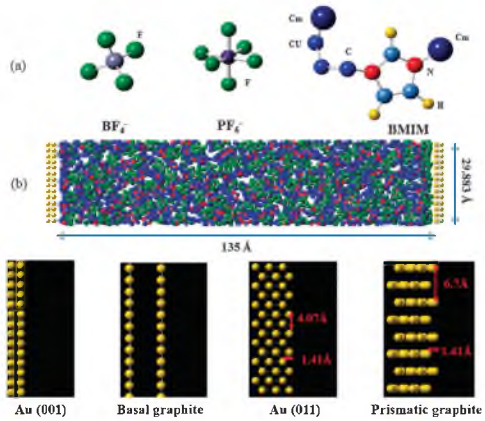

Fig. 2 Schematic illustration of the chemical structure of ions (a) and simulation cell set up and structure of electrode surfaces (b).

amount of bulk electrolyte (60–80 Å). The electrodes were modeled as conductors subjected to imposed desired electrostatic potential. The electrolyte phase was represented by 312 ionic pairs. The simulations were conducted at 423 K. The temperature was controlled by the Nose–Hoover thermostat with a coupling constant of 0.1 ps. The equations of motion were integrated using the reversible multiple time step RESPA algorithm.[122] A 0.5 fs step was used to compute forces arising from bond, bend and out-of-plane vibrations, a 2.5 fs step for the dihedral and non-bonded forces within a cut-off radius of 7.5 Å, and a 5 fs time step to evaluate van der Waals interactions within a cut-off radius of 10 Å and the reciprocal part of the Ewald summation. The latter was computed using smooth particle mesh Ewald methodology adapted for 2D symmetry.[123–126]

The potential difference between electrodes was controlled by imposing an electrostatic potential difference ΔU between two electrodes. The electrode charges varied during simulation to satisfy this constraint. The details of the methodology to iteratively compute the electrode charges are described in ref. 127 and 128. The electrode surface charges were Gaussian distributed with a width of 0.5 Å[128,129] while partial atomic charges of electrolyte molecules were point distributed. The electrode charges were updated every 50 fs.

The systems were prepared as follows: the distance between electrodes was adjusted such that the density in the middle of the electrolyte phase was the same as the density of a bulk electrolyte (with no electrodes) under corresponding thermodynamic conditions (*i.e.*, atmospheric pressure and 423 K). Then the potentials between electrodes were dialed in and the systems were equilibrated for about 4 ns to allow the formation of EDL. Each electrolyte was simulated at 24 potential differences ranging from 0 to 6 V. After equilibration, production runs over 50 ns were conducted for each system.

2.2. Force field

In order to reduce the computational cost, a computationally efficient united atom/explicit atom force field previously developed for [*N*-methyl-*N*-propylpyrrolidinium] [bis(trifluoromethanesulfonyl)imide], or [pyr_{13}][TFSI], and [pyr_{13}][bis(fluorosulfonyl)-imide], or [pyr_{13}][FSI], and [$C_n$mim][TFSI][104] was extended to [BMIM][PF_6] and [BMIM][BF_4]. In this model the alkyl $-CH_2-$ and CH_3- groups are represented as united atoms, while all atoms in the imidazolium cyclic structure and anions are represented explicitly. The BMIM force field parameters were taken from our previous work on [$C_n$mim][TFSI] RTILs.[104] The parameters for PF_6^- and BF_4^- anions were taken from the APPLE&P polarizable force field.[130] The developed force field was validated by comparing the prediction from simulations of thermodynamic, structural and transport properties of [EMIM][BF_4] and [BMIM][PF_6] RTILs with available experimental data as well as with predictions from simulations using a fully atomistic APPLE&P polarizable force field. Table 1 indicates that the combined force field predicts density within 0.7% of experimental values, while diffusion coefficients and ionic conductivity are within 30% of experimental values. This description of transport properties is in a better agreement with experiments than the fully atomistic simulations using the APPLE&P force field with polarization turned off. Force field parameters for graphite description were adopted from ref. 131 while the cross-term parameters

Table 1 Density (ρ), diffusion coefficients (D) and conductivity (λ) of bulk RTILs predicted using the combined UA/LA force field

T (K)	Force field	ρ (kg m^{-3})	D_+ (10^{-10} m^2 s^{-1})	D_- (10^{-10} m^2 s^{-1})	λ (mS cm^{-1})	Ref.
[BMIM][PF_6]						
393	UA/EA	1294	1.38	1.43	20.4	
393	Experiment	1288	1.83	1.55	29.6	154
393	APPLE&P(f1e12)	1267	2.01	1.54	27.9	
[EMIM][BF_4]						
393	UA/EA	1197	3.89	3.21	94	
393	Experiment	1206	4.00	3.57	87.7	155–157
393	APPLE&P(f1e17)	1187	4.87	4.07	118	
333	UA/EA	1246	1.32	1.13	32	
333	Experiment	1253	1.35	1.16	35.6	155–157
333	APPLE&P(f1e17)	1223	1.76	1.63	43.9	
298	UA/EA	1275	0.48	0.36	14.7	
298	Experiment	1280	0.497	0.416	15.7	155–157
298	APPLE&P(f1e17)	1259	0.50	0.42	15.9	

describing interactions with the electrolyte were obtained using combining rules. The description of non-bonded interactions of RTILs with Au surfaces was more challenging as, to the best of our knowledge, there have been rather limited efforts dedicated to parameterization of force field parameters for Au interaction with organic liquids.[132] Therefore, for simplicity and consistency of comparison between graphite and Au surfaces, in this work for Au atoms we have used the same Lennard-Jones parameters as for graphite carbons. Since the positions of Au atoms on electrode surfaces are fixed in our simulations, this choice of Au representation only influences electrode–electrolyte interactions and does not perturb Au surface structure. The selected representation of Au is in reasonable agreement with interactions reported for Au with proteins developed based on *ab initio* calculations.[132]

2.3. Details of analysis

Here we briefly review definitions of properties used in our analysis. The EDL potential (or the potential drop within the electrode/electrolyte interfacial region), U_{EDL}, is defined as the difference between electrostatic potential on the electrode surface ($\phi_{electrode}$) and the potential in the bulk electrolyte (ϕ_{bulk}),

$$U_{EDL} = \phi_{electrode} - \phi_{bulk} \quad (1)$$

The electrode potential ($U_{electrode}$) is defined as the EDL potential (U_{EDL}) relative to the potential of zero charge (PZC).

$$U_{electrode} = U_{EDL} - PZC \quad (2)$$

The PZC was computed as the potential drop within the EDL for uncharged electrode surfaces which can be obtained by setting the potential difference between two electrodes to zero.

From simulation trajectories we compute the electrode and electrolyte charge density profiles in the direction perpendicular to electrode surfaces, which is aligned with our choice of the z-axis. From these charge profiles we then calculate the Poisson potential by integrating along the z-axis the 1D Poisson equations:

$$\nabla_z[\varepsilon_0(\nabla_z\phi(z))] = -\rho(z) \quad (3)$$

The differential capacitance (DC) is then computed using the numerical derivative of the electrode charge density per unit surface (σ) with respect to the electrode potential.

$$DC(U_{electrode}) = d\sigma/dU_{electrode} \quad (4)$$

Note that in this definition, the capacitance is normalized per unit surface area of the electrode surface. In order to numerically differentiate eqn (2) we followed a procedure originally described in ref. 133. Specifically, we have chosen several (typically five or seven) consecutive points of $\sigma(U_{electrode})$ dependence within the 0.3–0.5 V potential window and approximated them with a parabola. The DC in the middle point was then obtained using the analytical derivative of the fitted parabola.

Finally, we remind that in our simulations all electrodes are treated as conductors. While for Au this is a natural assumption, carbon based electrodes can have noticeable semiconducting character.[134,135] The latter can significantly vary depending on electrode preparation and fabrication conditions. As was shown by Gerischer *et al.*[134,135] in semiconductive electrodes, a space charge distribution inside the electrode is generated and the total capacitance (C) is given by the contribution of the capacitance inside the semiconductor (C_{sc}) and the capacitance generated by electrolyte ordering (C_{el}) near the electrode surface: $1/C = 1/C_{sc} + 1/C_{el}$. The contribution of C_{sc} to total DC for semiconductive electrodes is not negligible and a U-shaped DC measured on graphite was previously interpreted by Gerischer as a result of changes in electronic density of states and the Fermi distribution in pyrolitic graphite itself rather than electrolyte ordering near the electrodes. Due to the assumption of the electrode being conductive our simulations using graphite electrodes only access the capacitances given by the electrolyte ordering/restructuring near the surface (*i.e.*, C_{el}). Hence, the capacitances determined from our analysis of simulations should correctly capture the trend of DC near Au surfaces or ideal graphite structures as in our simulations, but might miss some additional capacitive modes that might be present in real life carbon-based electrodes that contain semiconducting structural elements.

3. Results and discussion

3.1. Atomically flat surfaces

First we focus on the comparison of EDL structure and capacitance obtained for the two RTILs on atomically flat surfaces, namely the Au(001) surface and basal plane graphite.

Differential capacitance. The DCs as a function of electrode potential obtained for [BMIM][BF_4] and [BMIM][PF_6] on Au(001) and basal graphite are compared in Fig. 3a and b. On graphite both RTILs show an overall bell-shaped DC dependence as a function of electrode potential with a maximum value of about 5.5 μF cm^{-2} around PZC and the lowest value of about 3.7 μF cm^{-2} in the potential range investigated. Therefore the observed changes in DC as a function of electrode potential are relatively modest. Also, the shape and magnitude of DC for both RTILs are very similar indicating that the difference in the anion structure is not important for defining DC on the basal plane graphite surface. A bell-shaped DC for the [BMIM][PF_6]–graphite system was also observed recently in simulations of Paek *et al.*[136] using a slightly different simulation approach, *i.e.* the fixed and homogeneous distribution of electrode surface charges as well as a different force-field. The DC predicted by Paek *et al.*[136] was between 3 and 4.7 μF cm^{-2} which is systematically lower compared to our values by about 0.7 μF cm^{-2}. These small differences in DC can be due to variations in the utilized force fields or the inclusion of electrode polarizability. However, both simulations consistently predict the DC ranging between 4 and 5 μF cm^{-2} for this RTIL on a flat surface in the experimentally relevant potential window.

On the Au(001) surface (Fig. 3b) more variations between two RTILs can be observed. On this surface, the [BMIM][BF_4] shows a well-defined camel-shaped DC dependence with a clear

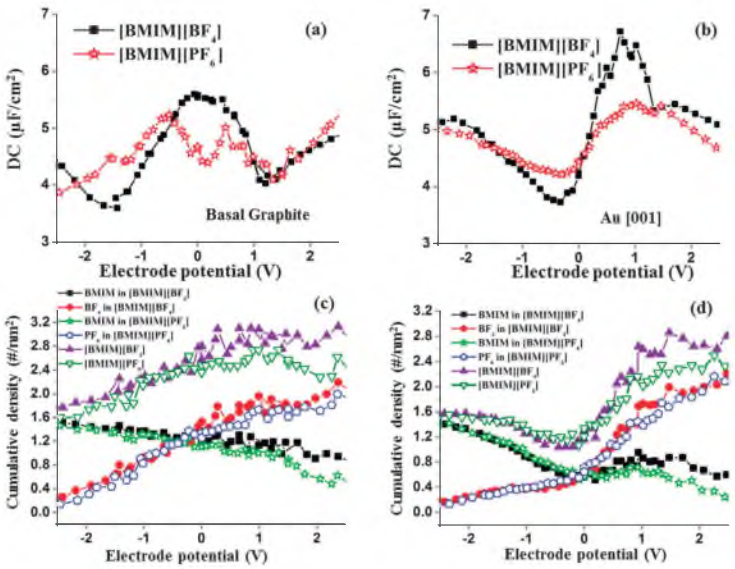

Fig. 3 Differential capacitance for (a) [BMIM][BF_4] and [BMIM][PF_6] on the graphite surface, (b) [BMIM][BF_4] and [BMIM][PF_6] on the Au(001) surface and cumulative density of ions in the 5 Å interfacial layer for (c) graphite and (d) Au(001) surfaces as a function of electrode potential.

minimum near PZC and slightly shifted to negative values ($\sim$ 0.2 V) of electrode potentials. As the electrode potential increases (either negative or positive) the DC increases but very asymmetrically. On the positive surface, the DC increases sharply and reaches a maximum of 6.8 μF cm^{-2} at about +0.9 V and then sharply drops to about 5 μF cm^{-2} with further increase of the potential. In the negative range of potentials, the DC increases more gradually and reaches a maximum of 5.2 μF cm^{-2} at about −2.3 V. Note that a slight increase in capacitances at somewhat larger potentials was also observed experimentally by Su *et al.*,[118] Costa *et al.*,[137] and Alam *et al.*[119] for imidazolium-based RTILs. The [BMIM][PF_6] on the Au(001) surface shows a qualitatively similar behavior to [BMIM][BF_4] RTIL; however, the amplitude of DC variations between maxima and minima is much smaller, about 1.1 μF cm^{-2} which is consistent with the extent of variations observed for this RTIL on the graphite surface.

Fig. 3a and b also show that with the exception of [BMIM][BF_4] on the Au(001) surface, all other electrode–electrolyte combinations have an average DC of 4.5–5.0 μF cm^{-2} and rather small variations ($\sim$1.0 to 1.5 μF cm^{-2}, or 20–25%) in the potential range investigated. This behavior is in agreement with our previous simulations showing that atomically flat surfaces generate DCs that have only weak dependence on the applied potential in the typical operational range. For example, similarly small changes in DC *vs.* potential were observed in our previous studies of [pyr_{13}][TFSI],[138] [pyr_{13}][FSI],[139] [EMIM][Li/FSI],[140] and [$C_n$mim][TFSI][141] RTILs in contact with flat (graphite) surfaces. Almost constant DC *vs.* potential was also obtained for these types of electrolytes by Merlet *et al.*[142,143] utilizing a coarse-grained model and similar treatment of electrode polarization.

The comparison of simulation predicted DC for [BMIM][PF_6] and [BMIM][BF_4] (Fig. 3a and b) with available experimental data on Au and glassy carbon (GC) (Fig. 1) indicates a good agreement with experimental data of Lockett *et al.* ([BMIM][BF_4] on GC)[120] that showed DC on the order of 4–9 μF cm^{-2} with relatively small dependence on electrode potential. However, our results are not even in qualitative agreement with those reported by Su *et al.*[118] for [BMIM][BF_4] on Au surface and by Silva *et al.*[121] for [BMIM][PF_6] on GC. Both of the studies reported very large values of DC ($\sim$25 μF cm^{-2}), with the former reporting a bell-shaped DC with unusually large maxima near PZC. Interestingly, the same work by Silva *et al.*[121] reports almost a constant DC with a value of around 6 μF cm^{-2} for [BMIM][PF_6] on the Pt electrode, which is in good agreement with our simulations. Taking into account that the majority of simulations of RTILs on flat surfaces typically predict almost a constant DC with an average value between 4 and 5.5 μF cm^{-2} within a potential window of ±2 V and significant discrepancy between some of the experimental studies mentioned above and the inherent difficulties in determining DC from experiment discussed above,[101,144] we believe that atomistic MD simulations could and should be used for tuning/calibration of DC measurements in experiments. We remind that the only instance in which our simulations predicted large variations and magnitudes of DC was when RTILs were placed on atomically rough surfaces where the dimensions of surface

features/patterns were comparable to ion sizes.[107] This suggests that it is possible that the large DC values reported by Su *et al.*[118] and Silva *et al.*[121] are either influenced by unaccounted contributions in electrode surface topography (*i.e.* surface roughening or restructuring) or may be affected by the inherent difficulties on measuring experimental DCs as discussed in ref. 101.

EDL structure: ion center-of-mass distributions. Next we investigate correlations between the EDL structure and DC dependencies as a function of electrode potential for investigated systems. Fig. 4 shows the center-of-mass density profiles of ions near the gold surface as a function of distance from the electrode and the applied potential. Qualitatively both RTILs have similar density profiles, see the comparison of Fig. 4a and c for BMIM and Fig. 4b and d for anions. As expected, as the electrode potential increases a counter-ion accumulation near the surface is observed. Comparison of Fig. 4b and d shows that at positive potentials the center-of-mass of BF_4^- approaches the gold surface by about 0.5 Å closer than PF_6^-. However, the comparison of F atom density profiles indicates that the initial rise in the density profile and the location of the first peak are at the same positions for both anions.

Fig. 5 further illustrates the changes in ion density profiles as a function of electrode potential. Here, the center-of-mass density profiles are compared for [BMIM][BF_4] on Au(001) at PZC and ±1 V electrode potentials. Examination of Fig. 5 reveals that most of the restructuring of the electrolyte occurs within ~15 Å from the electrode surface. At PZC both ions show a strong presence at the surface indicated by comparable heights of the first peaks defining the immediate interfacial layer (about 5.0 Å from the electrode surface). As electrode potential becomes negative the BMIM density in this layer increases (the height of the first peak increases) while the density of BF_4 decreases (the first peak is pushed out to further distances and merges with the second peak). This ion exchange process does not result in any noticeable change in the total ion density (Fig. 5c) in the interfacial layer. As the electrode potential becomes positive a qualitatively different picture is observed. At +1.0 V the density of BF_4 anions almost doubles in the interfacial layer. Anions pulled to the positively charged surface also bring along additional cations to minimize the anion–anion electrostatic repulsion. As a result the BMIM density at the interface also increases (see Fig. 5a) despite electrostatic repulsion by the positively charged surface. Hence, the overall number of ions in the first layer also increases as is evident from Fig. 5c.

The cumulative ion density in the interfacial layer (within 5.0 Å from the electrode surface) discussed above is plotted as a

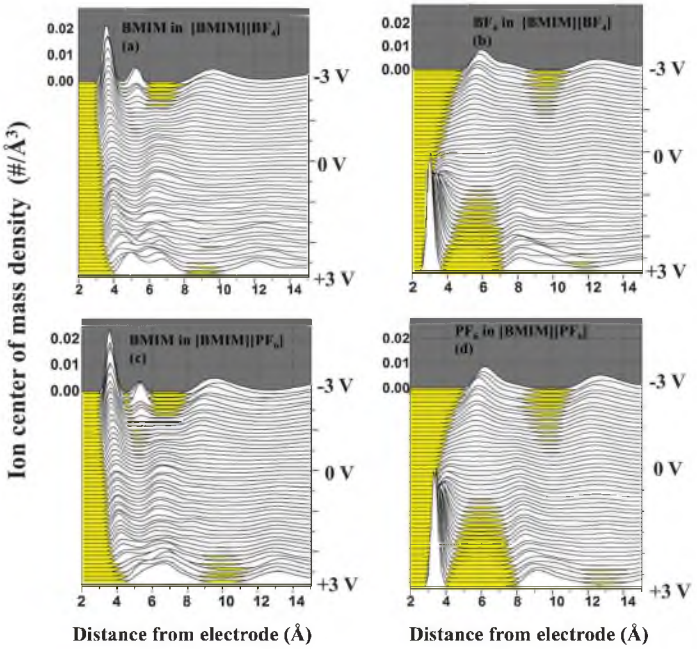

Fig. 4 Ion center-of-mass density profiles (left vertical axis) as a function of separation from electrode surface for a series of electrode potentials (right vertical axis) (a) density of BMIM for [BMIM][BF_4]/Au(001) system, (b) density of BF_4 for [BMIM][BF_4]/(Au-001) system, (c) density of BMIM for [BMIM][BF_6]/ (Au-001) system, and (d) density of PF_6 for [BMIM][BF_6]/ (Au-001) system.

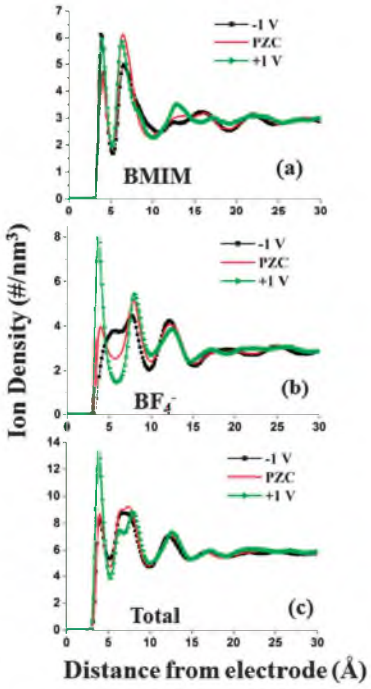

Fig. 5 Ion density profiles as a function of distance from electrode for [BMIM][BF_4] on the Au(001) surface: (a) BMIM density, (b) BF_4 density, and (c) total density.

function of electrode potential in Fig. 3c and d for both RTILs on graphite and Au, respectively. First, these figures illustrate that for a given electrode surface both RTILs show very similar dependencies of ion densities at the interface. Second, consistent with the Fig. 5 discussion, on the Au(001) surface as the electrode is charged negatively the anion density decreases while the cation density increases. Between PZC and −1 V these rates are similar, therefore resulting in almost a constant total number of ions. However, at more negative potentials the rate of BMIM addition to the surface outruns the anion reduction and hence the total number of ions slightly increases. On the positive range of potentials, from PZC to +1 V, we see a significant increase in anion density in the interfacial layer accompanied by a slight increase in BMIM density therefore resulting in a very sharp increase in the total number of ions at the interface. Above +1.0 V potentials, the BMIM density starts slowly to decrease with increasing potential while the rate of anion addition reduces, therefore resulting in a saturation of the total ion density. On the graphite surface, the dependence of cumulative densities on electrode potential is different. At PZC the total density of ions is at its saturation limit. As the potential becomes negative, the anion density drops faster than the BMIM density increases and hence, the total ion density monotonically decreases. On the positive electrode, the ion exchange in the interfacial layer goes with approximately the same rate and therefore the total ion density remains almost constant.

EDL structure: atomic distributions. Next we examine atomic level structure near the electrode surface as shown in Fig. 6. At the positive potential the density profile for F atoms (from PF_6 or BF_4) has two maxima at 2.9 and 4.6 Å from the Au(001) surface. For PF_6 the peaks are similar in magnitude suggesting that anions are oriented to allow three F atoms to be in direct contact with the surface. For BF_4 we also observe two maxima at the same positions, but with a 3 : 1 relative ratio of the area under the peaks indicating that BF_4 also points three F atoms toward the positive surface. As shown in Fig. 6, there is somewhat elevated concentration of F atoms near the negative surface even at −2 V. This suggests that for these RTILs, larger potentials are needed to segregate ions in the interfacial layer, in contrast to RTILs containing FSI or TFSI anions where −2 V was sufficient to repel most of the co-ions away from the negative surface.[127,128] Such behavior is also in agreement with the interfacial composition found for RTILs of similar structural asymmetry between ions reported by Feng *et al.*[145] for the [BMIM][NO_3]–graphite and by Wang *et al.*[146] for the [BMIM][PF_6]–graphite systems.

The density profiles of the BMIM ring carbon atoms are shown in Fig. 6b and e and are very similar for both RTILs on a given electrode surface. However, there is a noticeable difference between these profiles on Au and graphite surfaces. At the negatively charged graphite surface, the density profile for ring C atoms has a single peak at about 3.2 Å from the surface, indicating essentially a parallel alignment of the ring relative to the electrode surface. In contrast, on the Au(001) surface and below −2 V two peaks at 3.2 and 4.5 Å from the surface are observed, indicating that a large percentage of BMIM cations is oriented with their ring perpendicular to the surface.

Density profiles of carbon atoms from alkyl tails are shown in Fig. 6c and f. In agreement with our previous results for [$C_n$mim][TFSI][141] and [$pyr_{1,3}$][TFSI],[138] we observe an increased density of tails near the surface at positive potentials, even at potentials as large as +2 V, indicating that while BMIM rings (carrying the positive charge) are pushed away from the direct contact with the surface the cation tails remain at the surface.

EDL structure and DC correlations. It is interesting to examine how the changes in structural distributions in the interfacial layer as a function of applied potential can be correlated with the observed trends in DC. The main questions that need to be addressed are: what level of details (molecular or atomistic) in structural changes and how far away from the interface (one layer, two layers, or several nanometers) one need to take into account to explain the observed trends in DC? For example, examination of Fig. 3 indicates that the changes in ion density and composition observed for the defined interfacial layer (within 5 Å) qualitatively correlate with the observed DC dependence on electrode potential and the differences between graphite and Au(001) surfaces. Indeed, taking into account that the atom surface density in the graphite layer is ~38 C atoms nm^{-2}, while the surface density of the top Au(001) layer

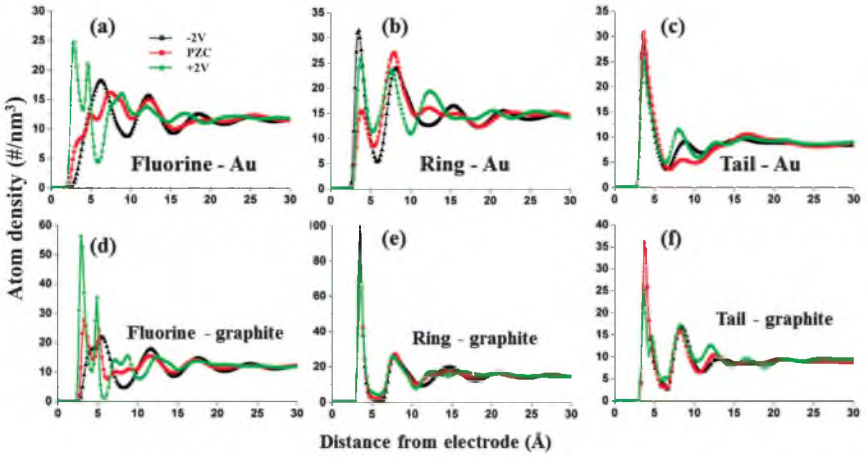

Fig. 6 Atom density profiles for various groups on graphite and Au surfaces: (a) fluorine (b) BMIM ring carbon atoms, (c) carbon atoms from the BMIM alkyl tail, and on the graphite surface: (d) fluorine, (e) BMIM ring carbon atoms, and (f) carbon atoms from BMIM alkyl tail.

is $\sim$12 atoms nm^{-2} one can expect a stronger van der Waals dispersion interaction between the ions and the graphite surface. Fig. 3c and d clearly confirm this supposition indicating that the total density of ions for both RTILs at PZC is about a factor of 2.5 larger on the graphite surface than on Au(001). Hence, one can consider the interfacial layer on graphite to be tightly packed and according to theoretical predictions by the Kornyshev model a bell-shaped DC should be expected in this case. The latter is indeed observed for both RTILs in the vicinity of PZC. For the loosely packed interfacial layer near the Au(001) surface, charging the surface results in overall densification of ions in the interfacial layer which leads to the U-shaped DC dependence near PZC. At higher potentials, as the total density of ions saturates on both electrodes the DC reaches its maxima resulting therefore in an overall camel-shaped DC for both RTILs.

While the generic trends observed in cumulative density of ions within the 5 Å interfacial layer are qualitatively consistent with observed DC trends, it is also important to understand the contribution of other layers to DC. To examine these we have calculated contributions to DC from the changes in charge densities associated with the center-of-mass of the ions as well as from individual atoms in the layers of various widths adjacent to electrode surfaces. Fig. 7a compares the total DC obtained for [BMIM][BF_4] on Au(001) with the derivative of the total charge density calculated based on the center-of-mass of ions in the interfacial layer of thickness d near the electrode surface. For the latter the total charge density was defined as $\sigma_{com} = \int_0^d (\rho_{BMIM}(z)q_{BMIM} - \rho_{anion}(z)q_{anion})dz$, where q_{BMIM} = +1, q_{anion} = −1, and $\rho_{BMIM}(z)$ and $\rho_{anion}(z)$ are the ion center-of-mass density profiles. Fig. 7b shows similar derivatives but obtained based on changes in the interfacial layer charge arising

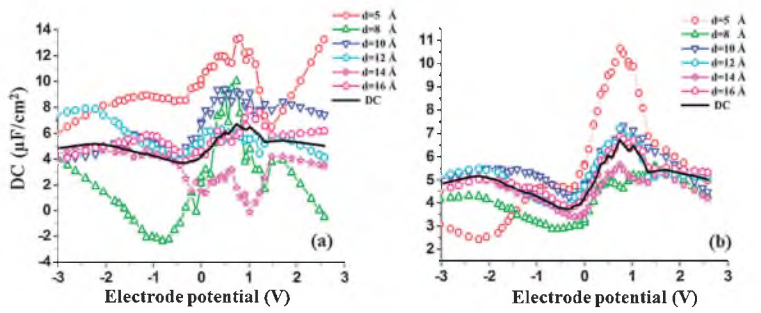

Fig. 7 Differential capacitance and the derivatives of the electrolyte charge density located within interfacial layers of various widths, d, near the electrode surface. Note, that for convenience of comparison the derivatives of electrolyte charge densities were multiplied by −1 and rescaled in units of μF cm^{-2}. The charge densities were computed based on (a) locations of ions center-of-mass and (b) atoms location and their corresponding partial charges.

from various atom types located in the layer, *i.e.* derivatives of $\sigma_{\text{atom}} = \int_0^d \left(\sum_i \rho_{i,\text{BMIM}}(z) q_{i,\text{BMIM}} + \sum_j \rho_{j,\text{anion}}(z) q_{j,\text{anion}} \right) \text{d}z$ where the summation is done over all atoms i and j belonging to BMIM or anions located within distance d from the electrode surface and $q_{i,\text{ion}}$ are the corresponding partial atomic charges for each atom.

Examination of Fig. 7 shows that independently of whether we use the center-of-mass or the atomic based calculations of the interfacial layer charge, the derivative of the charge accumulated in the interfacial layer of thickness 5.0 Å is in a poor quantitative agreement with DC. This indicates that while some qualitative trends in DC might be captured by structural changes in the immediate (first) layer of ions at the surface, the outer layers clearly have an important influence (at least for electrolytes investigated here) both in defining the dependence and the magnitude of DC as a function of electrode potential. Fig. 7 indicates that one has to take into consideration the restructuring of ions within the interfacial layer, $d \approx 12$ to 14 Å, in order to get a quantitative agreement of the electrolyte charge derivative with DC. However, consideration of an interfacial layer of 7–7.5 Å seems to be enough to capture qualitatively most features in DC. Interestingly, in our previous studies of systems with similar cations but less symmetric (more elongated) anions such as FSI and TFSI, we found that smaller (*i.e.* ≈5–6 Å) interfacial electrolyte widths were sufficient to obtain good agreement between the electrolyte charge derivative and DC.[106]

3.2. Atomically corrugated surfaces

Our previous simulations of RTILs containing FSI and TFSI anions have shown that details of the electrode surface structure, specifically the atomic scale roughness of the surface, can significantly change DC magnitude and even qualitatively change its shape as a function of electrode potential.[106] Here, we are probing how the atomic roughness of the electrode surface can influence the DC of RTILs containing PF_6 and BF_4 anions which are smaller and more spherical compared to FSI and TFSI anions. For this purpose we have simulated [BMIM][BF_4] on atomically more corrugated Au(110) and prismatic face graphite surfaces (see Fig 1). Note, that in contact with RTIL the Au(110) surface can, in principle, rearrange its structure and have a different configuration compared to a perfect crystal cut, but for our purpose of having well defined and controlled atomic scale roughness we have constrained the surfaces to the corresponding crystallographic symmetry. Both, the prismatic graphite and the Au(110), surfaces have atomic scale parallel grooves exposed to the electrolyte as shown in Fig. 1. The depth of the grooves is defined as the distance between the outermost and innermost atoms exposed to the electrolyte and it is very similar for both surfaces, *i.e.* 1.4 Å for Au(011) and 1.41 Å for prismatic graphite. The distance between neighboring grooves (*i.e.*, the widths of the surface patterns) is 4.0 Å for Au(110) and 7.5 Å for prismatic graphite. Therefore, grooves on the graphite surface are comparable to ion sizes while those on the Au(011) are not wide enough even to fit BF_4 or PF_6 anions.

In Fig. 8 we compare the DC obtained for [BMIM][BF_4] RTIL on atomically flat and corrugated surfaces. Fig. 8a shows that the DC on Au(001) and (011) surfaces are very similar, indicating that there is no influence of the gold surface structure. This observation is consistent with dependence of cumulative densities of ions in the interfacial layer as a function of electrode potential shown in Fig. 8b. Again, very little difference can be observed in EDL structure for these two surfaces. However, a quite different behavior is observed for the basal *vs.* prismatic graphite surfaces shown in Fig. 8c and d. Fig. 8c shows that the DC on prismatic graphite has a broad minimum between −0.35 V and −1.2 V and an enhanced maximum at +0.9 V. The variations in DC between minima and maxima are clearly more pronounced for the atomically rough surface. In agreement with our previous studies of other RTILs, for [BMIM][BF_4] on prismatic graphite we find an overall larger DC compared to that on the basal graphite surface. For example, on prismatic graphite the maximum in DC of 8.8 μF cm^{-2} (at +0.9 V) is reached compared to the 5.6 μF cm^{-2} near 0 V on the basal graphite. Near PZC on the prismatic graphite the maximum in DC is shifted to larger potentials which leads to a U-shaped (or camel-shaped) DC. The changes in the interfacial composition with potential are shown in Fig. 8d and are qualitatively consistent with the observed trends in DC. Indeed, for the basal graphite surface we observe almost linear increase or decrease in ion densities in the interfacial layers as a function of potential which is consistent with relatively small variation in DC. In contrast, on the basal graphite we observe small changes in BF_4 interfacial density at the negative electrode and a sharp increase in interfacial density of BF_4 in the potential range 0 to +1 V where DC increases sharply and reaches a maximum (at +0.9 V).

These results further support previously discussed trends that there is a strong impact of surface roughness on DC. Theoretical models developed by Kornyshev and co-workers[147,148] showed that surface roughness can reduce the variations of DC as a function of electrode potential. However, these studies mostly focused on the case of 'weak roughness' where dimensions of roughness were assumed to be larger than ion dimensions. Our atomistically detailed simulations presented here and in previous studies showed that the atomic scale roughness of the electrode surface can change the DC even qualitatively when the dimensions of the surface roughness are comparable to the ion sizes.

3.3. Influence of chemisorption

The cases considered above correspond to purely electrostatic capacitors where the formation of EDL and the capacitance are determined primarily by the balance of electrostatic forces at the electrode–electrolyte interfaces. In such systems, the van der Waals interactions between surface and RTILs are rather weak compared to electrostatic interactions. However, in some systems a strong adsorption of electrolyte species can occur due to partial charge transfer between the surface and electrolyte,

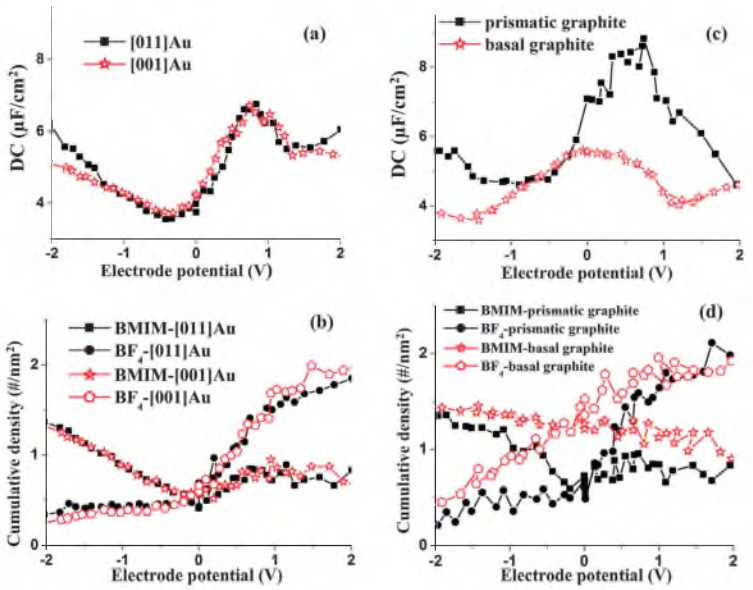

Fig. 8 (a) The DC for [BMIM][BF_4] on Au(001) and Au(011). (b) Cumulative densities of ions in the first interfacial layer (<5 Å from the electrode surface) as a function of electrode potential for [BMIM][BF_4] on Au(001) and Au(011). (c) The DC for [BMIM][BF_4] on the basal and prismatic graphite surfaces. (d) Cumulative densities of ions in the first interfacial layer (<5 Å from electrode surface) as a function of electrode potential for [BMIM][BF_4] on basal and prismatic graphite.

i.e. chemisorption. For example, Gao *et al.*[149] predicted adsorption energies of Cl on Au(111) ranging between 0.5 and −0.88 eV. Therefore, in such systems the interaction of electrolyte molecules with the surface can be comparable or even stronger than electrostatic interactions between charged electrode and the ions in electrolyte. To the best of our knowledge, the role of strong adsorption of ions on EDL structure and DC in RTILs has been largely unexplored. However, the recent work of Si *et al.*[150] indicated that explicit consideration of specific adsorption in modeling of the electrode–electrolyte interface can significantly change the EDL structure and generate DC with multiple minima and maxima.

In this section we examine the role of a possible chemisorption of the anion to the surface in defining DC and EDL structure. For this purpose we have modeled [BMIM][BF_4] RTIL with artificially introduced strong attractive interaction between BF_4 anions and the gold surface. The additional attraction between anion F atoms and the surface was made short-ranged such that beyond 3.8 Å separation from the surface it would be negligible. Therefore, as shown in Fig. 9 where the unbiased F-surface van der Waals interaction (weak adsorption) is compared with the modified interaction (strong adsorption), the new interaction results in a very deep energy minimum (60.2 kJ mol^{-1}) at about 2.8 Å separation, but becomes identical to the unbiased interaction for separations larger than 4.0 Å. Note that the interaction for the strong adsorption case can only be considered as approximate

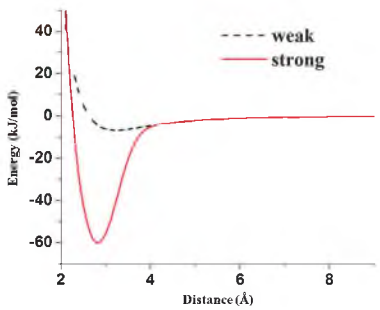

Fig. 9 The potential (van der Waals) energy between the uncharged Au(001) surface and a BF_4 ion for weak adsorption (black line) and strong adsorption (red line).

representation of chemisorption and was selected for the purpose of obtaining qualitative understanding.

The DC for the strong and weak adsorbing electrolyte on Au(001) is shown in Fig. 10a. The chemisorption changes the dependence of DC and EDL structure *vs.* potential to some extent. For RTIL with strongly adsorbing anions we observe a bell-shaped DC on the negative electrode and almost constant DC on the positive electrode. In other words, compared to a weakly adsorbing case the maximum in DC has shifted from +0.9 V to −1.85 V and increased from 7 to 8.7 μF cm^{-2}. The PZC

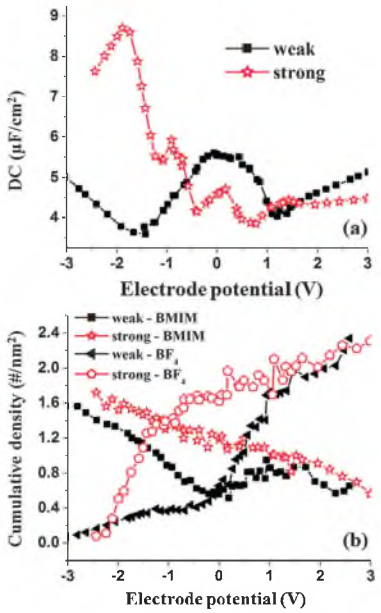

Fig. 10 (a) The DC for weak and strong adsorption cases on the Au(001) surface. (b) Cumulative densities of ions in the first interfacial layer (<5 Å from electrode surface) as a function of electrode potential for [BMIM][BF_4] on weak and strong adsorption cases.

has also shifted by as much as −0.6 V toward negative values. The integral capacitance (IC) at 2 V increases from 4.5 μF cm^{-2} for a weak adsorbing to 6 μF cm^{-2} (*i.e.* 33% larger) for strongly adsorbing anions. On the other hand, at the positive electrode the DC for strongly adsorbing systems is systematically lower and hence the corresponding IC at +2.0 V is also lower (4.2 μF cm^{-2} *vs.* 5.7 μF cm^{-2}). The latter observation can be explained by the fact that due to strong attraction with the surface the density of anions changes very little between 0 V and +2.0 V and is almost at its saturation limit at 0 V. Therefore, if both electrodes have strong adsorption of anions the net increase in the total capacitance of the capacitor is small due to cancellation between the capacitance enhancement on the negative electrode and the capacitance reduction on the positive electrodes. Hence, in such systems electrodes with different chemisorption properties are necessary. Interestingly, Fig. 10b shows that the strong interaction of anions with the surface also affects the density of BMIM at the interface in the entire range of potentials. One would expect that the increased density of anions near the surface would lower the interfacial density of cations. Interestingly, however, the interfacial densities of weakly adsorbing cations are also more elevated with the strongly adsorbing anions. This is not surprising taking into account the strong binding and correlation between anions and cations.

4. Conclusions

A comparative MD simulation study of the EDL structure and differential capacitance *versus* potential was performed for [BMIM][PF_6] and [BMIM][BF_4] on basal and prismatic graphite and (001) and (011) gold surfaces. The DCs for [BMIM][PF_6] and [BMIM][BF_4] systems are rather similar in magnitude for both surfaces. The variations in DC between 4 and 5 μF cm^{-2} are typical for capacitances previously found for RTILs from simulations[21,23,150–152] and experiments[153] near atomically flat surfaces. In spite of somewhat small changes in DC with respect to applied potential, the well known features predicted using the Kornyshev model, such as surface saturation or minimum and maxima in DCs, were observed for these systems. The DCs for the more asymmetric RTIL ([BMIM][BF_4]) were found to be more structured, *i.e.* larger changes between minima and maxima, which is expected based on basic EDL theories.[100] Also the effect of possible chemisorption of anions onto the electrode surface has been investigated. Without chemisorption the DC was slightly U-shaped near PZC; however for the RTIL with strongly adsorbing anions a bell-shaped DC was observed. The maximum of DC has shifted from +0.9 V to 1.85 V and increased from 7 to 8.7 μF cm^{-2} between strong and weak chemisorption.

Acknowledgements

The authors are grateful to the Department of Energy for financial support under the grant DE-SC0001912 to the University of Utah.

References

1 K. Xu, *Chem. Rev.*, 2004, **104**, 4303–4417.
2 K. Zhu, Q. Wang, J.-H. Kim, A. A. Pesaran and A. J. Frank, *J. Phys. Chem. C*, 2012, **116**, 11895–11899.
3 S. Aparicio and M. Atilhan, *J. Phys. Chem. C*, 2012, **116**, 12055–12065.
4 D. Santamaria-Perez, U. Amador, J. Tortajada, R. Dominko and M. E. Arroyo-de Dompablo, *Inorg. Chem.*, 2012, **51**, 5779–5786.
5 X. Zhang, L. Lu and Y. Cai, *Langmuir*, 2012, **28**, 9593–9600.
6 X. Xia, J. Tu, Y. Zhang, X. Wang, C. Gu, X-b. Zhao and H. J. Fan, *ACS Nano*, 2012, **6**, 5531–5538.
7 S. Lupart, G. Gregori, J. Maier and W. Schnick, *J. Am. Chem. Soc.*, 2012, **134**, 10132–10137.
8 K. Rana, G. Kucukayan-Dogu, H. Sener Sen, C. Boothroyd, O. Gulseren and E. Bengu, *J. Phys. Chem. C*, 2012, **116**, 11364–11369.
9 X. Fan, W. T. Zheng and J-K. Kuo, *ACS Appl. Mater. Interfaces*, 2012, **4**, 2432–2438.
10 G. P. Hao, F. Han, D. C. Guo, R. J. Fan, G. Xiong, W. C. Li and A. H. Lu, *J. Phys. Chem. C*, 2012, **116**, 10303–10311.
11 D. W. Wang, G. Zhou, F. Li, K. H. Wu, G. Q. Lu, H. M. Cheng and I. R. Gentle, *Phys. Chem. Chem. Phys.*, 2012, **14**, 8703–8710.

12 V. Etacheri, R. Marom, R. Elazari, G. Salitra and D. Aurbach, *Energy Environ. Sci.*, 2011, **4**, 3243–3262.
13 J. Liu, Y. Zheng, Y. P. Liao, X. Zeng, G. Ungar and P. V. Wright, *Faraday Discuss.*, 2005, **128**, 363–378.
14 P. Wu, J. Huang, V. Meunier, B. G. Sumpter and R. Qiao, *J. Phys. Chem. Lett.*, 2012, **3**, 1732–1737.
15 O. N. Kalugin, V. V. Chaban, V. V. Loskutov and O. V. Prezhdo, *Nano Lett.*, 2008, **8**, 2126–2130.
16 M. V. Fedorov and R. M. Lynden-Bell, *Phys. Chem. Chem. Phys.*, 2012, **14**, 2552–2556.
17 I. Shim and H. J. Kim, *ACS Nano*, 2010, **4**, 2345–2355.
18 S. Thiemann, S. Sachnov, S. Porscha, P. Wasserscheid and J. Zaumseil, *J. Phys. Chem. C*, 2012, **116**, 13536–13544.
19 A. Labuda and P. Grutter, *Langmuir*, 2012, **28**, 5319–5322.
20 D. Jiang, Z. Jin, D. Henderson and J. Wu, *J. Phys. Chem. Lett.*, 2012, **3**, 1727–1731.
21 R. M. Lynden-Bell, A. I. Frolov and M. V. Fedorov, *Phys. Chem. Chem. Phys.*, 2012, **14**, 2693–2701.
22 J. Sun, G. Chen, Y. Li, R. Jin, Q. Wang and J. Pei, *Energy Environ. Sci.*, 2011, **4**, 4052.
23 S. Kondrat, N. Georgi, M. V. Fedorov and A. A. Kornyshev, *Phys. Chem. Chem. Phys.*, 2011, **13**, 11359.
24 M. Marinescu, M. Urbakh and A. A. Kornyshev, *Phys. Chem. Chem. Phys.*, 2012, **14**, 1371.
25 S. Perkin, *Phys. Chem. Chem. Phys.*, 2012, **14**, 5052–5062.
26 X. Liu, Y. Zhao, X. Zhang, G. Zhou and S. Zhang, *J. Phys. Chem. B*, 2012, **116**, 4934–4942.
27 V. V. Chaban and O. V. Prezhdo, *Phys. Chem. Chem. Phys.*, 2011, **13**, 19345–19354.
28 M. Biera and S. Dietricha, *Mol. Phys.*, 2010, **108**, 211–214.
29 M. J. Earle, J. M. S. S. Esperanca, M. A. Gilea, J. N. C. Lopes, L. P. N. Rebelo, J. W. Magee, K. R. Seddon and J. A. Widegren, *Nature*, 2006, **439**, 831–834.
30 L. P. N. Rebelo, J. N. C. Lopes, J. M. S. S. Esperanca and E. Filipe, *J. Phys. Chem. B*, 2005, **109**, 6040–6043.
31 J. O. Valderrama and P. A. Robles, *Ind. Eng. Chem. Res.*, 2007, **46**, 1338–1344.
32 C. He, J. Li, C. Peng, H. Liu and Y. Hu, *Ind. Eng. Chem. Res.*, 2012, **51**, 3137–3148.
33 K. Paduszynski and U. Domanska, *J. Phys. Chem. B*, 2012, **116**, 5002–5018.
34 D. M. Fox, W. H. Awad, J. W. Gilman, P. H. Maupin, H. C. DeLong and P. C. Trulove, *Green Chem.*, 2003, **5**, 724–727.
35 Z. P. Rosol, N. J. German and S. M. Gross, *Green Chem.*, 2009, **11**, 1453–1457.
36 J. Widegren, E. Saurer, K. Marsh and J. Magee, *J. Chem. Thermodyn.*, 2005, **37**, 569–575.
37 X. Lu, J. Zhou, Y. Zhao, Y. Qiu and J. Li, *Chem. Mater.*, 2008, **20**, 3420–3424.
38 P. N. Tshibangu, S. N. Ndwandwe and E. D. Dikio, *Int. J. Electrochem. Sci.*, 2011, **6**, 2201–2213.
39 V. V. Chaban, I. V. Voroshylova, O. N. Kalugin and O. V. Prezhdo, *J. Phys. Chem. B*, 2012, **116**, 7719–7727.
40 A. Rivera, A. Brodin, A. Pugachev and E. A. Rössler, *J. Chem. Phys.*, 2007, **126**, 114503.
41 F. Shirini, N. G. Khaligh and S. Akbari-Dadamahaleh, *J. Mol. Catal. A: Chem.*, 2012, **365**, 15–23.
42 S. Saravanamurugan, R. Fehrmann and A. Riisager, *Synth. Commun.*, 2012, **42**, 3383–3394.
43 A. B. Menhaj, B. D. Smith and J. Liu, *Chem. Sci.*, 2012, **3**, 3216–3220.
44 N. Zhou, G. Zhao, K. Dong, J. Sun and H. Shao, *RSC Adv.*, 2012, **2**, 9830–9838.
45 Z. Li, H. Tao and R. Yang, *Adv. Mater. Res.*, 2012, **550–553**, 164–169.
46 Y. Funasako, T. Mochida, K. Takahashi, T. Sakurai and H. Ohta, *Chem.–Eur. J.*, 2012, **18**, 11929–11936.
47 F. Gharagheizi, P. Ilani-Kashkouli and A. H. Mohammadi, *Fluid Phase Equilib.*, 2012, **329**, 1–7.
48 L. K. J. Hauru, M. Hummel, A. W. T. King, I. Kilpeläinen and H. Sixta, *Biomacromolecules*, 2012, **13**, 2896–2905.
49 G. V. S. M. Carrera, M. N. Da Ponte and L. C. Branco, *Tetrahedron*, 2012, **68**, 7408–7413.
50 R. Xiong, N. Hameed and Q. Guo, *Carbohydr. Polym.*, 2012, **90**, 575–582.
51 (*a*) J. Pitawala, J. Scheers, P. Jacobsson and A. Matic, *J. Phys. Chem. B*, 2013, **117**, 8172–8179; (*b*) L. Lu, X. Huang and Y. Qu, *J. Solid State Electrochem.*, 2012, **16**, 3299–3305.
52 J.-K. Kim, L. Niedzicki, J. Scheers, C.-R. Shin, D.-H. Lim, W. Wieczorek, P. Johansson, J.-H. Ahn, A. Matic and P. Jacobsson, *J. Power Sources*, 2013, **224**, 93–98.
53 K. Subramaniam, A. Das and G. Heinrich, *Compos. Sci. Technol.*, 2013, **74**, 14–19.
54 E. van de Ven, A. Chairuna, G. Merle, S. P. Benito, Z. Borneman and K. Nijmeijer, *J. Power Sources*, 2013, **222**, 202–209.
55 M. Moniruzzaman and T. Ono, *Bioresour. Technol.*, 2013, **127**, 132–137.
56 N. Böckenfeld, S. S. Jeong, M. Winter, S. Passerini and A. Balducci, *J. Power Sources*, 2013, **221**, 14–20.
57 C. Gerbaldi, J. R. Nair, S. Ferrari, A. Chiappone, G. Meligrana, S. Zanarini, P. Mustarelli, N. Penazzi and R. Bongiovanni, *J. Membr. Sci.*, 2012, **423–424**, 459–467.
58 P. Kiatkittikul, T. Nohira and R. Hagiwara, *J. Power Sources*, 2012, **220**, 10–14.
59 S. Livi, V. Bugatti, L. Estevez, J. Duchet-Rumeau and E. P. Giannelis, *J. Colloid Interface Sci.*, 2012, **388**, 123–129.
60 C. Y. Neo and J. Ouyang, *Electrochim. Acta*, 2012, **85**, 1–8.
61 Z. Z. Yang, L. N. He, Q. W. Song, K. H. Chen, A. H. Liu and X. M. Liu, *Phys. Chem. Chem. Phys.*, 2012, **14**, 15832–15839.
62 D. Weingarth, A. Foelske-Schmitz and R. Kötz, *J. Power Sources*, 2013, **225**, 84–88.
63 J.-K. Kim, L. Niedzicki, J. Scheers, C. R. Shin, D. H. Lim, W. Wieczorek, P. Johansson, J. H. Ahn, A. Matic and P. Jacobsson, *J. Power Sources*, 2013, **224**, 93–98.
64 W. W. Cui, D. Y. Tang and Z. L. Gong, *J. Power Sources*, 2013, **223**, 206–213.
65 J. D. Stenger-Smith, W. W. Lai, D. J. Irvin, G. R. Yandek and J. A. Irvin, *J. Power Sources*, 2012, **220**, 236–242.

66 R. Palm, H. Kurig, K. Tõnurist, A. Jänes and E. Lust, *Electrochim. Acta*, 2012, **85**, 139–144.
67 R. Leones, F. Sentanin, L. C. Rodrigues, I. M. Marrucho, J. M. S. S. Esperança, A. Pawlicka and M. M. Silva, *eXPRESS Polym. Lett.*, 2012, **6**, 1007–1016.
68 R. Leones, F. Sentanin, L. C. Rodrigues, R. A. S. Ferreira, I. M. Marrucho, J. M. S. S. Esperança, A. Pawlicka, L. D. Carlos and M. Manuela Silva, *Opt. Mater.*, 2012, **35**, 187–195.
69 Z. Wang, Y. Cai, T. Dong, S. Chen and X. Lu, *Ionics*, 2012, 1–8.
70 D. T. Dam, X. Wang and J. M. Lee, *RSC Adv.*, 2012, **2**, 10512–10518.
71 J. Shao, X. Li, Q. Qu and Y. Wu, *J. Power Sources*, 2013, **223**, 56–61.
72 H. G. Jung, N. Venugopal, B. Scrosati and Y. K. Sun, *J. Power Sources*, 2013, **221**, 266–271.
73 F. P. Du, J. J. Wang, C. Y. Tang, C. P. Tsui, X. P. Zhou, X. L. Xie and Y. G. Liao, *Nanotechnology*, 2012, **23**(47), 475704.
74 X. Wang, W. S. Liu, X. Lu and P. S. Lee, *J. Mater. Chem.*, 2012, **22**, 23114–23119.
75 R. Wang, *Adv. Mater. Res.*, 2012, **548**, 591–594.
76 F. Cao, G. X. Pan, P. S. Tang and H. F. Chen, *J. Power Sources*, 2012, **216**, 395–399.
77 Q. Cheng, Y. Xia, V. Pavlinek, Y. Yan, C. Li and P. Saha, *J. Mater. Sci.*, 2012, **47**, 6444–6450.
78 J. Jagiello and G. Yushin, *Adv. Funct. Mater.*, 2012, **22**, 1655–1662.
79 D. Wei, M. R. J. Scherer, C. Bower, P. Andrew, T. Ryhänen and U. Steiner, *Nano Lett.*, 2012, **12**, 1857–1862.
80 A. Sumboja, X. Wang, J. Yan and P. S. Lee, *Electrochim. Acta*, 2012, **65**, 190–195.
81 T. Delurio and E. Lee, *Power Electron. Technol.*, 2009, **35**, 14–17.
82 L. B. Bhuiyan, S. Lamperski, J. Wu and D. Henderson, *J. Phys. Chem. B*, 2012, **116**, 10364–10370.
83 L. B. Bhuiyan, D. Henderson and S. Sokolowski, *Condens. Matter Phys.*, 2012, **15**, 23801.
84 L. B. Bhuiyan, C. W. Outhwaite and D. Henderson, *J. Chem. Eng. Data*, 2011, **56**, 4556–4563.
85 L. B. Bhuiyan and D. Henderson, *Mol. Phys.*, 2011, **109**, 1863–1871.
86 L. B. Bhuiyan and D. Henderson, *Mol. Simul.*, 2011, **37**, 269–276.
87 C. W. Outhwaite, S. Lamperski and L. B. Bhuiyan, *Mol. Phys.*, 2011, **109**, 21–26.
88 W. Silvestre-Alcantara, L. B. Bhuiyan and D. Henderson, *J. Chem. Eng. Data*, 2010, **55**, 1837–1841.
89 W. Silvestre-Alcantara, L. B. Bhuiyan, C. W. Outhwaite and D. Henderson, *Collect. Czech. Chem. Commun.*, 2010, **75**, 425–446.
90 D. Henderson and L. B. Bhuiyan, *J. Chem. Theory Comput.*, 2009, **5**, 1985–1989.
91 D. Henderson, S. Lamperski, Z. Jin and J. Wu, *J. Phys. Chem. B*, 2011, **115**, 12911–12914.
92 M. Marinescu, M. Urbakh and A. A. Kornyshev, *Phys. Chem. Chem. Phys.*, 2012, **14**, 1371–1380.
93 A. A. Kornyshev, M. Marinescu, J. Paget and M. Urbakh, *Phys. Chem. Chem. Phys.*, 2012, **14**, 1850–1859.
94 M. Z. Bazant, B. D. Storey and A. A. Kornyshev, *Phys. Rev. Lett.*, 2011, **106**, 046102.
95 Z. Y. Wang and Y. Q. Ma, *Phys. Rev. E: Stat., Nonlinear, Soft Matter Phys.*, 2012, **85**, 062501.
96 T. Nagy, D. Henderson and D. Boda, *J. Phys. Chem. B*, 2011, **115**, 11409.
97 S. Lamperski, C. W. Outhwaite and L. B. Bhuiyan, *J. Phys. Chem. B*, 2009, **113**, 8925–8929.
98 L. Kenji and S. Hirofumi, *J. Chem. Phys.*, 2011, **135**, 244702.
99 D. Henderson and S. Lamperski, *J. Chem. Eng. Data*, 2011, **56**, 1204–1208.
100 A. A. Kornyshev, *J. Phys. Chem. B*, 2007, **111**, 5545–5557.
101 M. Druschler, N. Borisenko, J. Wallauer, C. Winter, B. Huber, F. Endresb and B. Roling, *Phys. Chem. Chem. Phys.*, 2012, **14**, 5090–5099.
102 B. Rolling, M. Druschler and B. Huber, *Faraday Discuss.*, 2012, **154**, 303–311.
103 M. Druschler, B. Huber and B. Roling, *J. Phys. Chem. C*, 2011, **115**, 6802–6808.
104 J. Vatamanu, O. Borodin, D. Bedrov and G. D. Smith, *J. Phys. Chem. C*, 2012, **116**, 7940–7951.
105 J. Vatamanu, O. Borodin and G. D. Smith, *J. Phys. Chem. C*, 2012, **116**, 1114–1121.
106 J. Vatamanu, L. Cao, O. Borodin, D. Bedrov and G. D. Smith, *J. Phys. Chem. Lett.*, 2011, **2**, 2267–2272.
107 L. Xing, J. Vatamanu, G. D. Smith and D. Bedrov, *J. Phys. Chem. Lett.*, 2012, **3**, 1124–1129.
108 C. Merlet, C. Pean, B. Rotenberg, P. A. Madden, P. Simon and M. Salanne, *J. Phys. Chem. Lett.*, 2013, **4**, 264–268.
109 G. Feng and P. T. Cummings, *J. Phys. Chem. Lett.*, 2011, **2**, 2859–2864.
110 D. Jiang, Z. Jin and J. Wu, *Nano Lett.*, 2011, **11**, 5373–5377.
111 P. Wu, J. Huang, V. Meunier, B. G. Sumpter and R. Qiao, *J. Phys. Chem. Lett.*, 2012, **3**, 1732–1737.
112 C. Merlet, B. Rotenberg, P. A. Madden, P.-L. Taberna, P. Simon, Y. Gogotsi and M. Salanne, *Nat. Mater.*, 2012, **11**, 306–310.
113 S. Kondrat and A. Kornyshev, *J. Phys.: Condens. Matter*, 2011, **23**, 022201.
114 P. Wu, J. Huang, V. Meunier, B. G. Sumpter and R. Qiao, *ACS Nano*, 2011, **5**, 9044–9051.
115 S. Tazi, M. Salanne, C. Simon, P. Turq, M. Pounds and P. A. Madden, *J. Phys. Chem. B*, 2010, **114**, 8453–8459.
116 M. Trulsson, J. Algotsson, J. Forsman and C. E. Woodward, *J. Phys. Chem. Lett.*, 2010, **1**, 1191–1195.
117 Y. Lauw, M. D. Horne, T. Rodopoulos and F. A. M. Leermakers, *Phys. Rev. Lett.*, 2009, **103**, 117801.
118 Y. Z. Su, Y. C. Fu, J. W. Yan, Z. B. Chen and B. W. Mao, *Angew. Chem., Int. Ed.*, 2009, **48**, 5148.
119 (*a*) M. T. Alam, J. Masud, Md. M. Islam, T. Okajima and T. Ohsaka, *J. Phys. Chem. C*, 2011, **115**, 19797–19804; (*b*) Md. M. Islam, M. T. Alam and T. Ohsaka, *J. Phys.*

Chem. C, 2008, **112**, 16568–16574; (*c*) M. T. Alam, Md. M. Islam, T. Okajima and T. Ohsaka, *J. Phys. Chem. C*, 2008, **112**, 16600–16608; (*d*) M. T. Alam, Md. M. Islam, T. Okajima and T. Ohsak, *Electrochem. Commun.*, 2007, **9**, 2370–2374.

120 V. Lockett, M. Horne, R. Sedev, T. Rodopoulos and J. Ralston, *Phys. Chem. Chem. Phys.*, 2010, **12**, 12499–12512.

121 F. Silva, C. Gomes, M. Figueiredo, R. Costa, A. Martins and C. M. Pereira, *J. Electroanal. Chem.*, 2008, **622**, 153.

122 X. M. E. Tukerman, B. J. Berne and G. J. Martyna, *J. Chem. Phys.*, 1990, **97**, 1990.

123 M. Kawata and M. Mikami, *Chem. Phys. Lett.*, 2001, **340**, 157–164.

124 M. Kawata and U. Nagashima, *Chem. Phys. Lett.*, 2001, **340**, 165–172.

125 M. Kawata, M. Mikami and U. Nagashima, *J. Chem. Phys.*, 2002, **116**, 3430.

126 M. Kawata, M. Mikami and U. Nagashima, *J. Chem. Phys.*, 2001, **115**, 4457.

127 J. Vatamanu, O. Borodin and G. D. Smith, *Phys. Chem. Chem. Phys.*, 2010, **12**, 170–182.

128 S. K. Reed, O. J. Lanning and P. A. Madden, *J. Chem. Phys.*, 2007, **126**, 084704.

129 J. I. Siepmann and M. Sprik, *J. Chem. Phys.*, 1995, **102**, 511.

130 O. Borodin, *J. Phys. Chem. B*, 2009, **113**, 11463–11478.

131 D. Bedrov and G. D. Smith, *Langmuir*, 2006, **22**, 6189–6194.

132 L. B. Wright, P. M. Rodger, S. Corni and T. R. Walsh, *J. Chem. Theory Comput.*, 2013, **9**, 1616–1630.

133 S. Lamperski, C. W. Outhwaite and L. B. Bhuiyan, *J. Phys. Chem. B*, 2009, **113**, 6569–6574.

134 H. Gerischer, *J. Phys. Chem.*, 1985, **89**, 4249–4251.

135 H. Gerischer, R. McIntyre, D. Scherson and W. Storck, *J. Phys. Chem.*, 1987, **91**, 1930–1935.

136 E. Paek, A. J. Pak and G. S. Hwang, *J. Electrochem. Soc.*, 2013, **160**, A1–A10.

137 R. Costa, C. M. Pereira and F. Silva, *Phys. Chem. Chem. Phys.*, 2010, **12**, 11125–11132.

138 J. Vatamanu, O. Borodin and G. D. Smith, *J. Am. Chem. Soc.*, 2010, **132**, 14825–14833.

139 J. Vatamanu, O. Borodin and G. D. Smith, *J. Phys. Chem. B*, 2011, **115**, 3073–3084.

140 J. Vatamanu, L. Cao, O. Borodin, D. Bedrov and G. D. Smith, *J. Phys. Chem. Lett.*, 2011, **2**, 2267–2272.

141 J. Vatamanu, O. Borodin, D. Bedrov and G. D. Smith, *J. Phys. Chem. C*, 2012, **116**, 7940–7951.

142 C. Merlet, M. Salanne and B. Rotenberg, *J. Phys. Chem. C*, 2012, **116**, 7687–7693.

143 C. Merlet, M. Salanne, B. Rotenberg and P. A. Madden, *J. Phys. Chem. C*, 2011, **115**, 16613–16618.

144 M. Gnahm, T. Pajkossy and D. M. Kolb, *Electrochim. Acta*, 2010, **55**, 6212–6217.

145 G. Feng, J. S. Zhang and R. Qiao, *J. Phys. Chem. C*, 2009, **113**, 4549–4559.

146 S. Wang, S. Li, Z. Cao and T. Yan, *J. Phys. Chem. C*, 2010, **114**, 990–995.

147 L. I. Daikhin, A. A. Kornyshev and M. Urbakh, *J. Chem. Phys.*, 1998, **108**, 1715.

148 L. I. Daikhin, A. A. Kornyshev and M. Urbakh, *Phys. Rev. E: Stat. Phys., Plasmas, Fluids, Relat. Interdiscip. Top.*, 1996, **53**, 6192.

149 W. Gao, T. A. Baker, L. Zhou, D. S. Pinnaduwage, E. Kaxiras and C. M. Friend, *J. Am. Chem. Soc.*, 2008, **130**, 3560–3565.

150 X. Si, S. Li, Y. Wang, S. Ye and T. Yan, *ChemPhysChem*, 2012, **13**, 1671–1676.

151 G. Feng, D-e. Jiang and P. T. Cummings, *J. Chem. Theory Comput.*, 2012, **8**, 1058–1063.

152 A. I. Frolov, K. Kirchner, T. Kirchner and M. V. Fedorov, *Faraday Discuss.*, 2012, **154**, 235.

153 W. Druschler, N. Borisenko, J. Wallauer, C. Winter, B. Huber, F. Endres and B. Roling, *Phys. Chem. Chem. Phys.*, 2012, **14**, 5090.

154 H. Tokuda, K. Hayamizu, K. Ishii, M. Abu Bin Hasan Susan and M. Watanabe, *J. Phys. Chem. B*, 2004, **108**, 16593–16600.

155 M. B. Shiflett and A. Yokozeki, *J. Chem. Eng. Data*, 2007, **52**, 1302–1306.

156 A. Noda, K. Hayamizu and M. Watanabe, *J. Phys. Chem. B*, 2001, **105**, 4603–4610.

157 J. Vila, L. M. Varela and O. Cabeza, *Electrochim. Acta*, 2007, **52**, 7413–7417.

CHAPTER 3

ON THE EFFECT OF CURVATURE ELECTRODE ON ELECTRIC DOUBLE-LAYER CAPACITORS

3.1 Introduction

Capacitance of EDLC is governed by many factors (*1–4*). One of them is nanostructures of the electrodes (*5*). There are many benefits from utilizing electrodes with nanostructures (nanowire, spherical fullerenes, and nanotubes). First, they can provide more surface area facing the electrolyte. In other words, they significantly increase the spaces for forming the electric double layers (EDL). Second, when certain curved structure is comparable with the size of the ions that will compose the EDL, such geometric natures will contribute to additional space for more ions aggregating into EDL, meanwhile causing capacitance enhancement. Therefore, detailed studies on such carbon-based nanostructure electrodes of EDLCs are necessary.

In this chapter, well-designed Molecular Dynamics simulations were conducted (Figure 3.1 shows cation, anion ionic structures, and simulation setups), and we how different nanostructures (e.g., nanotube, C_{20}, C_{60}, and C_{180}) of electrodes changed the capacitance of EDLCs, and the correlations between EDL structures and their corresponding integral capacitance (IC). One of the most significant questions needed to be answered in this chapter is, what kinds of nanostructures of electrodes are able to yield a higher capacitance in EDLCs?

During our studies, we defined two types of nanostructure electrodes. One is an open-structured electrode. The other is a nanoconfinement electrode. Open-structured electrodes mean that the electrodes are completely separated from one another, between them is the bulk electrolyte. The distance between the two electrodes (e.g., tube (3,3), tube (5,5), and tube (7,7)) or nanowall is much larger than the size of the RTIL molecules. In such

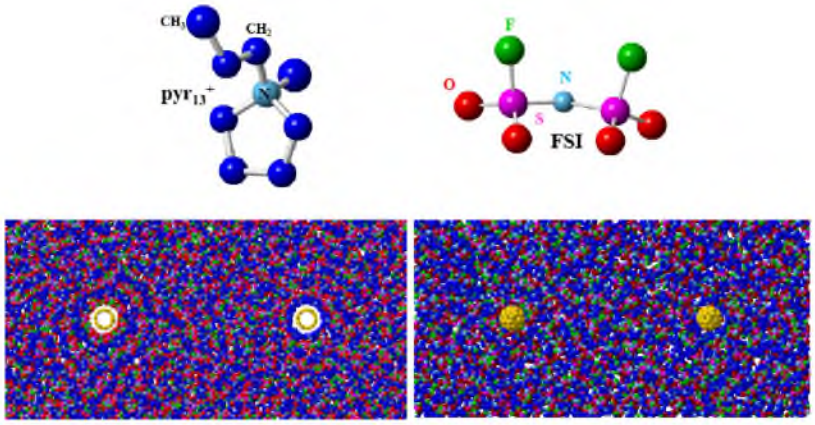

Figure 3.1. Ions chemical structure of N-methyl-N-propylpyrrolidinium (pyr_{13}^{+}) and bis(fluorosulfonyl)imide (FSI). The structures of fullerene and cylinder electrodes are also demonstrated as well their corresponding systems snapshot.

electrodes, the ions that formed the EDL are the same as the ions in bulk electrolyte; they contact with each other (totally opened), and the ions inside the EDL are more structured, layer-by-layer. In contrast, nanoconfinement electrodes have very narrow pore, or nanoscale features, in which the separation between the structural features is only a single ion. Utilizing such electrodes, the electrolyte is confined by the electrodes so that the formed EDL cannot contact the bulk electrolyte directly. The physical behaviors of ions in this confined condition are extremely different compared to those in open structure electrodes.

This research paper published in the Physical Chemistry Letter shown below comprised studies of both open structures electrodes and nanoconfinement electrodes. Here I need to declare that the contribution of this thesis is only toward the open structures electrodes part of the article. The details of the article are shown in section 3.4.

3.2 Further Discussion

IC is defined as 2*q/ΔU, where q is the charge dialed on the ion, and ΔU is the potential between the two electrodes. Figure 3.2 compares the IC as a function of the distance away from the electrode surface for various geometries of electrodes, including corrugated and rod-like single nanocarbon chains in which the corrugated nanowires have the groove structures and can generate a deep electric field, as well as accommodate more ions; spherical curvature electrodes with radius of 1.89 $\mathring{A}$ for C_{20}, 3.45 $\mathring{A}$ for C_{60}, and 6.22 $\mathring{A}$ for C_{180}; cylindrical single-walked carbon nanotubes (SWCNTs) electrodes of (3,3), (5,5), and (7,7) with radii of 1.93 $\mathring{A}$, 3.39 $\mathring{A}$ and 6.102 $\mathring{A}$, respectively; and atomically flat surfaces electrode consisting flat grapheme layers. Nano single carbon chains/wires can be consider as an ideal case of single-chain conductor; however, isolated C_{20} and (3,3) SWCNT's stability and conductive properties are different due to their structural elements and can be embedded into other structures. In Figure 3.2, we calculated the IC near the nanowire electrodes. Among them, the corrugated single carbon wire electrodes generated higher capacitance around 265 F/g during the [pyr_{13}][TFSI] ionic liquid electrolyte. A rod-like nanowire electrode system generated 240 F/g capacitance with [pry_{13}][FSI] and [EMIM][PF_6] electrolytes, which is 10 F/g smaller than a corrugated nanowire system. Later we will discuss the capacitance of atomic flat surface electrode systems, and the capacitance of corrugated nanowire is four factors higher than that of atomically flat surface systems.

Due to the rough edges of the single carbon chain shape, this electrode is physically producing a higher local electrostatic field near the surface; meanwhile, it is attracting

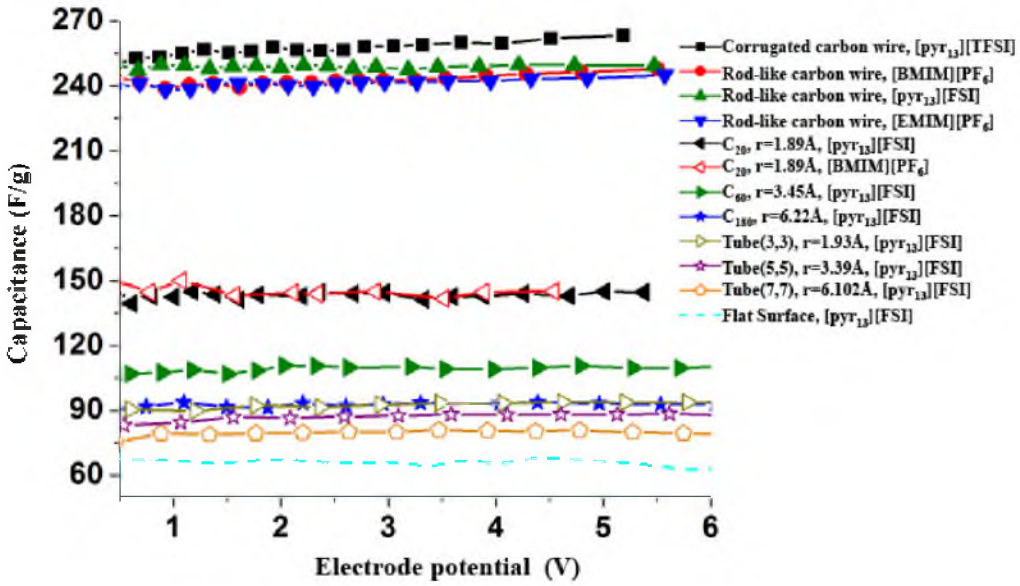

Figure 3.2. Comparison of Integral Capacitance (IC) for all systems studies in this work.

more ions onto the near surface, which strongly enhances the segregation densities of the electrolytes. The more ions are aggregated the higher the charge densities. This means that this shape of electrodes generates a larger capacitance compared to an atomically flat surface. The atomically corrugated structure consists of many identical repeated groove units on the surface of the electrodes, which faces the bulk electrolyte. The groove is 7.1 $\mathring{A}$ deep and 7 $\mathring{A}$ wide. By designing a proper ion size of electrolyte, which is compatible with the size of the groove width and depth, a faster accumulative rate and a well-shaped EDL structure with more ions will be achieved near the electrode surface, and EDLC with this kind of electrode will have a greatly increased capacitance.

Next, we analyzed the capacitance for curved electrodes. When the radius of the electrode is decreased and the surface area per unit increases, a larger capacitance is observed per surface area. For example, C_{20}, which has the smallest radius of 1.89 $\mathring{A}$ and the largest surface area, has a capacitance of 150 F/g; this is a 50% capacitance decrease compared to an atomically corrugated nanowire surface. Two kinds of electrolyte pairs, [pry_{13}][FSI] and [BMIM][PF_6], were examined; however, as shown in Figure 3.2, different electrolyte materials have not made a significant change in their IC. When we increase the radius of the spherical electrode to 3.45 $\mathring{A}$, which corresponds to the dimensions of electrode of C_{60}, it has an IC of 110 F/g capacitance, which is 40 F/g smaller than the IC of C_{20} system and 150 F/g (more than 50%) smaller than that of corrugated nanowire. Increasing the radius even more to 6.22 $\mathring{A}$, which is the same dimensions as the C_{180} electrode system, that system only has an IC of 91 F/g capacitance. It is 60 F/g smaller than the IC of C_{20} electrode system, 40 F/g smaller than C_{60} and 170 F/g smaller than a single carbon nanowire.

Nanotubes capacitance enhancement is much smaller than that of spherical fullerenes. With the same electrolyte materials, [pyr_{13}][FSI], tube (3,3), which has the largest surface area (radius = 1.93 $\mathring{A}$) among the three, it has the highest IC of only 90 F/g. This value is nearly the same as a spherical C_{180} system, which has the smallest IC among all the fullerenes. However, it is still larger than an atomically flat surface system. When we increase the radius to 3.39 $\mathring{A}$, which corresponds to tube (5, 5), its IC of around 88 F/g is even smaller compared to tube (3,3). It is 2 F/g smaller than tube (3, 3) and smaller than all the spherical systems as well as nanowires. Even the larger radius of the tube (7, 7) only has an IC of 82 F/g, which is the smallest IC among all the curvature shapes of electrodes and the one closest to an atomically flat surface.

Last, the atomically flat surface electrode system, shown in Figure 3.2, only has an IC

of 65 F/g, which is 17 F/g less than tube (7,7), 23F/g smaller than tube (5,5), and 25 F/g smaller than tube (3,3). Also it is 56% smaller than C_{20} (radius = 1.9 $\AA$) and 75% smaller than the nanowire system.

We analyzed the integral charge densities so that we can better explain the trend of IC. Starting from the surface of the electrodes (0 $\AA$), we divided EDL structures into several shells along the z-direction. Therefore, the volume (ΔV) of each shell is dependent of their radius dz, a small distance of the thickness of each shell. For example, the volume of the first shell for the spherical system is defined as $\frac{4}{3}\pi(r_1^3 - r_0^3)$, where r_0 is the radius of the corresponding spherical electrode, and r_1 is the distance between the end of first shell and the surface of its electrode. Then we sum up all the charge carried by ions in a certain shell and divide by the volume of the shell. For the spherical electrode systems, the calculation is the volume change, $\frac{4}{3}\pi(r_1^3 - r_0^3)$, divided by the surface area of the electrode ($A_{elelctrode}$). We described this calculation as $Q_{int}/A_{elelctrode}$, and the equation for Q_{int} is

$$Q_{int} = \frac{\int_{r_0}^{r_i} q \cdot 4\pi r^2 \cdot dr}{\Delta V}$$

Figure 3.3(a) and (b) show integral charge densities for spherical systems and atomic flat surface systems, when the dialed potential on each electrode is -2 V and +2 V (the total is 4 V), respectively. The integral charge densities for nanowire, nanotube, and atomic flat surface, when the dialed potential on each electrode are -2 V and +2 V, are shown in Fig 3.3 (c) and (d). From Figure 3.3 (a), we can clearly see that the integral charge density for the first shell that the C_{20} electrode system has is the largest integral charge density of 4.6 electrons per nm^3 per 1 nm^3 of electrode surface are (e/nm^3/1 nm^2) followed by C_{60}. That electrode system has 2.9 (e/nm^3/1 nm^2), which is 1.8 (e/nm^3/1 nm^2) smaller than that of the C_{20} system. When the radius becomes larger than the C_{180} electrode system, it is only has 1.9 (e/nm^3/1 nm^2) integral charge density. That is 1 (e/nm^3/1 nm^2) smaller than that of the C_{60} electrode system and 2.7 (e/nm^3/1 nm^2) smaller than the C_{20} electrode system. These results strongly correspond to their IC. The C_{20} system has the largest IC of 150 F/g, the C_{60} system has 110 F/g, and the C_{180} has 91 F/g. An atomic flat surface electrode system only has an IC of 62 F/g, which means that it has the lowest integral charge density of 1 (e/nm^3/1 nm^2). Apparently, the amount of charge it can hold per unit determines how much capacitance the corresponding system has. Figure 3.3(b) demonstrates the same trend of integral charge density for spherical and flat surface systems. Near positive electrodes (+2 V), a C_{20} system has an even bigger absolute integral charge density of 6.7 (e/nm^3/1 nm^2). The same phenomenon occurred with the C_{60} system as well; it has a value of 4.1

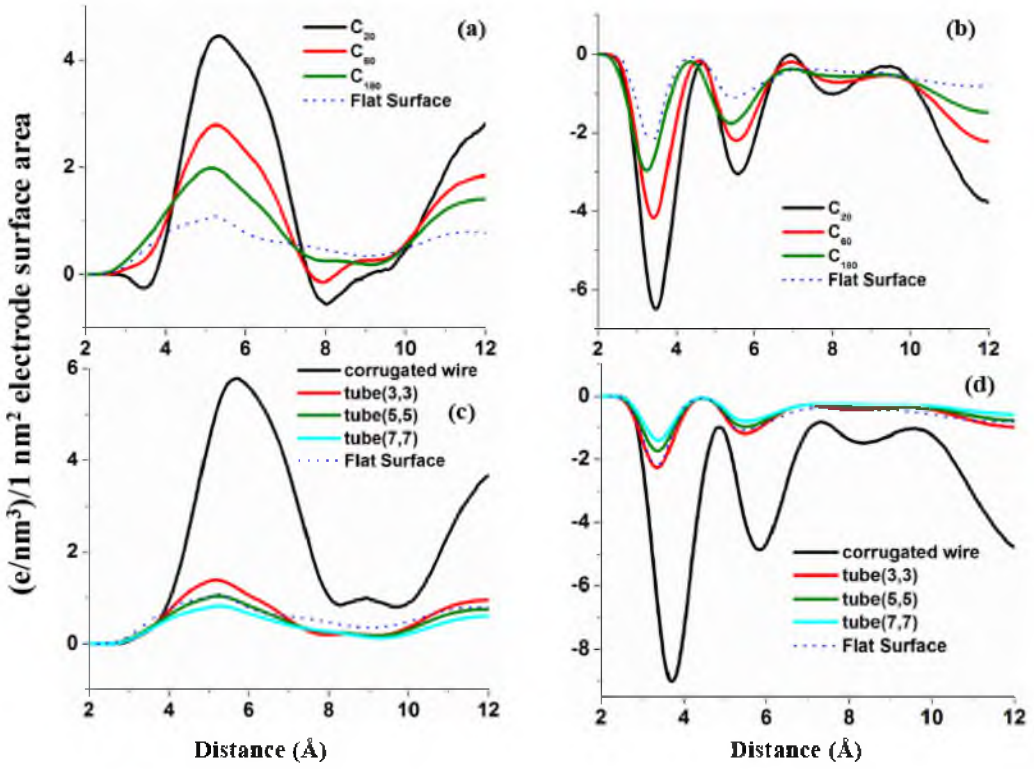

Figure 3.3. Charge density per unit volume (nm^3) per 1 nm^2 surface area of electrode (a) -2 V for spherical system and atomic flat surface system; (b) +2 V spherical system and atomic flat surface system; (c) -2 V for nanowire, nanotube, and atomic flat surface systems; (d) +2 V for nanowire, nanotube, and atomic flat surface systems.

($e/nm^3/1\ nm^2$), which is 1.2 ($e/nm^3/1\ nm^2$) larger than its negative electrode, but 2.6 ($e/nm^3/1\ nm^2$) less than C_{20}'s. As for the C_{180} system, its first shell value on positive electrodes is 2.9 ($e/nm^3/1\ nm^2$), which is 1.2 ($e/nm^3/1\ nm^2$) smaller than C60s and 3.8 ($e/nm^3/1\ nm^2$) smaller than C_{20}'s. These results also follow the same trend and highly correspond with the result of their IC.

Next, we illustrate the integral charge densities of nanowire, nanotube, and atomic flat surface systems. In Figure 3.3 (c) we can see, on the negative side of electrode, a corrugated nanowire system has a much higher charge density of 5.9 ($e/nm^3/1\ nm^2$). This value is 4.4 ($e/nm^3/1\ nm^2$) larger than that of the tube (3,3) system, which only has 1.5 ($e/nm^3/1\ nm^2$). Tube (5,5) has a value of 1 ($e/nm^3/1\ nm^2$). This is 4.9 ($e/nm^3/1\ nm^2$) smaller than that of a corrugated nanowire system. Surprisingly, in this instance the atomic flat surface has almost the same density as tube (5,5), which is bigger than tube (7,7)'s density of only 0.7 ($e/nm^3/1\ nm^2$). However, in the IC profiles, tube (7,7)'s IC is 82 F/g bigger than the flat surfaces IC, which is 62 F/g. With the positive electrode side, shown in Figure 3.3 (d), the nanowire system still has the larger absolute density value of 9.1 ($e/nm^3/1\ nm^2$). However, in this instance, tube (3,3) and atomic flat surface systems have the same integral charge density of 2.1($e/nm^3/1\ nm^2$), which are 7 ($e/nm^3/1\ nm^2$) smaller than the nanowires. Tube (5,5) only has a 1.8 ($e/nm^3/1\ nm^2$) charge density, which is 7.3 ($e/nm^3/1\ nm^2$) smaller than that of the nanowire and 0.3 ($e/nm^3/1\ nm^2$) smaller than that of tube (3,3) and the atomic flat surface. Tube (7,7) has the smallest charge density of 1.6 ($e/nm^3/1\ nm^2$). This is 7.5 (e/nm3/1 nm2) smaller than the nanowires, 0.5 ($e/nm^3/1\ nm^2$), smaller than tube (3,3) and the atomic flat surface, and 0.2 ($e/nm^3/1\ nm^2$) smaller than tube (5,5). Except for the atomic flat surface, all the other systems have great congruence with their IC profiles.

Last, corrugated nanowire has 5.9 ($e/nm^3/1\ nm^2$) charge density on the negative electrode. That is 1.3 ($e/nm^3/1\ nm^2$) larger than the C_{20} system ($e/nm^3/1\ nm^2$). On the positive electrode corrugated nanowire (9.1 $e/nm^3/1\ nm^2$), it is 2.4 ($e/nm^3/1\ nm^2$) larger than that of the C_{20} system (6.7 $e/nm^3/1\ nm^2$). This also agrees with its IC.

Clearly, nanowire structures have the highest integral charge densities and correspond to their highest IC values among all the systems we examined. Nanowire structures are followed by the integral charge densities of fullerene electrode structure systems ($C_{20} > C_{60} > C_{180}$). The rank of their integral charge densities has strong agreement with their corresponding IC, as well as the matter of its positive electrode or negative electrode. According to their IC values, all the nanotubes integral charge densities are larger than an atomic flat surface system, but only tube (3,3)'s value is larger than atomic flat surfaces.

Tube (5,5) and tube (7,7) are smaller than that of a flat surface. Nanotubes integral charge density still follows the order of tube (3,3) > tube (5,5) > tube (7,7), which is exactly the same order we observed from their IC profile.

3.3 References

[1] Barbieri, O.; Hahn, M.; Herzog, A.; Ktz, R. *Carbon* **2005**, *43*, 1303–1310.

[2] Simon, P.; Gogotsi, Y.; Trans. R. *Soc. London, Ser. A* **2010**, *368*, 3457–3467.

[3] Largeot, C.; Portet, C.; Chmiola, J.; Taberna, J. C.; Gogotsi, Y.; Simon, P. *J. Am. Chem. Soc.* **2008**, *130*, 2730–2731.

[4] Xing, L.; Vatamanu, J.; Smith, G. D.; Bedrov, D. *J. Phys. Chem. Lett.* **2012**, *3*, 1124–1129.

[5] Vatamanu, J.; Cao, L.; Borodin, O.; Bedrov, D.; Smith, G. D. *J. Phys. Chem. Lett.* **2012**, *2*, 2267–2272.

3.4 Increasing Energy Storage in Electrochemical Capacitors with Ionic Liquid Electrolytes and Nanostructured Carbon Electrodes

THE JOURNAL OF PHYSICAL CHEMISTRY Letters

Letter

pubs.acs.org/JPCL

Increasing Energy Storage in Electrochemical Capacitors with Ionic Liquid Electrolytes and Nanostructured Carbon Electrodes

Jenel Vatamanu, Zongzhi Hu, and Dmitry Bedrov*

Department of Materials Science & Engineering, University of Utah, 122 South Central Campus Drive, Room 304, Salt Lake City, Utah 84112, United States

Carlos Perez and Yury Gogotsi

Department of Materials Science & Engineering, and A.J. Drexel Nanotechnology Institute, Drexel University, 3141 Chestnut Street, Philadelphia, Pennsylvania 19104, United States

Supporting Information

ABSTRACT: The potential pathways to increase the energy storage in electric double-layer (EDL) supercapacitors using room-temperature ionic liquid electrolytes and carbon-based nanostructured electrodes are explored by molecular dynamics simulations. A systematic comparison of capacitances obtained on nanoparticles of various shape and dimensions showed that when the electrode curvature and the length scale of the surface roughness are comparable to ion dimensions, a noticeable improvement in the capacitive storage is observed. The nanoconfinement of the electrolyte in conductive electrode pores further enhances the capacitance due to mismatch in ion−electrode surface interactions and strong electrostatic screening. We show that nanoporous structures made of arrays of conductive carbon chains represent a synergy of all three favorable factors (that is, high curvature, atomic scale roughness, and nanoconfinement) and can generate non-Faradic capacitance ranging from 260 to 350 F/g, which significantly exceeds the performance of the current generation of nanostructured electrodes.

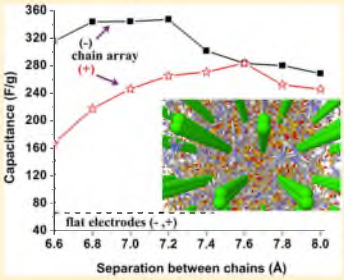

SECTION: Energy Conversion and Storage; Energy and Charge Transport

Electric double-layer capacitors (EDLCs or supercapacitors) have been extensively explored as promising energy storage devices in which the charge/energy is stored through ion rearrangement in the interfacial layer between the electrode and electrolyte. Substantial efforts have been dedicated to improve the energy density of EDLCs through design of nanostructured electrodes with a high specific surface area and understanding the interplay between various phenomena defining the performance of these devices. Several experimental, theoretical, and simulation studies conducted on this topic over the past few years clearly demonstrated the complexity of physical phenomena and correlations governing the EDL capacitance. For example, it was shown that the capacitance could be strongly influenced by thermodynamic conditions,[1] electrolyte chemical structure,[2−4] and nanoconfinement,[5,6] as well as by the electrode surface roughness/nanostructure[7,8] and conductivity. While our detailed understanding of these complex systems is still in its infancy, there is sufficient evidence that envisioned breakthroughs for supercapacitors must come from the optimal design of nanostructured electrode/electrolyte combinations.

Utilization of nanostructured electrodes provides several beneficial factors; (i) it can significantly increase the surface area exposed to the electrolyte and hence available for EDL formation, (ii) when the nanoscale structural features on the electrode surface, for example, surface curvature or atomic scale roughness, are comparable to the size of ions comprising the EDL, additional geometric factors can facilitate the ion separation in the EDL and lead to a capacitance enhancement, and finally, (iii) as has been demonstrated in several experiments[2−5] and simulations[9−12] as well as explained by theoretical models,[13−15] the confinement of the electrolyte in charged nanoporous electrodes can be accompanied by qualitatively different physical behavior, for example, strong (exponential-like) screening of electrostatic interactions between ions due to electronic polarization of the electrode can lead to super ionic states of densely packed ions of the same charge,[14] which can also result in the enhancement of capacitive storage.[6,10] However, the plethora of possible nanostructured electrode architectures as well as the complicated interplay between electrode/electrolyte structural characteristics and the capacitor performance makes the

Received: July 15, 2013
Accepted: August 7, 2013

rational design of novel supercapacitors a daunting task. The most frequently utilized electrodes, such as activated or carbide-derived carbon (CDC), are structurally heterogeneous amorphous materials consisting of a variety of nanostructural elements, including flat graphene sheets, 1D and 2D curved surfaces, and even carbon single chains.[16]

Moreover, the content of these structural elements as well as their characteristic shape and size distributions can depend on (and hence can be controlled by) electrode preparation conditions (e.g., high- or low-temperature synthesis of CDC). In this Letter, we attempt to provide guidance to the process of designing optimal nanostructured electrodes by systematically analyzing several correlations between EDL capacitance and nanostructural features of electrodes. Specifically, we focus on two important questions: Which nanostructured elements are most beneficial to manipulate with in order to increase the energy storage in EDLC? What are the theoretically possible limits of the energy storage in EDLCs that can be achieved using nanostructured electrodes and room-temperature ionic liquids (RTILs)? Addressing these questions provides guidance toward designing the next generation of nanostructured electrodes for high-energy-density supercapacitors.

For EDLCs, RTILs are widely considered the electrolyte of the future. RTILs are solventless electrolytes with many properties that make them attractive for electrochemical energy storage: high chemical and thermal stability, negligible vapor pressure, a broad electrochemical stability potential window, and an immense parameter space in terms of ion selection and resulting properties. While there are a number of studies of the EDL in RTIL electrolytes on flat surface electrodes, studies of complex electrode geometries, such as those of exohedral carbon nanomaterials, are rare in the literature and so far focused on organic electrolytes.[17]

For the purpose of this work, we divided the nanostructured electrodes in two categories, open-structure (or exohedral) and nanoconfinement electrodes. In our definition, the open-structure electrodes are those where the electrode nanostructural features are sufficiently separated from each other by an electrolyte such that there is no electrolyte nanoconfinement. In other words, the pore size or the separation between nanoscale features (e.g., nanotubes or fullerenes) is significantly larger than the dimensions of electrolyte molecules (i.e., RTIL ions), and hence, the EDLs formed on such electrode surfaces are in contact with the bulk electrolyte. This definition would include flat surfaces as well as porous systems with wide pores, for example, for a typical RTIL electrolyte, this would correspond to pores wider than 40 Å, which is about five times larger than the size of individual ions and about twice the width of highly structured EDLs near flat surfaces in typical RTILs. The kinetic limitations in EDLCs currently observed[18,19] for RTIL electrolytes (charging rate and temperature of operation) are addressed by the use of these exohedral materials, and therefore, this type of electrode has received significant attention. In contrast, electrodes with relatively narrow pores or with arrangement of nanoscale features (e.g., nanotube bundles) where the separation between those structural features is comparable to a single ion in size will be categorized here as nanoconfinement electrodes. In such electrodes, the electrolyte experiences confinement between the electrode surfaces, and therefore, the formed EDL is not in direct contact with the bulk electrolyte. As we will show below, the physical phenomena and behavior of the electrolyte in such confined environments can be significantly different than that on open-structure electrodes.

The simulation setup consisted of two electrodes and a RTIL electrolyte being placed between the electrodes. The simulations for open-structure electrodes such as fullerenes, nanotubes, and single carbon chains were performed using the constant electrode charge methodology described in ref 30, while simulations for flat and nanopatterned surfaces as well as for electrodes with nanoconfinement (slit nanopores and single-chain arrays) were conducted using a constant applied potential approach, as described in ref 20. In the former approach, the partial atomic charges for surface atoms were predefined and homogeneously distributed. In the latter approach, electrodes were modeled as conductors with charges determined using self-consistent iterations for electrostatic energy minimization with respect to electrode charges.[21,22] Positions of electrode atoms were fixed in all simulations. For description of the RTIL electrolytes, a combined explicit atom/united atom force field that has been developed and validated previously[20,23,24] was utilized. The equations of motion were integrated using the RESPA algorithm[25] as described in ref 26. The temperature was maintained at 393 K using Nosé–Hoover thermostat chains.[27] More detailed descriptions of the systems setup and simulation methodologies and protocols are given in the Supporting Information. For each system, production runs over 10 ns were conducted for each value of the potential difference investigated. The collected statistics on electrode charges and ion densities were subsequently used to derive electrode potentials and capacitances. The potentials of zero charge (PZCs) were computed from the simulations with uncharged electrodes. The electrode potential was defined as the difference between the Poisson potential on the electrode surface and in bulk electrolyte minus the PZC. The differential capacitance (DC) was computed as the numerical derivative of the electrode charge versus electrode potential as described in ref 28. The integral capacitance (IC) was computed as the electrode charge at a given potential divided by the electrode potential.

Open Structures. While the role of electrolyte chemistry on the formation of the EDL and the capacitance was investigated both by experiments and simulations, understanding of the influence of the electrode surface geometry on the EDL capacitance is still rather poor. We begin our discussion by analyzing the capacitance generated on electrodes with several common surface geometries such as atomically flat, rough, and curved. Figure 1 compares the ICs at a 4 V potential difference between electrodes for the following electrode geometries: (i) flat surfaces consisting of graphene layers; (ii) atomically rough or nanopatterned surfaces, (iii) cylindrical electrodes consisting of (3,3), (5,5), and (7,7) metallically conducting single-walled carbon nanotubes (SWCNTs) with corresponding nanotube radii of 1.9, 3.4, and 6.1 Å, respectively; (iv) spherical particle electrodes with radii of 1.9, 3.45, and 6.4 Å represented here by C_{20}, C_{60}, and C_{180} fullerenes, respectively; and (v) carbynes, single carbon chains. The latter represent an ideal case of a single-chain conductor. While the stability and conductive properties of isolated C_{20} and (3,3) SWCNTs are not practical, these structural elements can be embedded into other structures and also represent a limiting case of highly curved surfaces in porous carbons such as CDC or activated carbon. Similarly, the electrochemical stability and feasibility of manufacturing electrodes comprised of linear carbon chains is yet to be proven, but from a fundamental understanding point

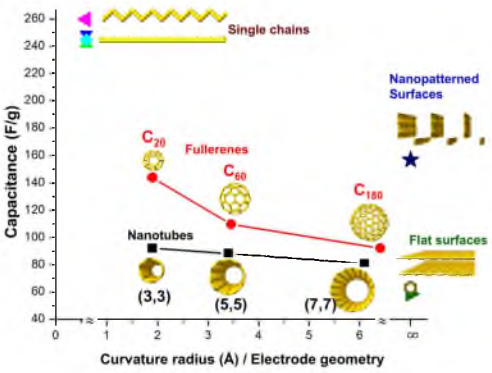

Figure 1. The capacitance as a function of electrode surface curvature radius and geometry for various open structure electrode geometries as obtained from MD simulations at the 4 V potential difference between electrodes. For majority of the open structures (i.e., flat surfaces as well as well-separated nanotubes, spherical particles, and carbon chains), the DC is almost independent of the potential in the potential window between 0 and 4 V, and hence, the ICs on individual electrodes are very similar. However, for atomically corrugated nanopatterned surfaces, the charge accumulation/separation is asymmetric with electrode polarity, and therefore, an average value for positive and negative electrodes is shown. The ICs obtained for rod-like carbon chains immersed in [EMIM][TFSI] (green ▲), [pyr_{13}][FSI] (turquoise ◆), [BMIM][PF_6] (blue ▼), and an all-trans carbon chain in the [pyr_{13}]/[TFSI] (pink ◀) are shown.

of view, this system represents the limiting case where the thickness (diameter) of the electrode nanostructure becomes comparable to single-atom dimensions. To facilitate the comparison of capacitances obtained on electrodes with different geometries, we have normalized them per unit mass of electrode atoms that are in direct contact with the electrolyte. Where it was possible to define a surface area, we also report the capacitance per unit of specific surface area.

For an atomically flat graphite electrode, the IC of the RTILs ranges between 4.5 and 5.3 $\mu F/cm^2$ or 55 and 70 F/g, depending on the electrolyte chemical structure. For example, the average IC shown in Figure 1 for a basal plane (flat) graphite electrode is 65 F/g (4.93 $\mu F/cm^2$) for [C_2mim][TFSI], 61.6 F/g (4.67 $\mu F/cm^2$) for [pyr_{13}][FSI], and 56.6 F/g (4.3 $\mu F/cm^2$) for [C_8mim][TFSI]. In our normalization of capacitance, we assume that the surface graphene layer is exposed to electrolyte only on one side, that is, its capacitances per unit surface area and per unit mass are related as 1 $\mu F/cm^2$ = 13.2 F/g. In principle, one can consider the case where the graphene layer is exposed to electrolyte with both sides (delaminated graphene), which would lead to doubling of the electrolyte accessible surface area and, hence, will roughly double the capacitance values given above. This will be the case for pillared or suspended single-layer graphene.

Next, we examine curved electrode surfaces. As the curvature of the electrode surface increases (decreasing radius), larger capacitances per unit surface area are observed. For nanotubes, the enhancement is rather small. Specifically, for [pyr_{13}][FSI] electrolyte, the average IC for a tube with a very small 1.9 Å radius is 92 F/g (or 8 $\mu F/cm^2$), which is 50% larger than that on a flat surface. For the larger tubes (with radii of 3.4 and 6.4 Å) that can be manufactured in bulk quantities, the IC decreases to 88 (6.6 $\mu F/cm^2$) and 80 F/g (or 6 $\mu F/cm^2$), respectively. Similarly, a relatively weak increase of capacitance with decreasing nanotube radius was recently observed in molecular dynamics simulations of another RTIL by Feng et al.[29] Spherical electrodes increase the capacitances to a somewhat larger extent than cylindrical ones. The spherical electrode with the average radius of 6.4 Å (C_{180}, corresponding to the pore radius in many porous carbons) shows the IC almost similar to that of the most curved nanotube (1.9 Å radius) investigated. Decreasing the sphere radius to 3.45 Å (C_{60}) results in an average IC of 110 F/g (8.7 $\mu F/cm^2$), which is 78% larger than on a flat surface. Decreasing further the sphere radius to 1.9 Å (C_{20}, corresponding to the smallest pores in carbon materials) leads to 144 F/g (≈12.5 $\mu F/cm^2$) or a 132% increase compared to the IC obtained on flat surfaces. Qualitatively similar trends in capacitance were observed by Feng et al.[30] from simulations of systems consisting of two or three concentric spheres (onions); however, our simulations predict that much smaller radii of electrode particles are required to reproduce the extent of enhancement in capacitance observed in ref 30.

The observed changes in capacitance can be primarily explained by increased volume of the surface layer available for the ion adsorption on the curved surface compared to the volume near the same surface area but on a less curved or flat electrode. For example, a simple calculation shows that if we consider the thickness of the first layer to be 5 Å and the surface location to be a nanotube (or fullerene) radius plus one atomic van der Waals diameter (~3 Å) from the nanoparticle center, then the volume of the surface layers for nanotubes with 1.9 and 6.4 Å radii should be about 50 and 20%, respectively, larger than the volume of the surface layer on a flat surface with equivalent surface areas. The capacitance values reported above are very consistent with this geometric trend. The increased volume of the surface layer on highly curved electrodes allows electrolyte to bring more counterions to compensate for the electrode surface charge. While it is clear that surface curvature increases the capacitance, it only becomes significant when the radius of the curvature is small. This allows us to conclude that the curvature effects can only contribute a modest extent to the capacitance enhancement observed experimentally on, for example, onion-like carbon electrodes[31−33] where the outer layer radius of the onion typically is much larger than 6 Å. A significant (i.e., more than doubling) increase in capacitances for spherical electrodes (compared to those for flat surfaces) would require a curvature radius as small as 1.9 Å, as in the C_{20} fullerene.

Next, we analyze the capacitance near atomically corrugated nanopatterned surfaces. The rough edges of the nanopatterned surfaces are expected to generate large local electrostatic fields, promoting the ion segregation near the electrode surface at low electrode potentials and therefore generating a larger capacitance[7,8] than on atomically flat surface electrodes. Atomically rough surfaces can be populated with random structural features using chemical etching or other surface modifications. For the particular case illustrated here, the atomically rough surfaces were generated from graphite ABAB staking in such a way that small surface grooves 7.1 Å deep and 7 Å wide were exposed to the electrolyte (see Figure 1). These surfaces with groove widths comparable to the ion sizes have modified the EDL structure and accumulation rates (versus electrode potential) of the electrolyte near the surface, generating surprisingly large capacitance per specific surface

dx.doi.org/10.1021/jz401472c J. Phys. Chem. Lett. 2013, 4, 2829−2837

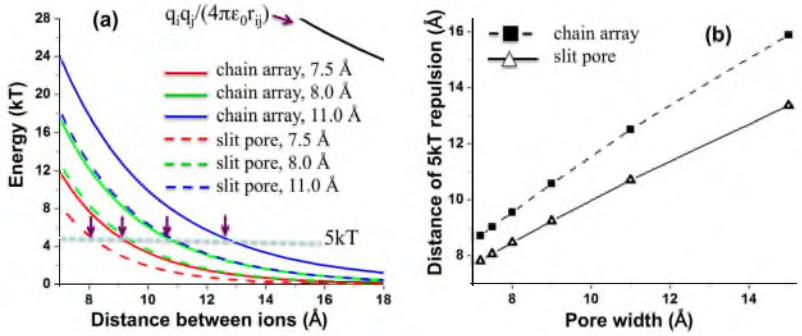

Figure 2. (a) The total electrostatic energy between two ions inserted into a porous electrode consisting of an array of carbon chains and a slit geometry pore as a function of the distance between the ions and the separation between the chains/walls. For comparison, the unscreened electrostatic energy is also shown as a black line. Also shown are the $5kT$ energy level and the corresponding separations for each curve. (b) The separations between two ions at which the electrostatic repulsion is reduced below $5kT$ plotted as a function of the pore width.

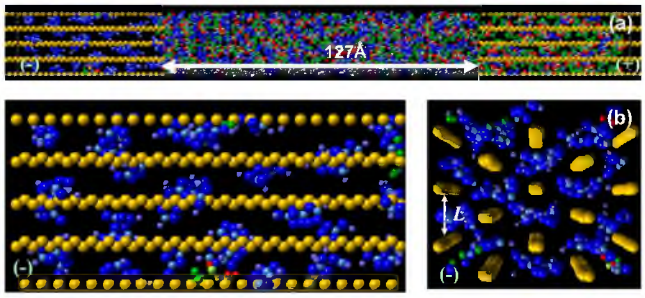

Figure 3. (a) Snapshot of the simulation cell setup. [EMIM][TFSI] RTIL between negatively charged (left) and positively charged (right) electrodes. (b) Lateral and side views of the negative electrode comprised of a single-chain array and filled with EMIM counterions at a −2.0 V electrode potential.

area. For example, the average (over two electrodes) IC of the electrode with a corrugated surface shown in Figure 1 is 157 F/g (or 7.5 μF/cm^2), which is factor of 2−3 higher than those obtained on atomically flat basal plane graphite. Note that in the case of a nanopatterned surface, we observed a noticeable asymmetry in the capacitance as a function of electrode polarity, with the negative electrode generating up to 20% larger IC than the positive one. More detailed discussion of correlations between the capacitance and EDL structure on atomically corrugated surfaces can be found in refs 7 and 8.

Finally, our simulations reveal that the largest enhancement of the capacitance is obtained for electrodes made of conductive carbon chains (carbynes). Linear chains of carbon were observed experimentally in TiC−CDC[16] and B_4C−CDC.[34] We modeled carbynes both as a 1D sequence of carbon atoms (i.e., rod-like =C=C=C= or −C≡C−C≡C−) as well as sequences of atoms arranged in a zigzag shape (all-trans) conformation. Both geometries have produced similar capacitances of around 240−250 F/g. This enhancement was obtained for several different electrolytes (i.e., [pyr_{13}][FSI], [EMIM][TFSI], [BMIM][PF_6]), therefore indicating that the chemical structure of the electrolyte does not play an important role and the observed increased values of the capacitance is primarily correlated with the electrode geometry/curvature. Due to extreme curvature effects and atomic-scale corrugation, electrodes comprised of single carbon chains immersed in RTILs can generate a capacitance that is up to a factor of 4 larger than the capacitances on flat surfaces with one side exposed toward the electrolyte, or almost double the IC of a single graphene layer immersed in electrolyte with both sides exposed to the electrolyte. Taking into account the relatively weak dependence of the capacitance on the chemical structure of the electrolyte, we believe that the capacitances shown in Figure 1 for the linear chains are close to a theoretical limit that can be expected for open structures.

Electrodes with a Nanoconfined Electrolyte. Recent experiments have indicated that when the electrolyte is confined into pores with at least one dimension comparable to ion sizes, then a twofold capacitance enhancement can be observed.[2−6] Theoretical models[14] and molecular simulations[9] showed that for slit-like nanopores, the primary mechanism for the observed capacitance enhancement is an abrupt separation of ions inside of the nanopores due to expulsion of co-ions when the electrode potential reaches a certain threshold. The complete ion separation is facilitated by strong screening of electrostatic interactions between ions confined in nanopores with polarized conductive walls, which leads to an effective short-range ion−ion electrostatic interaction, as illustrated in Figure 2a for two positive ions inside of negatively charged slit-pores as a function of ion separation and pore width. The short-range interaction

dx.doi.org/10.1021/jz401472c J. Phys. Chem. Lett. 2013, 4, 2829−2837

between ions promotes dense packing of the counterions inside of nanopores upon complete ion separation and, hence, maintains the high capacitance.

Taking into account the intrinsically high capacitance observed for carbon single chains in open structures, it is reasonable to assume that combining the high atomic roughness and the curvature of linear carbon chains with a nanoconfinement effect can lead to a further capacitance enhancement. To test this hypothesis, we have conducted simulations of RTILs in contact with model electrodes comprised of an array of single chains, as illustrated in Figure 3. First, we confirmed that the relatively low volumetric density of conductive atoms in this nanoporous electrode structure still provides sufficient screening of electrostatic interactions between intercalated ions. Figure 2a clearly shows a fast (exponential) decrease of the repulsion energy between inserted ions both for the slit and for carbon chain array geometries. Comparing the separation between ions at which the electrostatic repulsion energy is comparable to thermal fluctuations (below $5kT$), it is clear that only 10−20% higher ion separations are required to reach this energy level for the linear chain confinement compared to the slit-pores. Figure 2b shows that the scaling of these separations as a function of nanoconfinement dimensions (width in the slit-pore or separation between single chains) is very similar. Therefore, in single-chain conductive arrays, one can expect sufficient screening of electrostatic interactions between inserted ions needed to retain a relatively high density of the counterions inside of the nanopores even when all co-ions are expelled.

Next we investigate the non-Faradic capacitance enhancement that can be obtained in such nanoporous electrode structures. The IC obtained from simulations of an [EMIM]-[TFSI] RTIL electrolyte on carbon chain arrays with spacing ranging between 6.6 and 8.0 Å is shown in Figure 4 as a

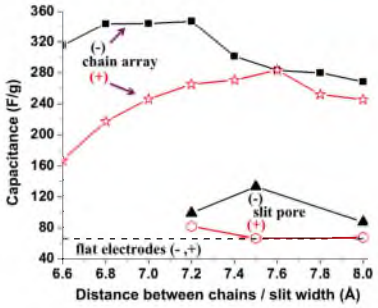

Figure 4. The IC as a function of distance between carbon chains or the width of the slit nanopore for the positive and negative electrodes. The dashed line corresponds to 66 F/g, which is the typical range of ICs on a flat surface.

function of chain separation and is compared to the corresponding values obtained for electrodes with slit-pore geometries. Examination of Figure 4 reveals the following major trends/observations:

(i) The IC values ranging between 240 and 347 F/g obtained for carbon chain arrays are almost a factor of 6 larger than the average IC on a flat surface, clearly indicating a remarkable capacitance enhancement. For comparison, experimental CDC systems generated capacitances of 140−160 F/g in subnanometer pores,[5] while previous simulations of slit-like nanopores reported a 133 F/g maximum in the IC.[9] For our best geometry, the IC per unit mass of electrode in the chain array is about 40% larger than that of an isolated single chain (open structure).

(ii) The IC is asymmetric with respect to the electrode polarity. Specifically, the positive electrode generates systematically lower capacitances than the negative electrode. Similar asymmetry in capacitance enhancement was previously observed for this RTIL electrolyte in slit-like nanopores.[9] This asymmetry is a consequence of details of the chemical structure and the distribution of partial atomic charges in electrolyte ions that, in turn, leads to different interactions between ions and the electrode surface.

(iii) The variation of the IC as a function of the distance between chains is rather broad; however, high values of the capacitance are observed over a broad range (a couple of Å) of chain separations. On the negative electrode, a maximum capacitance of 340−350 F/g is reached between 6.8 and 7.2 Å of chain separation. The relatively broad maxima in the IC indicate a potential flexibility in the design and fabrication of these nanoporous structures with optimal energy storage. In contrast, for slit nanopores, both simulations and experiments showed that only a very narrow range of pore widths (~0.5 Å) generates the capacitance enhancement.

Examination of the ion density inside of electrodes showed that at 0 V for chain arrays with separations > 7.6 Å, the RTIL had no problem wetting the electrodes. However, for arrays with chain separations < 7.5 Å, the ions did not wet the electrode, that is, they did not intercalate inside of the electrode at atmospheric pressure. We observed a similar effect for slit-like nanopores for slit widths < 7.0 Å, and Merlet et al. observed this near-PZC in their simulations of nanoporous CDC electrodes.[35] In these systems, the steric repulsion of ions due to nanoconfinement is larger than attractive dispersion interactions between RTILs and electrode atoms therefore creating "ionophobic" conditions at 0 V. Overcoming this steric repulsion requires either an external pressure or electrostatic potential to be applied on the electrodes. For the latter, Figure 5 shows the density of ions inside of electrodes as a function of chain separation in the electrode at a 3 V potential difference. For electrodes with ionophobic conditions (<7.5 Å), we can see that when the potential is applied, only counterions intercalate inside of the electrode, therefore leading to an almost complete separation of ions. For a wider spacing of chains, more ions intercalate into the electrode, but the electrolyte is no longer completely separated (we see some fraction of co-ion intercalation). Note that the charge built on the electrode is primarily defined by the difference of counterions and co-ions intercalated. From Figure 5, we can see that while the overall number of EMIM and TFSI ions increases with increasing spacing between the chains, the difference between these two (and hence the total charge) stays almost constant. This is consistent with the observed relatively broad and flat peaks in the IC as a function of chain separation discussed in Figure 4.

The mechanisms of charge accumulation (and the capacitance enhancement) on electrodes and the asymmetry of capacitance as a function of electrode polarity can be further studied by examining the DC and ion densities as a function of the electrode potential, as shown in Figure 6 for the system with a 7.2 Å spacing between electrode chains. For the investigated combination of an electrolyte and array of chains, the DC versus electrode potential shows a minimum at low

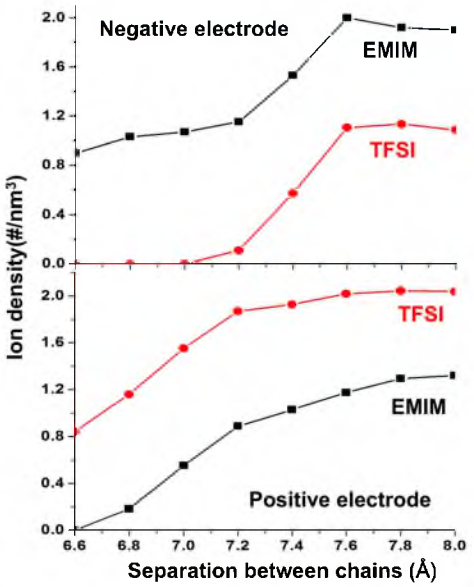

Figure 5. The density of ions for the [EMIM][TFSI] electrolyte inside of carbon chain array electrodes as a function of separation between the chains. Data are shown for the applied potential difference of 3 V.

voltages due to low wettability of the pores by the electrolyte. A maximum at +2 V of 420 F/g and two maxima on the negative electrode at −0.8 (of 375 F/g) and −1.5 V (of 420 F/g) can be clearly identified in Figure 6a. Interestingly, the DC remains surprisingly high (300−350 F/g) even at potentials larger than ±2 V and remains above 250 F/g for an electrode potential in the range of ±4 V. The latter is quite impressive compared to flat electrodes or nanopores with slit-pore geometries where the DC drops quickly as the electrode potential magnitude increases above 2−2.5 V.

Shown in Figure 6b are the densities of inserted ions as a function of the electrode potential. Near PZC, densities of both ions are almost zero, consistent with relatively poor wettability of pores with this separation and with the observed minimum in DC (near PZC) shown in Figure 6a. For this type (i.e., ionophobic) of electrodes, simulations using the primitive model by Kiyohara et al.[36,37] predicted that intercalation of the electrolyte into pores is accompanied by a first-order phase transition at a certain value of the electrode potential, which would compensate for the steric repulsion between the electrolyte and the nanopore. As we can see from Figure 6b in our chemically realistic system for the selected separation of chains, the behavior on positive and negative electrodes is different. On the negative electrode, we observe an almost linear increase of the counterion (EMIM cation) and the total ion densities as the magnitude of the electrode potential increases. There are no sharp jumps in the ion density that can be associated with the phase transition observed by Kioyhara et al. The depletion of the co-ion (TFSI anion) from the negative electrode occurs at a relatively low voltage, that is, the TFSI is essentially completely removed at about −1.8 V. At potentials below −1.8 V, the dominant mechanism for the charge accumulation on the negative electrode is the counterion densification inside of nanopores. However, the changes in the composition/density versus potential on the positive electrode are strikingly different from the negative electrode. As the electrode potential changes sign from negative to positive, a sharp increase of the TFSI density is observed near PZC. Surprisingly, concomitant with the increase of TFSI, the density of EMIM also increases due to strong bonding to TFSI and the inability of the positive electrode to expel the EMIM co-ion. The overall density of ions increases sharply, which is consistent with the first-order phase transition observed by Kiyohara et al. in their simulations using the primitive model. In the potential range between +0.3V and +4.0V the EMIM co-ion density decreases. Interestingly, in this potential range, the total ion density stays almost constant, consistent with the ion swapping mechanism.

Analysis of the total ion density/composition inside of the electrodes shows that the mechanism of charge accumulation can strongly depend on the electrode polarity as well as geometric dimensions of nanopores and the specific interaction between electrolyte ions and the electrode. For the RTIL/single-chain array systems investigated in this work, we observed various mechanisms of ion intercalation/exchange inside of the nanoporous electrodes. These mechanisms included (a) a continuous ion swapping inside of the nanopore

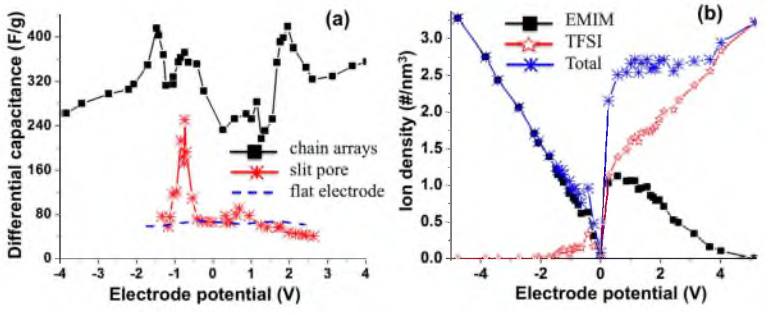

Figure 6. (a) The differential capacitance as a function of the electrode potential for carbon chain array electrodes with a 7.2 Å chain spacing, a slit-like nanopore of width 7.5 Å, and an atomically flat (basal plane graphene) electrode. (b) Densities of ions inside of carbon chain array (7.2 Å chain spacing) electrodes as a function of the electrode potential.

dx.doi.org/10.1021/jz401472c J. Phys. Chem. Lett. 2013, 4, 2829−2837

with increasing electrode potential (the dominant mechanism for wider nanopores that correspond to ionophilic conditions at PZC, i.e., chain separations > 7.5 Å), (b) a continuous increase of the ion density toward superionic states (e.g., as was shown in Figure 6b for the negative ionophobic electrode with a 7.2 Å chain spacing as well as observed by Kondrat et al.[38] in their coarse-grained simulations for slit nanopores), and (c) a change in the electrolyte composition accompanied by clear sharp jumps (phase transitions) in one or both ion densities (this mechanism has been observed in both ionophobic and ionophilic chain array electrodes as well as in our previous studies of slit nanopores). However, despite the variety and specificity of the observed mechanisms for each system, Figure 4 shows that enhanced values of capacitance are obtained for electrodes with ionophobic as well as ionophilic conditions, indicating that the capacitance is primarily sensitive to the extent of ion separation with an applied potential independent of what mechanisms are responsible for this process.

Finally, we would like to point out that the synthesis and stability of linear carbon chains (carbynes) is quite a controversial issue,[39] and fabrication of their arrays is not realistic at the moment. Short (~10 atoms long) chains have been observed in interstellar space, and longer chains were reported in confinement inside of nanotubes;[40,41] however, the presence of linear carbon was observed in highly disordered CDC.[16,34] Moreover, conductivity measurements on those CDC materials have shown 1D hopping for electrical conductance mechanisms,[42] confirming the presence of linear carbon chains in those amorphous materials. The presence of 1D chain elements might explain why low-temperature CDC with a small average pore size and fairly low conductivity shows higher capacitance values compared to materials with 2 orders of magnitude higher conductivity produced or annealed at higher temperatures and containing 2D carbon sheets.[43] Simulations presented here clearly showed that single-chain structural elements can generate several times higher capacitance (per mass) compared to that of a flat graphene surface. Hence, we speculate that despite having overall lower conductivity, the low-temperature CDC might have enough single-chain structural elements that would lead to increased capacitance compared to high-temperature CDC, which is overall more conductive but has "flatter" surface (i.e., lower capacitance) structural elements.

In conclusion, our systematic analysis of correlations between the nanoscale structure of carbon-based electrodes and capacitive energy storage of the EDLC with RTIL electrolytes showed that atomic-scale roughness and curvature of electrode surfaces as well as nanoconfinement of electrolytes can provide noticeable enhancement of the capacitance when the dimensions of these nanostructural characteristics are comparable to electrolyte ion sizes.

Increasing the curvature of the electrode results in an effectively larger volume of the interfacial layer, which allows more counterions per surface area (compared to a flat surface) to compensate for the electrode surface charge, therefore leading to increased capacitance. Open-structure electrodes comprised of single nanotubes or spherical fullerenes showed increasing capacitance with increasing nanoparticle curvature. However, the effect becomes significant only at large curvatures. For example, while a maximum capacitance increase of ~50% compared to a flat basal plane graphene surface was observed for the smallest radius nanotube (R = 1.9 Å), for more realistic nanotubes (R = 3.4 and 6.4 Å), a capacitance increase of only 15−20% was obtained. For spherical particles, the capacitance increase was more pronounced (e.g., for C_{60} fullerenes, R = 3.45 Å, an 80% capacitance increase compared to the flat electrode was observed). However, from practical points of view, increasing the curvature in two dimensions and preserving the conductive properties of electrode nanoparticles might be challenging.

The atomic-scale roughness of the electrode surface can also increase the capacitance. The large local electrostatic fields generated at the atomically rough surface edges facilitate the ion segregation near the surface at lower voltages (less than 2 V), allowing therefore higher capacitance. Just roughening of the flat surface can increase the capacitance by a factor of 2.5 compared to the flat surface if the dimensions of surface roughening patterns are comparable to the electrolyte ions' dimensions.

The nanoconfinement of RTIL electrolytes inside of conductive electrode nanopores leads to significant screening of electrostatic interactions between ions, which can facilitate the separation of co-ions and counterions as well as allow denser packing of counterions inside of nanopores (i.e., super ionic states). As has been shown experimentally and in simulation/theoretical studies, the nanoconfinement can lead to a factor of 2 increase in the capacitance.

In attempt to explore the maximum possible capacitive non-Faradic energy storage, we have investigated the synergistic effect of all three beneficial characteristics by studying the electrodes comprised of conductive single-chain arrays that combine the nanoconfinement effect with maximized atomic roughness and the curvature possessed by a single-chain conductor. The capacitances on the order of 340−350 F/g obtained for the arrays of linear carbon chains are close to a theoretical limit of non-Faradic capacitance that can be achieved using RTIL electrolytes. So far, experimentally, this magnitude of capacitance was only observed when Faradic redox processes were involved, that is, in pseudocapacitors. For example, electrodes comprised of doped polymer chains with single-chain electronic conductivity as large as 80 kS/cm[44] showed similarly large capacitances.[45] However, the charge storage in those electrodes involves fast redox reactions between the electrolyte and polymer chains, which leads to chemical degradation of the electrode after a few thousands cycles. Nanostructured electrode/electrolyte combinations with non-Faradic charge storage, that in principle can have an infinite lifespan due to the absence of chemical reactions, typically report capacitances below 200 F/g. However, very little effort to maximize the interplay of all beneficial nanostructural characteristics discussed above has been made so far. Our simulations clearly demonstrate that significantly higher energy storage is possible for the non-Faradic capacitors if the fabrication and preparation of nanoporous carbon electrodes can be directed to maximize the content of atomically rough and highly curved surfaces. The ideal structural element that contains both of these properties is a carbon single chain. Therefore, optimizing processing conditions to allow the maximum content of carbon single-chain segments, like those believed to be present in low-temperature CDC electrodes, is a promising direction for designing a new generation of nanostructured electrodes.

■ ASSOCIATED CONTENT

Supporting Information

A detailed description of the simulation setup and protocols. This material is available free of charge via the Internet at http://pubs.acs.org.

■ AUTHOR INFORMATION

Notes

The authors declare no competing financial interest.

■ ACKNOWLEDGMENTS

The authors are grateful to the Department of Energy for financial support through the SISGR program under Contract DE-SC0001912 to the University of Utah.

■ REFERENCES

(1) Kornyshev, A. A. Double-Layer in Ionic Liquids: Paradigm Change? *J. Phys. Chem. B* **2007**, *111*, 5545−5557.
(2) Barbieri, O.; Hahn, M.; Herzog, A.; Kötz, R. Capacitance Limits of High Surface Area Activated Carbons for Double Layer Capacitors. *Carbon* **2005**, *43*, 1303−1310.
(3) Simon, P.; Gogotsi, Y. Charge Storage Mechanism in Nanoporous Carbons and Its Consequence for Electrical Double Layer Capacitors. *Philos. Trans. R. Soc. London, Ser. A* **2010**, *368*, 3457−3467.
(4) Kalugin, O. N.; Chaban, V. V.; Loskutov, V. V.; Prezhdo, O. V. Uniform Diffusion of Acetonitrile inside Carbon Nanotubes Favors Supercapacitor Performance. *Nano Lett.* **2008**, *8*, 2126−2130.
(5) Chmiola, J.; Yushin, G.; Gogotsi, Y.; Portet, C.; Simon, P.; Taberna, P. Anomalous Increase in Carbon Capacitance at Pore Sizes Less than 1 Nanometer. *Science* **2006**, *313*, 1760−1763.
(6) Largeot, C.; Portet, C.; Chmiola, J.; Taberna, J. C.; Gogotsi, Y.; Simon, P. Relation Between the Ion Size and Pore Size for an Electric Double-Layer Capacitor. *J. Am. Chem. Soc.* **2008**, *130*, 2730−2731.
(7) Vatamanu, J.; Cao, L.; Borodin, O.; Bedrov, D.; Smith, G. D. On the Influence of Surface Topography on the Electric Double Layer Structure and Differential Capacitance of Graphite/Ionic Liquid Interfaces. *J. Phys. Chem. Lett.* **2011**, *2*, 2267−2272.
(8) Xing, L.; Vatamanu, J.; Smith, G. D.; Bedrov, D. Nanopatterning of Electrode Surfaces as a Potential Route to Improve the Energy Density of Electric Double-Layer Capacitors: Insight from Molecular Simulations. *J. Phys. Chem. Lett.* **2012**, *3*, 1124−1129.
(9) Xing, L.; Vatamanu, J.; Borodin, O.; Bedrov, D. On the Atomic Nature of Capacitance Enhancement Generated by Ionic Liquid Electrolyte Confined in Subnanometer Pores. *J. Phys. Chem. Lett.* **2013**, *4*, 132−140.
(10) Kondrat, S.; Pérez, C. R.; Presser, V.; Gogotsi, Y.; Kornyshev, A. A. Effect of Pore Size and Its Dispersity on the Energy Storage in Nanoporous Supercapacitors. *Energy Environ. Sci* **2012**, *5*, 6476−6479.
(11) Feng, G.; Cummings, P. T. Supercapacitor Capacitance Exhibits Oscillatory Behavior as a Function of Nanopore Size. *J. Phys. Chem. Lett.* **2011**, *2*, 2859−2864.
(12) Wu, P.; Huang, J.; Meunier, V.; Sumpter, B. G.; Qiao, R. Voltage Dependent Charge Storage Modes and Capacity in Subnanometer Pores. *J. Phys. Chem. Lett.* **2012**, *3*, 1732−1737.
(13) Skinner, B.; Chen, T. R.; Loth, M. S.; Shklovskii, B. I. Theory of Volumetric Capacitance of an Electric Double-Layer Supercapacitor. *Phys. Rev. E* **2011**, *83*, 056102.
(14) Kondrat, S.; Kornyshev, A. Superionic State in Double-Layer Capacitors with Nanoporous Electrodes. *J. Phys.: Condens. Matter.* **2011**, *23*, 022201/1−02201/5.
(15) Jiang, D.; Jin, Z.; Wu, J. Oscillation of Capacitance inside Nanopores. *Nano Lett.* **2011**, *11*, 5373−5377.
(16) Palmer, J. C.; Jain, S. K.; Gubbins, K. E.; Cohaut, N.; Fischer, J. E.; Dash, R. K.; Gogotsi, Y. In *Characterization of Porous Solids VIII*, Proceedings of the 8th International Conference on Characterization of Porous Solids; Kaskel, S., Lewellyn, P., Rodriguez-Reinoso, F., Seaton, N.A., Eds.; Royal Society of Chemistry: Cambridge, U.S., 2009; Special Publication No. 318, pp 56−63.
(17) Huang, J.; Sumpter, B. G.; Meunier, V.; Gogotsi, Y. G.; Yushin, G.; Portet, C. Curvature Effects in Carbon Nanomaterials: Exohedral versus Endohedral Supercapacitors. *J. Mater. Res.* **2010**, *25*, 1525−1531.
(18) Palmer, J. C.; Llobet, A.; Yeon, S. H.; Fischer, J. E.; Shi, Y.; Gogotsi, Y.; Gubbins, K. E. Modeling the Structural Evolution of Carbide-Derived Carbons Using Quenched Molecular Dynamics. *Carbon* **2010**, *48*, 1116−1123.
(19) Kondrat, S.; Kornyshev, A. Charging Dynamics and Optimization of Nanoporous Supercapacitors. *J. Phys. Chem. C* **2013**, *117*, 12399−12406.
(20) Vatamanu, J.; Borodin, O.; Bedrov, D.; Smith, G. D. Molecular Dynamics Simulation Study of the Interfacial Structure and Differential Capacitance of Alkylimidazolium Bis(trifluoromethanesulfonyl)-imide [Cnmim][TFSI] Ionic Liquids at Graphite Electrodes. *J. Phys. Chem. C* **2012**, *116*, 7940−7951.
(21) Reed, S. K.; Lanning, O. J.; Madden, P. A. Electrochemical Interface Between an Ionic Liquid and a Model Metallic Electrode. *J. Chem. Phys.* **2007**, *126*, 084704/1−084704/13.
(22) Vatamanu, J.; Borodin, O.; Smith, G. D. Molecular Dynamics Simulations of Atomically Flat and Nanoporous Electrodes with a Molten Salt Electrolyte. *Phys. Chem. Chem. Phys.* **2010**, *12*, 170−182.
(23) Hu, Z.; Vatamanu, J.; Borodin, O.; Bedrov, D. A Molecular Dynamics Simulation Study of the Electric Double Layer and Capacitance of [BMIM][PF_6] and [BMIM][BF_4] Room Temperature Ionic Liquids Near Charged Surfaces. *Phys. Chem. Chem. Phys.* **2013**, *15*, 14234−14247.
(24) Vatamanu, J.; Borodin, O.; Smith, G. D. Molecular Simulations of the Electric Double Layer Structure, Differential Capacitance, and Charging Kinetics for *N*-Methyl-*N*-propylpyrrolidinium Bis-(fluorosulfonyl)imide at Graphite Electrodes. *J. Phys. Chem. B* **2011**, *115*, 3073−3084.
(25) Martyna, G. J.; Tuckerman, M. E.; Tobias, D. J.; Klein, M. L. Explicit Reversible Integrator for Extended System Dynamics. *Mol. Phys.* **1996**, *87*, 1117−1157.
(26) Xing, L.; Vatamanu, J.; Borodin, O.; Smith, G. D.; Bedrov, D. Electrode/Electrolyte Interface in Sulfolane-Based Electrolytes for Li-Ion Batteries: A Molecular Dynamics Simulation Study. *J. Phys. Chem. C* **2012**, *116*, 23871−23881.
(27) Hoover, W. G. Canonical Dynamics: Equilibrium Phase-Space Distributions. *Phys. Rev. A* **1985**, *31*, 1695−1697.
(28) Vatamanu, J.; Borodin, O.; Smith, G. D. Molecular Dynamics Simulation Studies of the Structure of a Mixed Carbonate/$LiPF_6$ Electrolyte near Graphite Surface as a Function of Electrode Potential. *J. Phys. Chem. C* **2012**, *116*, 1114−1121.
(29) Feng, G.; Li, S.; Atchison, J. S.; Presser, V.; Cumming, P. T. Molecular Insights into Carbon Nanotube Supercapacitors: Capacitance Independent of Voltage and Temperature. *J. Phys. Chem. C* **2013**, *117*, 9178−9186.
(30) Feng, G.; Jiang, D.; Cummings, P. T. Curvature Effect on the Capacitance of Electric Double Layers at Ionic Liquid/Onion-Like Carbon Interfaces. *J. Chem. Theory Comput.* **2012**, *8*, 1058−1063.
(31) Lin, R.; Taberna, P.-L.; Fantini, S. B.; Presser, V.; Pérez, C. R.; Malbosc, F. O.; Rupesinghe, N. L.; Teo, K. B. K.; Gogotsi, Y.; Simon, P. Capacitive Energy Storage from −50 to 100 °C Using an Ionic Liquid Electrolyte. *J. Phys. Chem. Lett.* **2011**, *2*, 2396−2401.
(32) Portet, C.; Chmiola, J.; Gogotsi, Y.; Park, S.; Lian, K. Electrochemical Characterizations of Carbon Nanomaterials by the Cavity Microelectrode Technique. *Electrochim. Acta* **2008**, *53*, 7675−7680.
(33) McDonough, J. K.; Frolov, A. I.; Presser, V.; Niu, J.; Miller, C. H.; Ubieto, T.; Fedorov, M. V.; Gogotsi, Y. Influence of the Structure of Carbon Onions on Their Electrochemical Performance in Supercapacitor Electrodes. *Carbon* **2012**, *50*, 3298−3309.
(34) Kravchik, A. E.; Kukushkina, Ju. A.; Sokolov, V. V.; Tereshchenko, G. F. Carbon Structure of Nanoporous Carbon Produced from Boron Carbide. *Carbon* **2006**, *44*, 3263−3268.

(35) Merlet, C.; Rotenberg, B.; Madden, P. A.; Taberna, P.-L.; Simon, P.; Gogotsi, Y.; Salanne, M. On the Molecular Origin of Supercapacitance in Nanoporous Carbon Electrodes. *Nat. Mater.* **2012**, *11*, 306−310.
(36) Kiyohara, K.; Sugino, T.; Asaka, K. Phase Transition in Porous Electrodes. *J. Chem. Phys.* **2011**, *134*, 154710.
(37) Kiyohara, K.; Shioyama, H.; Sugino, T.; Asaka, K. Phase Transition in Porous Electrodes. II. Effect of Asymmetry in the Ion Size. *J. Chem. Phys.* **2012**, *136*, 094701.
(38) Kondrat, S.; Georgi, N.; Fedorov, M. V.; Kornyshev, A. A. A Superionic State in Nano-porous Double-Layer Capacitors: Insights from Monte Carlo Simulations. *Phys. Chem. Chem. Phys.* **2011**, *13*, 11359−11366.
(39) Kudryavtsev, Yu. P.; Heimann, R. B.; Evsyukov, S. E. Carbynes: Advances in the Field of Linear Carbon Chain Compounds. *J. Mat. Sci.* **1996**, *31*, 5557−5571.
(40) Wang, Z.; Ke, X.; Zhu, Z.; Zhang, F.; Ruan, M.; Yang, J. Carbon-Atom Chain Formation in the Core of Nanotubes. *Phys. Rev. B* **2000**, *61*, R2472−R2474.
(41) Zhao, X.; Ando, Y.; Liu, Y.; Jinno, M.; Suzuki, T. Carbon Nanowire Made of a Long Linear Carbon Chain Inserted Inside a Multiwalled Carbon Nanotube. *Phys. Rev. Lett.* **2003**, *90*, 187401.
(42) Vora, P. M.; Gopu, P.; Rosario-Canales, M.; Pérez, C. R.; Gogotsi, Y.; Santiago-Avilés, J. J.; Kikkawa, J. M. Correlating Magnetotransport and Diamagnetism of sp^2-Bonded Carbon Networks through the Metal−Insulator Transition. *Phys. Rev. B* **2011**, *84*, 155114.
(43) Simon, P.; Gogotsi, Y. Capacitive Energy Storage in Nanostructured Carbon−Electrolyte Systems. *Acc. Chem. Res.* **2013**, *46*, 1094−1103.
(44) Heeger, A. J.; Kivelson, S.; Schrieffer, J. R.; Su, W.-P. Solitons in Conducting Polymers. *Rev. Mod. Phys.* **1988**, *60*, 781−850.
(45) Snook, G. A.; Kao, P.; Best, A. S. Conducting-Polymer-Based Supercapacitor Devices and Electrodes. *J. Power Sources* **2011**, *196*, 1−12.

CHAPTER 4

A COMPARATIVE STUDY OF ALKYLIMIDAZOLIUM ROOM TEMPERATURE IONIC LIQUIDS WITH FSI AND TFSI ANIONS NEAR CHARGED ELECTRODES

Reprinted from Publication Electrochimica Acta, 145, Zongzhi Hu, Jenel Vatamanu, Oleg Borodin, Dmitry Bedrov, A comparative study of alkylimidazolium room temperature ionic liquids with FSI and TFSI anions near charged electrodes, 40–52, Copyright (2014), with permission from Elsevier.

Electrochimica Acta 145 (2014) 40–52

Contents lists available at ScienceDirect

Electrochimica Acta

journal homepage: www.elsevier.com/locate/electacta

A comparative study of alkylimidazolium room temperature ionic liquids with FSI and TFSI anions near charged electrodes

Zongzhi Hu [a], Jenel Vatamanu [a,*], Oleg Borodin [b], Dmitry Bedrov [a]

[a] Department of Materials Science & Engineering, University of Utah, 122 South Central Campus Drive, Room 304, Salt Lake City, Utah 84112, United States
[b] Electrochemistry Branch, Sensor & Electron Devices Directorate, U.S. Army Research Laboratory, Adelphi, USA

ARTICLE INFO

Article history:
Received 29 May 2014
Received in revised form 16 August 2014
Accepted 16 August 2014
Available online 4 September 2014

ABSTRACT

Electric double layer (EDL) structure and capacitance generated by the two series of room temperature ionic liquids containing alkylimidazolium $C_n$mim (n = 2,4,6,8) cations and bis(fluorosulfonyl) imide $(FSO_2)_2N^-$ (FSI) or bis(trifluoromethylsulfonyl) imide $(CF_3SO_2)_2N^-$ (TFSI) anions were studied on flat (basal plane graphite) and atomically corrugated (prismatic plane graphite) charged electrode surfaces using atomistic molecular dynamics simulations. On atomically flat surface, generated EDLs in all systems produced a weakly changing differential capacitance (DC) as a function of electrode potential. However, on atomically rough surfaces, ionic liquids with FSI and TFSI anions show substantially different EDL structures and DC dependence. Unlike [$C_n$mim][TFSI], which generated a camel-shape DC regardless of the cation alkyl tail length, the [$C_n$mim][FSI] showed a transition from a bell-shape to a camel-shape DC upon increase of the cation alkyl tail length. Analysis of contributions from rearrangement and reorientation of cations and anions indicated that the ability of the FSI anion to respond to changes in electrode potential is the primary driving force for such behavior.

1. Introduction

Electric double layer (EDL) capacitors are among very promising energy storage technologies [1–6] that can address the constantly increasing energy demands. The energy storage in EDL capacitors is achieved at the electrode-electrolyte interfaces via purely electrostatic (non-Faradic) mechanisms. The absence of electrochemical reactions provides EDL capacitors with several unique advantages such as high delivered power, fast charging/discharging, and long lifetime compared to e.g., batteries. [7–22] One of the promising class of electrolytes in EDL capacitors (or supercapacitors) is room temperature ionic liquids (RTILs) that are comprised of various combinations of molecular ions and that have a melting temperature near or below the room temperate [23–27] good ionic conductivity [28–31] and a large window of thermal [32–35] and electrochemical stability. [36–40] Furthermore, most RTILs have low flammability and volatility [41–49] and are considered environmentally more friendly compared to conventional organic solvents. [50–52] As the energy storage in EDL supercapacitors is achieved at the electrode-electrolyte interface, the understanding of electrolyte structuring near charged surfaces is important in elucidating the charge storage mechanisms and for prediction of possible new routes in materials design to improve the energy density of these devices. The ability of an electrode (or capacitor) to store energy is typically quantified by either differential capacitance (DC) or integral capacitance (IC). Therefore, an increasing number of theoretical and experimental works is dedicated to understanding the correlations between the EDL structure and the magnitude and shape of these capacitances. [53–63]

Our previous simulations have shown that the microstructure of the electrode surface can make a significant impact on the EDL structure and the dependence of DC on electrode potential. [64,65] Similarly, Ho et al. reported for solutions of ions [66] noticeable differences in capacitance when the electrode surface was roughened. Furthermore, several experiments [67–72] showed that electrode surface layers (especially metallic ones) in contact with RTIL electrolytes could restructure generating an inherent atomic scale roughness at the electrode-electrolyte interface. Therefore, a more complete understanding of electrolyte behavior near charged electrodes must be gained by studying the EDL structure at electrode surfaces with different topography. In this work, using atomistic molecular dynamics (MD) simulations we systematically compare the EDL structure and capacitance of two series of RTILs comprised of alkylimidazolium ($C_n$mim, n = 2, 4, 6, 8) cation and either bis-(fluorosulfonyl) imide (FSI) or bis-(trifluoromethanesulfonyl) imide (TFSI) anions on atomically flat (basal plane graphite) and atomically

* Corresponding author: tel: 801-581-8991
E-mail address: jenel.vatamanu@utah.edu (J. Vatamanu).

http://dx.doi.org/10.1016/j.electacta.2014.08.072
0013-4686/

rough (prismatic graphite) surfaces. Scheme 1 illustrates the system set up, the surface topography and the chemical structure of ions in investigated systems.

2. Simulation Setup

The simulations setup consisted of RTIL electrolyte confined between two graphite electrodes that were approximated as conductors. The electrostatic potentials of $+\Psi_0/2$ were imposed on the electrodes, therefore allowing to constrain the total potential difference between electrodes to be $\Delta U = \Psi_0$. Electrode charges were modeled as Gaussian distributed with the widths of 0.5 Å [73,74] and were computed on the fly by minimizing the total electrostatic energy of the system as described in Refs. [73,75]. For more specific details on this methodology and its implementation see e.g., Refs. [76] and [77].

The non-bonded van der Waals interactions were evaluated within a spherical cut-off of 10 Å. The long-range electrostatic interactions were computed using the Smooth Particle Mesh Ewald (SPME) [78,79] method modified for 2D periodic system. [80,81] Simulations were conducted at 393 K and the temperature was controlled using the Nose-Hoover thermostat [82] with a coupling time constant of 0.1ps. The distance between two electrodes was adjusted such that electrolyte density in the middle of the simulation cell was equal to the electrolyte bulk density at 393 K and atmospheric pressure. The latter was computed from the simulations of a bulk RTIL in a 3D-periodic cubic cell using standard NPT ensemble. The equations of motion were integrated with a reversible multiple time step r-RESPA algorithm. [83] Every 0.5fs forces due to bonds and bends were updated. In these simulations the bond lengths were constrained using the SHAKE approach. [84] Every 2.5fs the dihedral and out-of-plane bending forces as well as non-bonded forces within 7.5 Å cut off were updated. Finally, a 5fs time step was used to integrate the non-bonded interactions within the 10 Å cut off and the reciprocal part of SPME summation. The [$C_n$mim][TFSI] electrolyte was modeled with a combined united-atom(UA)/explicit-atom(EA) force field developed in ref. [85]. The force field for [C_2mim][FSI] was developed following a similar procedure as described in refs. [85,86] and using MD simulations with fully atomistic, polarizable APPLE&P force field [87] as a reference. For additional details regarding the force field development, validation and the parameters see references [85,86] and Appendix 1 below.

Using generated simulation trajectories the electrode charges and the spatial distribution of charges in electrolyte were computed. From the profiles of spatial charge distribution $\rho(z)$ across the simulation cell (where z is the direction perpendicular to electrode surfaces), the corresponding Poisson potential $\phi(z)$ was calculated using a numerical integration of the 1D-Poisson equation: $d^2\phi(z)/dz^2 = -\rho(z)/\varepsilon_0$, where ε_0 is the vacuum permittivity. For RTIL electrolytes the Poisson potential usually has large fluctuations near the electrode-electrolyte interface, however, quickly reaches a constant value in the bulk as the EDL formed near the electrode surface screens out the external electrostatic field created by electrodes. The EDL potential drop (U_{EDL}) is calculated as the difference between the Poisson potential at the electrode

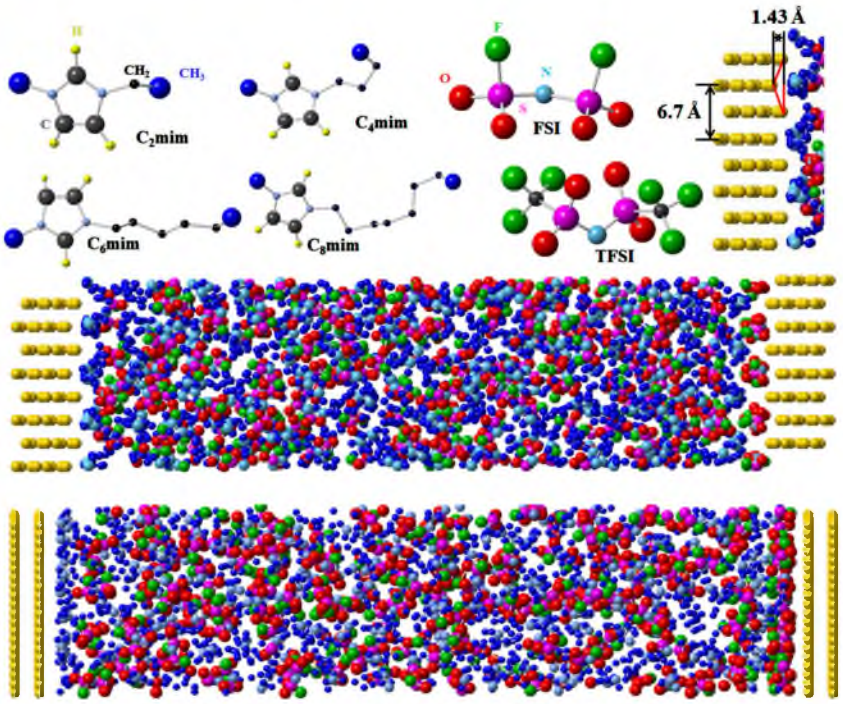

Scheme 1. Chemical structure of the ions comprising the studied ionic liquids and snapshots of the surfaces and simulation cells investigated. CH2 and CH3 groups are represented as united atoms.

surface and the Poisson potential in the bulk electrolyte, $U_{EDL} = \phi_{electrode} - \phi_{bulk}$. The EDL potential for uncharged electrodes is defined as the potential of zero charge (PZC). For any applied surface potential $+\Psi_0$, an electrode potential is defined as the $U_{electrode} = U_{EDL} - PZC$. The differential capacitance (DC) is defined as the variation of the electrode charge (σ) with respect to small changes in the electrode potential $DC = d\sigma/dU_{electrode}$ and was computed as a numerical derivative of the $\sigma = f(U_{electrode})$ obtained from simulations and utilizing the procedure described in refs. [88] (see also the supplementary material of ref. [89] for details).

Another quantity that is often reported in experimental studies of EDL capacitors is the integral capacity (IC) defined as the ratio between the electrode charge and the electrode potential, $IC = \sigma/U_{electrode} = \sigma/(U_{EDL} - PZC)$. The total energy stored by the capacitor can be directly quantified by the capacity of the entire capacitor (IC_{cap}) as follows $E = 0.5 * IC_{cap}(\Delta U)^2$. The IC_{cap} is defined as the ratio between the electrode charge and the potential difference between electrodes, $IC_{cap} = \sigma/\Delta U$. Note that since both electrodes can be considered as individual capacitors connected in series the integral capacitance of the whole cell can be related to the integral capacity of individual plates by the relation: $1/IC_{cap} = 1/IC_+ + 1/IC_-$.

3. Differential capacitance.

Similar to results from our previous simulations of $C_n$mim series with TFSI anion [90] as well as other related RTILs (e.g., [pyr_{13}][TFSI] [91] and [C_4mim][BF_4], and [C_4mim][PF_6] [92]), the DC for [$C_n$mim][FSI] on atomically flat electrode surface shows small variations as illustrated in Fig. 1. The DC stays almost constant as function of electrode potential and the variation in cation tail length (Fig. 1a) does not make any significant effect on the capacitance value or shape. Panel 1b compares the DC of [$C_n$mim][FSI] with that for RTILs with other anions. Variation of anion causes somewhat large differences in the magnitude and shape of DC, but most of them are still in the range between 4–5 $\mu F/cm^2$. This observed range of DC values is in a very good agreement with recent experimental data on [C_4mim][FSI] [93] and in agreement with recent experimental capacitance measurements of similar RTILs near electrodes comprised of a few graphene layers. [94] Recent molecular simulations of related RTILs by Feng et al. [5], Merlet et al. [95], Liu et al. [96] as well as classical density functional theory results [60] also showed similar insensitivity of DC to electrode potential for atomically flat surfaces and similar values for DCs. All these data further support the point that in the practically relevant electrode potential window (i.e., from -3 V to +3 V) on atomically flat (clean) surfaces, common RTILs produce very similar in magnitude and weakly varying DCs. Variations in the ion chemical structures might lead to subtle changes in DC shape in such system, however it would unlikely change substantially the average DC (typical variation are within 20% of the magnitude).

However on atomically rough (prismatic graphite) surfaces we observe a different trend. Fig. 2 compares DCs of [$C_n$mim][FSI] and [$C_n$mim][TFSI] for each cation investigated. Comparison of [$C_n$mim][FSI] data with those shown in Fig. 1 for the flat surface, shows that on the rough electrode surface DC is significantly larger near the PZC and has qualitatively different dependence on the potential from that generated on atomically flat surface. While the maximum DC on the flat surface was ~5 $\mu F/cm^2$, on the rough prismatic graphite it reaches values as large as 8 $\mu F/cm^2$. Also, while the DC on the flat surface was weakly changing versus potential, the DC on the rough surface shows significant variations in the -2 to +2 V voltage window and ranging in magnitude from 4 to 8 $\mu F/cm^2$. If the overall shape of DC on the flat surface for RTILs with n = 2 and n = 4 were weakly camel-shaped and had a clear U-shaped domain near PZC, on the rough surface these RTILs show an overall bell-shape dependence with a very pronounced maximum near PZC (Fig. 2a,b). For RTILs containing cations with longer tails (n = 6 and 8) the trend is reversed: on the flat surface the DC shows one very broad peak (no minimum near PZC), yet on the rough surface we clearly observe a camel-shape dependence with a clear minimum near PZC and two maxima at -0.5 V and +1 V.

As can be seen from Scheme 1, the TFSI anion is larger than FSI as it replaces two F atoms of FSI with two $-CF_3$ groups in its structure. As we discussed above the chemical structure of the anion does not make any significant impact on DC for atomically flat surfaces. On the rough surface, however, the behavior of DC is strongly influenced by the anion chemical structure. Fig. 2 shows that for the entire series of [$C_n$mim][TFSI] with n = 2,4,6,8 only the camel-shape DCs are observed, while for [$C_n$mim][FSI] the DC changes from the bell-shape to a camel-shape as the cation tail length increases. In this regard it is interesting to compare our results with the data reported in ref. [97] from coarse-grained simulations of RTILs comprised of cation with a neutral tail on flat electrode surfaces. In that work a strong dependence of DC on the length of uncharged tail was observed showing a transition from bell-shaped to camel-shaped upon increase of the tail. Our simulations using chemically realistic model show that only corrugated surfaces can lead to such strong variations in DC. For the flat surface we essentially an opposite trend than shown in Fig. 2 of ref [97], however we indeed observe a transition from a

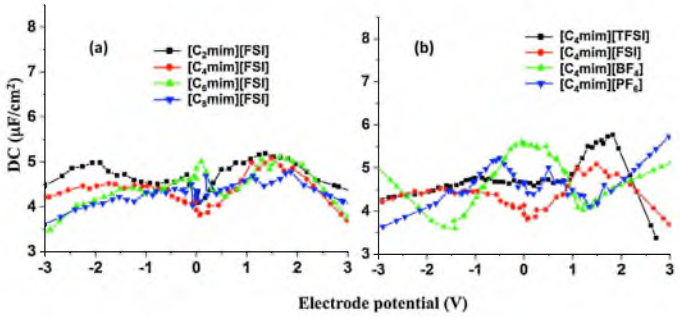

Fig. 1. The differential capacitance of RTIL on the basal plane graphite (atomically flat) electrode surface as a function of electrode potential for (a) [$C_n$mim][FSI] with n = 2,4,6 and 8 and (b) [C_4mim][anion] with anion = FSI, TFSI, BF_4, or PF_6.

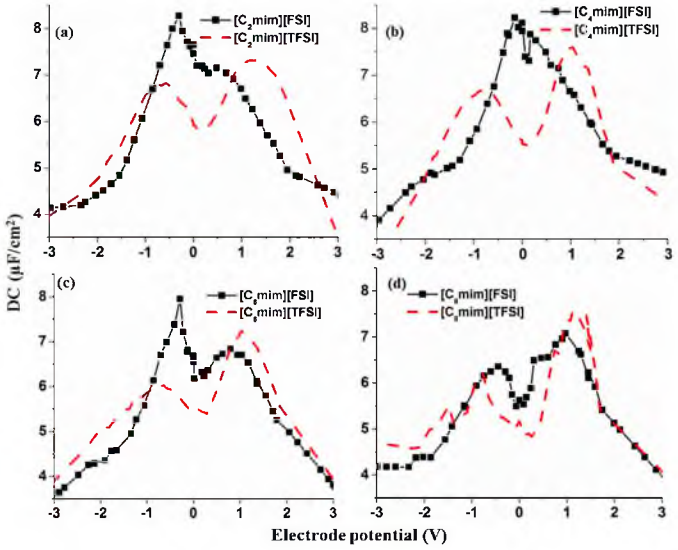

Fig. 2. The differential capacitance of [$C_n$mim][FSI] and [$C_n$mim][TFSI] RTILs on the prismatic plane graphite (atomically rough) electrode surface as a function of electrode potential.

bell-shaped to U-shaped (camel-shaped) DC on the rough surface for FSI anion. So far the [$C_n$mim][FSI] RTILs is the only system which showed this trend with increasing alkyl tail length in our simulations.

4. Integral capacitance

Shown in Fig. 3 is the doubled IC_{cap} as a function of applied potential for [$C_n$mim][FSI] and [$C_n$mim][TFSI] RTILs, for voltages ΔU larger than 0.25 V. Note that for the capacitor where ICs on individual electrodes are roughly symmetric in magnitude, the IC_{cap} should be about a factor of two smaller than the corresponding DCs and ICs of individual electrodes. Therefore, to facilitate the comparison with DC and IC in Fig. 3 we show values of 2^*IC_{cap}. It should be noted that RTILs studied here are electrochemically stable up to potential difference of 4 V, [98] however extending the simulated potential range is useful for understanding of general trends and might be useful for validation of theoretical models in the limit of ion saturation in the EDL. According to Fig. 3 and in agreement with the trends observed for DC, the IC_{cap} on the flat surface is almost constant versus applied potential difference for RTILs with both anions. For any given cation, both anions generate very similar total capacitances. In contrast, on the rough surface we observe a noticeable difference between the 2^*IC_{cap} of [$C_n$mim][FSI] and [$C_n$mim][TFSI] RTILs. For ΔU below 4 V the 2^*IC_{cap} of [$C_n$mim][FSI] is almost 30% (or 1–2.5 μF/cm²) depending on the voltage and the cation tail length) larger than that for [$C_n$mim][TFSI]. At larger voltages, $4V<\Delta U<6.5$ V, where the electrode surface becomes crowded with counterions, the IC_{cap} generated by RTILs with both anions become again comparable (see Figs. 3a,b). For both anions the increase of the alkyl tail length of the cation from n = 2 to n = 8 overall decreases the 2^*IC_{cap} (and hence the ICs of individual electrodes) on average by 1.0 μF/cm². For example, this means that at $\Delta U = 3$ V an energy density loss of the capacitor of ≈2.2 μJ/cm² (or ≈25% in relative value) is expected when the length of the cation alkyl tail is increased from 2 to 8 carbon

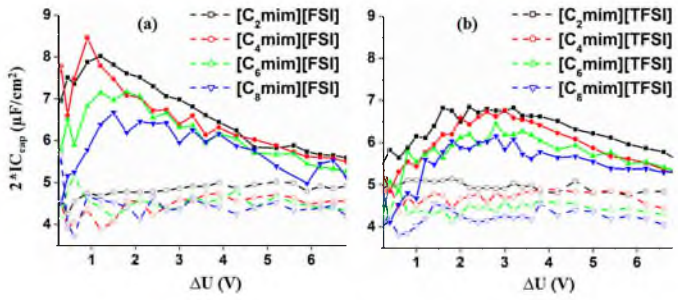

Fig. 3. The integral capacitance (doubled) of the entire capacitor (2^*IC_{cap}) as a function of potential difference between electrodes for (a) [$C_n$mim][FSI] and (b) [$C_n$mim,TFSI] ionic liquids on atomically flat (open symbols) and rough (filled symbols) electrodes.

atoms. Interestingly that for RTILs with TFSI anion the capacitance decrease with increasing of cation tail length is almost independent of the potential difference (Fig. 3b), yet for FSI anion this effect strongly depends on the applied potential difference. At $\Delta U = 1$ V, the 2^*IC_{cap} decreases by about 2.0 $\mu F/cm^2$ upon increasing n from 2 to 8, yet at $\Delta U = 4$ V this difference is less than 0.5 $\mu F/cm^2$.

In many practical applications variation of cation alkyl tail length is used to alter electrochemical, thermophysical or transport properties of RTIL electrolytes to optimize device operation. For example, it is known that increasing the alkyl tail length from n = 1 to n = 6 or 8 in $C_n$mim containing RTILs increases their electrochemical stability or decreases the melting point from as much as 350–400 K (for n = 1 or 2) to about 200 K for n = 6–8. [99,100] On the other hand, the increase of cation alkyl tail length generally leads to higher viscosity of RTILs [100]which is not desirable for capacitors operated at high frequencies. Fig. 3 shows that the increase of alkyl tail length also has a detrimental influence on the energy storage. Based on the data presented in Fig. 3, we have established the following empirical relation: increasing the alkyl tail length of alkylimidazolium cation by one $-CH_2-$ group results in the reduction of IC_{cap} on average by ≈5–6% or 0.0625 $\mu F/cm^2$, and correspondingly, the capacitance of individual electrodes decreases on average by ≈0.125 $\mu F/cm^2$. This reduction in the energy storage must also be considered when an optimal RTIL electrolyte is considered for desired operational conditions. The magnitude of capacities found here are in agreement with general scalling of the capacities proposed in ref. [101].

5. Dependence of the EDL structure on the applied voltage

As the electrode surface are charging the electrolyte near the surface is restructuring leading to the screening out the applied external electric field. It has been previously shown by X-ray reflectivity [102–104] and atomic force microscopy [105,106] experiments as well as by analytical theories [107–110] and atomistic simulations [88–92,111] that RTILs rearrange near charged surfaces in sequences of layers locally rich or depleted in one of the ionic species. Typically, the first layer (the closest to the surface) is overcharged, i.e., it contains more countercharge than the amount of the charge built on the electrode surface, and as the voltage increases the layer can become noticeably denser compared to bulk electrolyte. The second layer is usually rich in co-ions and it slightly overcompensates the excess charge of counterions in the first layer. Several additional layers with decreasing amplitude of charge imbalance can form as well such that the total counter charge over all formed layers will be equal and opposite in sign to the charge accumulated on the electrode. However, some experimental reports, such as the impedance spectroscopy analysis by Baldelli, [112] have suggested that the EDL structure in RTILs is dominated by essentially a single Helmholtz-like layer. In light of these two apparently contradictory interpretations, it is important to closely examine and compare the EDL structuring observed for different RTILs and electrode surfaces from our atomistic simulations.

Fig. 4 shows the ion density profiles calculated based on the location of the ions' center-of-mass as obtained from simulations at uncharged ($U_{electrode} = 0$ V) and charged ($U_{electrode} = \pm 1$ V) surfaces. Figs. 4(a-c) and 4(d-f) compare the ion density profiles of [C_2mim][TFSI] and [C_2mim][FSI] RTILs on the atomically flat electrode surfaces, while panels 4(g-i) show profiles for the atomically rough surface. These figures clearly indicate a formation of the first (innermost) counterion layer within 5 Å from the surface followed by several additional layers at larger separations. The ions centers-of-mass in the first layer are localized within a plane parallel to the surface reaching the maximum local density that is a factor of 7–9 higher compared to the bulk density. The atomically rough surfaces slightly perturbs the distribution of ions next to the surface therefore lowering the maximum local density to ~3–4 and broadening the peaks in the distributions. For all RTILs

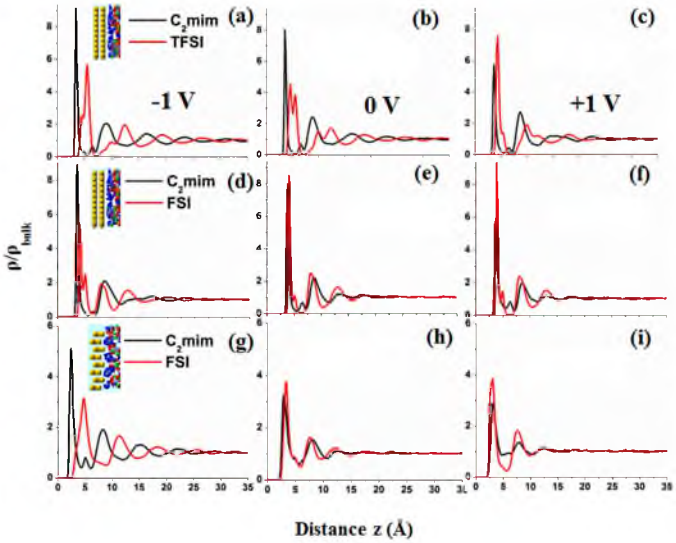

Fig. 4. The normalized ion center-of-mass density profiles as a function of distance from electrode surface at several electrode potentials: -1 V (left column), PZC (central column), and +1V(right column) for [C_2mim][TFSI] on the basal plane graphite (a-c), for [C_2mim][FSI] on the basal plane graphite (d-f), and [C_2mim][FSI] on the prismatic plane graphite (g-i).

studied here we found a multilayer structuring of electrolyte near electrode, even at low electrode potentials. Note that while the center-of-mass peaks show strong oscillations the overall mass density in the EDL looks much smoother. For example, for [C_2mim][FSI] RTIL on the basal plane graphite, the depletion regions between center-of-mass peaks are mostly populated with alkyl tails. Therefore, the observed maxima in the center-of-mass density profiles mostly reflect the alignment of ions into two-dimensional layers, rather than an overall densification of the EDL.

Next we analyze the influence of ion chemical structure on the EDL layered structure. The [C_2mim][TFSI] generates larger amplitudes and shows more layers in the density profiles than the [C_2mim][FSI] RTIL. Indeed, near uncharged flat surface the oscillations in the density profiles for [C_2mim][FSI] basically disappear beyond three layers such that at separations larger than 23 Å from the electrode surface RTIL is essentially unstructured or almost bulk-like (see Fig. 4e for the flat surface and Fig. 4h for the rough surface). In contrast, for the [C_2mim][TFSI] RTIL, the decreasing in amplitude oscillations in the density profiles are observed up to 35 Å from the electrode surface, even near the uncharged flat surface (see Fig. 4b). Interestingly, the anion and cation layers in the [C_2mim][FSI] RTIL have significant overlaps, while in the [C_2mim][TFSI] an alternating ordering of well-separated cation/anion layers is observed. This is related to the disparity in size of investigated anions and the ability of relatively smaller FSI anion to form a layer almost within the boundaries of the cation layer. The TFSI anion, which is noticeably larger in volume than FSI, cannot pack as effectively as FSI and therefore TFSI layers are wider and are well-separated from cation layers. The only condition when we see a clear separation between cation and anion layers in the [C_2mim][FSI] RTIL is on the negatively charged atomically rough surfaces (Fig. 4g). The surface roughness on negative electrodes facilitates the separation between FSI and imidazolium cation in the EDL.

Another aspect of variation of the chemical structure is the influence of the alkyl tail length on the EDL structure. Comparison of density profiles of the ions center-of-mass for [C_2mim][FSI] and [C_8mim][FSI] (not shown) indicate the extent of oscillations (seen in Fig. 4) are similar for those two RTILs and extend up to 30–35 Å from the surface. These longer-range oscillations are in agreement with experimental measurements using atomic force microscopy (AFM) in Ref. [113]. However, in interpretation of the AFM force vs electrode separation data a formation of multiple bilayer structures was proposed for RTILs containing longer alkyl tails. In this regard it is interesting to examine the distribution of N atoms from the cation in the EDL for two RTILs with very different

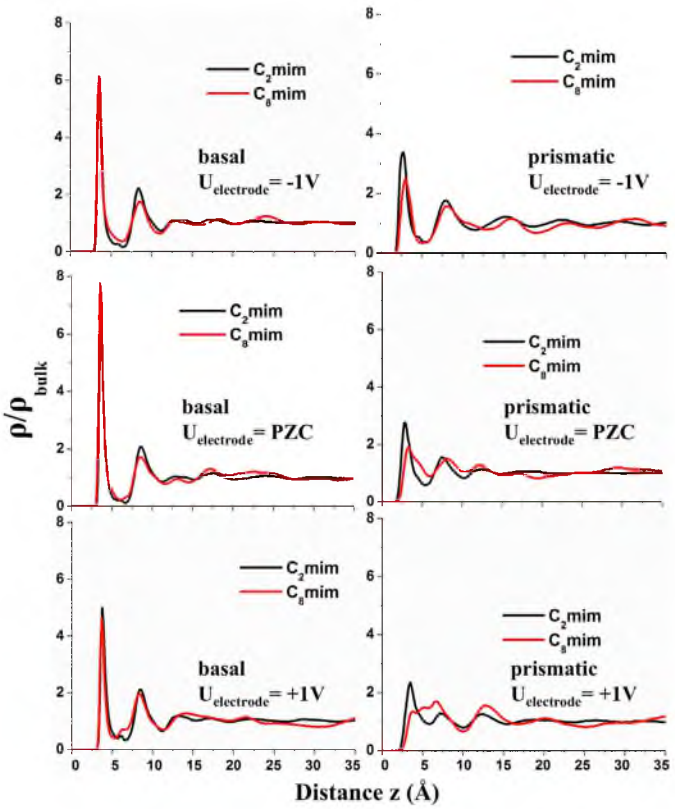

Fig. 5. The normalized density profiles of imidazolium N atoms for [C_2mim][FSI] and [C_8mim][FSI] as a function of distance from electrode surface at electrode potentials -1 V, PZC, and +1 V on the basal plane graphite (left column) and on the prismatic plane graphite (right column).

cations. Fig. 5 compares these profiles at several voltages both for basal and prismatic plane graphite. If a bilayer structure would be present one should expect that the location and the separation between the peaks in these density profiles (i.e., the location of charged imidazolium head groups) would strongly depend on the alkyl tail length. For longer tails a larger separation between e.g., the first and the second peak should be expected. However, as we can see from Fig. 5 on the basal plane graphite the location and the separation between the peaks is independent of alkyl tail length. This is consistent with simulation analysis on related systems reported in Ref. [114] and our previous analysis of [$C_n$mim][TFSI] RTIL. In these systems the spacing between cation "layers" is usually defined by the ability of the anion to "bridge" them, while alkyl tails find the way to fill out the remaining space. At charged surfaces, this usually leads to parallel orientation of alkyl tails to the surface and hence no influence of their length on the ionic layers separation. On the prismatic graphite surface there is somewhat more influence of the alkyl tail length on the distribution of cation head groups, particularly on the positive electrode. However, it does not appear to create any qualitative difference in EDL structure.

In light of structural correlation discussed above it is also instructive to examine the extent of charge overscreening in EDL as a function of voltage. Similar to the analysis in ref. [115], a measure of overscreening can be defined as a ratio between the cumulative counter-charge in the considered electrolyte layer and the charge on the electrode surface. Therefore, we can define the overscreening factor $\gamma(z)$ as a function of distance z from the electrode surface as the ratio between the total electrolyte charge accumulated in the layer between the electrode surface and a certain distance z from the electrode to the total electrode charge,

$$\gamma(z) - \frac{\int_0^z q(Z)dZ}{|\int_0^z q_{electrode}(Z)dZ|}$$

where $|\int_0^z q_{electrode}(Z)dZ|$ is the absolute value of the total electrode charge, q(z) is the space charge density at a given distance z from the electrode, $\int_0^z q(z)dZ|$ is the cumulative charge density at a distance z from electrode. Note that the $\gamma(z)$ is defined only for charged surfaces where the total charge on electrode is not zero. With the above definition the $\gamma(z)$ is -1 or +1 at the negative or positive electrodes, respectively. Values of $\gamma(z)$ larger than 1 in absolute value indicate spatial regions where the total cumulative electrolyte charge exceeds (i.e., overscreens) the charge on the electrode. For the flat conductive electrodes most of the electrode charge is distributed in the surface layer adjacent to electrolyte, and therefore the $\gamma(z)$ is straightforward to understand.

Fig. 6 illustrates the extent of overscreening as a function of separation from the electrode surface as obtained from our simulations of [C_2mim][FSI] on atomically flat electrode surfaces. As shown in Fig. 6, at small voltages (i.e. bellow 0.6 V) the total cumulative charge in electrolyte layers can significantly (almost an order of magnitude) exceed the charge on the electrode, which is in agreement with Bazant's et al. [115] prediction from a mean field theory approach. Interestingly, at lower voltages such overscreening is observed not only for the first layer but also for the layers further removed from the electrode surface. Moreover, even within one layer, e.g. the innermost layer of ions within 5 Å from the surface, the $\gamma(z)$ can even change the sign. Such large overscreening on weakly charged electrodes is consistent with the fact that even uncharged surfaces can generate some charge separation of electrolyte at the interface and small voltages applied on electrode will not interfere much with the relatively large (compared to the electrode charge accumulated at small voltages $\Delta U < 0.6$ V) local charges in the interfacial layer(s) inherited from the intrinsic electrolyte structure at uncharged surfaces. The latter is generated by the differences in the ions' shape, conformations, and their short-range non-bonded interactions with the surface. The extent of overscreening in the interfacial layer also depends on the electrode polarity and voltage magnitude.

The trends in overscreening profiles can be rationalized by examining the charge density profiles shown in Fig. 7. While at uncharged surface there are more cations in the first ionic layer (within 5 Å), the FSI anions present in this layer are oriented such that the negatively charged O and F atoms are much closer to the surface than the atoms caring most of the positive charge of the cation. As can be seen from Figs. 6a,b and 7, at very closed approaches the $\gamma(z)$ drops sharply to negative values and then after reaching a minimum rises to the positive $\gamma(z)$ at the innermost layer boundary. The presence of the negatively charged O and F atoms on the surface shown in Fig. 7b,c explains the negative PZC for these RTILs on graphite surfaces. When slightly negative potentials are applied to the electrode there is still an excess of negative groups next to the surface, as shown in Fig. 6a, and voltages as high as -1 V are needed to push the O and F atoms completely away from the surface and to eliminate the region of negative $\gamma(z)$ near the surface. At the positive electrode, the negative counter-charge continues to accumulate next to the electrode surface and, hence, the region of negative $\gamma(z)$ is preserved at all potentials as expected. However, the extent of overscreening is decreasing due to increasing dominance of electrostatic interactions between the electrode and the counter-ions and relative reduction of contributions from the effects that led to the intrinsic ion partitioning near the uncharged surface. Nevertheless, on the positive electrode, the first layer charge

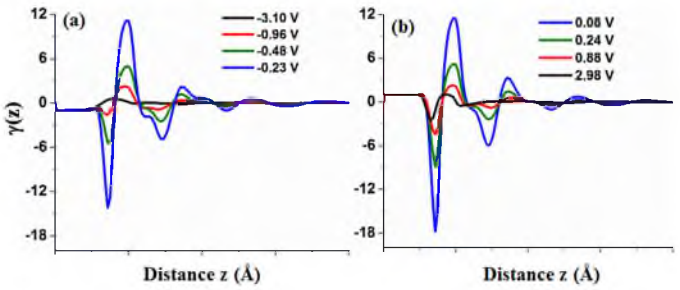

Fig. 6. The dependence of $\gamma(z)$ on the distance from electrode surface for several potentials on the negative (a) and positive (b) electrodes for [C_2mim][FSI].

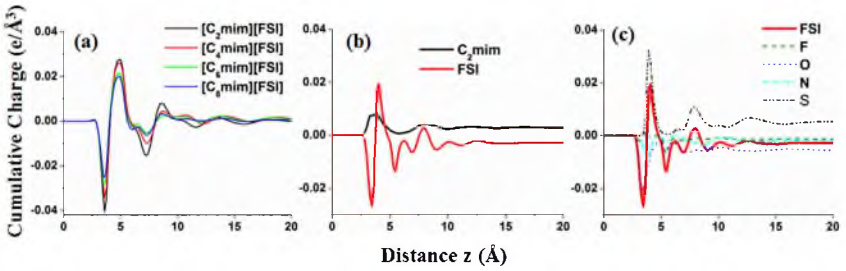

Fig. 7. (a) The cumulative space charge profile as a function of distance from electrode for the [$C_n$mim][FSI] series on flat surface. (b) Contributions to the spatial charge profile from individual ions for [C_2mim][FSI]. (c) Contributions to the spatial charge profile generated by FSI from its atoms different atom types (F, S, O, N). All profiles were obtained at the PZC and calculated using atom-based charge distributions.

exceeds the electrode charge by as much as 140% even at electrode potentials as large as +3.5 V for the entire series [C_{2-8}mim][FSI]. The observation that some electrode/counterion combinations could require voltages larger than those corresponding to electrolyte electrochemical stability in order to transition from overscreening to overcrowding regime is in agreement with our previous simulations [91].

The increase of cation alkyl tail decreases the density of the negative charge near the surface (see Fig. 7a) because alkyl tails have an effective affinity for uncharged graphite surface [85] and therefore they compete with the negatively charged O and F atoms of FSI on the surface. However, qualitatively the behavior of RTILs with longer alkyl tail cations is similar to that shown in Fig. 6 and 7b,c for the [C_2mim][FSI].

Finally, Figs. 6 and 7 clearly illustrate the importance of details of the chemical structure and partial charge distribution of the ions. Often coarse-grained models that collapse several atoms into a single force center caring a combined charge are used to represent RTIL electrolytes. While these models can capture the bulk structure of RTIL very well, it will be hard to expect from them to capture correct the structure, overscreening profiles, and capacitance of the EDL near charge surfaces. For example, if instead of considering atomic charge distribution in calculation of overscreening profiles in Fig. 6 we would coarse-grained our representation and associated the whole charge with the ion center-of-mass, the overscreening profiles would show qualitatively different (inaccurate) dependence.

6. Correlation of DC with EDL structure

Finally, we attempt to correlate the observed dependence of DC on voltage with the changes in the EDL structure. In our previous work [65] we explained why RTILs on strongly corrugated surfaces can generate a larger and qualitatively different DC compared to that on atomically flat surfaces. We remind here that from a microscopic point of view the differences in capacitance between flat and rough surfaces could be understood as originating from the large gradients in local electrostatic fields generated near the rough edges and the steric effects interfering with ion packing on the surface when the dimensions of surface roughness patterns/features are comparable to ion sizes. [65] These strong local fields influence the rates (vs. voltage) at which the ion adsorption/desorption occurs and, therefore, qualitatively change the dependence of DC.

Here we focus on examinination of DC for [$C_n$mim][FSI] RTILs on corrugated surface. It is interesting to understand the impact of the multi-layer structure of EDL and its correlation with the DC dependence. For this purpose we have computed derivatives (with respect to applied potential) of the charge accumulated in the interfacial layers of various thickness d and compared them with the charge accumulation on the electrodes, i.e., the DC. For convenience of comparison with DC, the derivative of electrolyte cumulative charges in the layers were multiplied by -1 and converted into μF/cm^2 units. For all systems studied here we found that the changes in the total charge accumulated in the first layer from the surface (which encompasses the first peak in the ion density profiles and extends to ~5 Å from the surface) are in qualitative agreement with the obtained DC. Indeed, as shown in Fig. 8a–c for [C_2mim][FSI], [C_2mim][TFSI] and [C_8mim][FSI], the variation in the interfacial layer charge density has the same qualitative shape as the total DC, however, the magnitudes are noticeably off from the true DC. For example, in the [C_8mim][FSI] the maximum rate (vs. potential) of the first layer charge accumulation is ~10.2 μF/cm^2 while the maximum in the DC is 6.2 μF/cm^2, indicating that quantitatively the contributions of additional layers to the total charge variation on the electrode is significant. Nevertheless, for all RTILs investigated here we can conclude that consideration of charge accumulation in the interfacial layer of thickness d = 10–12 Å is sufficient to *quantitatively* capture the generated DC. Therefore in these systems the charge storage occurs in about 1 nm interfacial layer of electrolyte while the remaining electrolyte further away from the surface is basically just bulk electrolyte. This observation may be consistent with impedance spectroscopy experiments probing (for certain electrolytes) an electrode-electrolyte interface consisting of a thick (less than 1 nm) layer near surface. [112]

We also examine the contributions from anion and cation to the total charge accumulation in the EDL as shown in Fig. 8d–f for the interfacial region of width d = 10 Å. If a small change in electrode potential causes large changes in the interfacial layer charge due to reorientation or redistribution of cation or anion then the corresponding contribution to DC will be high. For example for [C_2mim][FSI] near PZC both cation and anion show relatively high values of contributions to the interfacial charge derivative (~4 μF/cm^2 Fig. 8d). For FSI anion this value is close to its maximum that is basically preserved over a wide range of positive potentials. This indicates that in this system the FSI anion can easily rearrange its distribution near positively charged surface. On the negative electrode, the FSI contribution drops by about factor of two, but still continues to contribute even at highly negative surfaces, e.g. at -3 V the FSI contribution is about 2 μF/cm^2. For C_2mim cation the effect has an opposite trend. With increasing the magnitude of the negative potential the cation contribution to charge accumulation increases up to -0.5 V potential and then smoothly reduces such that at -3 V both cation and anion have similar contributions to DC. On the positive electrode, the cation contribution smoothly goes to zero

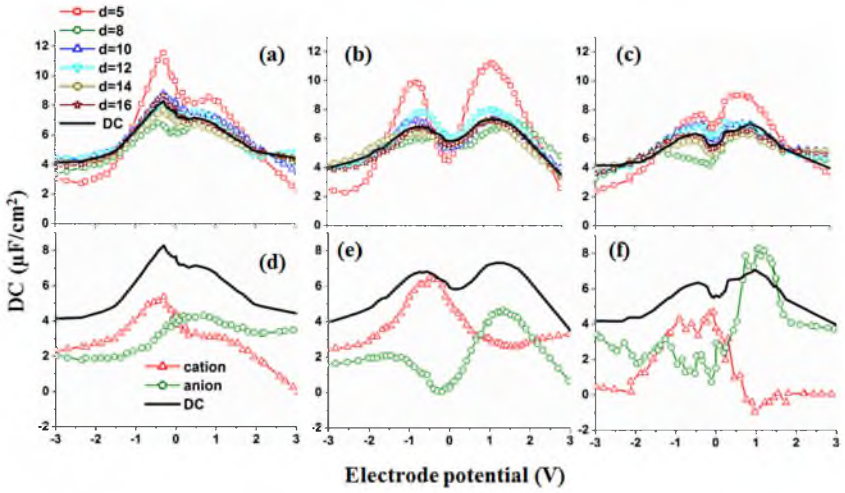

Fig. 8. The differential capacitances and derivatives of the cumulative charge density (converted in μF/cm^2 and multiplied by -1 for convenience of comparison) of electrolyte located within an interfacial region of thickness d for (a) [C_2mim][FSI], (b) [C_2mim][TFSI] and (c) [C_8mim][FSI] near prismatic plane graphite. Panels d-f show anion and cation contributions to the derivatives of the total charge within the interfacial layer d = 1.0 nm.

indicating that redistribution or increased packing of FSI anions remain the only contributor to DC at high positive voltages. Fig. 8d clearly shows that near PZC the contributions from both ions are close to their maximum and, therefore, results in the overall bell-shape DC dependence for this system.

Figs. 8e,f show that for [C_2mim][TFSI] and [C_8mim][FSI] RTILs on the same prismatic plane graphite surface the charge accumulation rates vs electrode potential are different. Here the maximum contributions from each ion type are well separated from PZC in opposite directions. For example, while the maximum from cation contribution remained approximately at the same voltage, the maximum rate for anion shifted to the +1.0–1.5 V range. At PZC, the anion is basically insensitive to electrode potential changes and hence does not contribute to DC. Only at higher positive potentials the anion contribution becomes dominant. This shift of anion contribution to higher positive voltages is the primary reason for the observed camel-shape DC in these systems. This qualitative change in DC shape with increasing tail length for the [$C_n$mim][FSI] RTILs is likely associated with strong tendency of these tails to adsorb on the prismatic graphite surface and maximize their van der Waals interactions. This, in turn, interferes with the ability of FSI anion to rearrange near the surface at relatively small values of positive potentials. Clearly this effect depends on a very delicate balance of all competing interactions, i.e., details of charge distribution on the electrode surface, the specifics of electrostatic and van der Waals interactions between the ions and with the surface, steric interference of surface structure with ion packing, etc. As we can see from, the same series of RTILs with FSI anion but on a basal plane graphite does not show a transition from a bell-shape to a camel-shape or if the TFSI anion is used instead then only the camel-shape dependence of DC independent of alkyl tail length is observed.

7. Conclusions

A systematic molecular dynamics simulation study of differential capacitance and the electric double layer structure formed near atomically flat and corrugated surfaces for [$C_n$mim][FSI] and [$C_n$mim][TFSI] (n = 2,4,6,8) showed that the influence of the alkyl tail length depends on the topography of electrode surface and anion type. On atomically flat electrode (basal plane graphite) surfaces our simulation showed that RTIL electrolytes order into several layer structure that extends over 1.5 to 3 nm distance from the electrode surface depending on the voltage and ionic liquid. For these surfaces a weak dependence of DC on voltage, cation tail lengths and anion type is observed for all RTILs compared. This general trend is in agreement with phenomenological EDL models.[116,117]

However, the DCs of the same electrolytes on atomically rough surface (represented here by the prismatic plane graphite) show very different trends and substantial dependence on the ions chemical structure. The variations in DC between minima and maxima become on the order of 2–3 μF/cm^2 (within the -2 V - +2 V electrode potential window) which is about factor 3-4 large than those observed for the same electrolytes on flat surfaces. In addition to increased variations on potential the capacitances on the atomically rough surfaces are systematically higher than on the flat ones. While on flat surfaces the change of anion from FSI to TFSI did not qualitatively changed the dependence of DC on voltage, on the rough surfaces the DC generated by RTILs containing FSI anion showed a transition from a bell-shaped DC for RTILs with the n = 2,4 cation tail lengths to a camel-shaped DC for cations with longer alkyl tails. Such behavior is atributed to the ability of the FSI anions to rearrange in the EDL layer upon changes in electrode potential. Despite of the multilayer structure, the DC dependence on voltage can be qualitatively understood from the changes in the cumulative charge in the electrolyte interfacial layer(s). We demonstrate that details of the ion orientation is important for understanding the electrode charge accumulation and over-screening particularly at low voltages where intrinsic partitioning of cations or anions to the specific surface can facilitate the charge separation in the interfacial layer.

Acknowledgements.

This research was sponsored by the Army Research Laboratory under Cooperative Agreement Number W911NF-12-2-0023. The

views and conclusions contained in this document are those of the authors and should not be interpreted as representing the official policies, either expressed or implied, of the Army Research Laboratory or the U.S. Government. The U.S. Government is authorized to reproduce and distribute reprints for Government purposes notwithstanding any copyright notation herein.

Appendix 1. : Development of Nonpolarizable United Atom/ Explicit Atom Force Field for [$C_n$mim][FSI]

In order to cut the computational cost a nonpolarizable combined united atom (UA)/explicit atom (EA) force field for [$C_n$mim][FSI] has been developed and validated using the APPLE&P [87] (Atomistic Polarizable Potential for Liquids, Electrolytes and Polymers) as a reference point. The previously developed [90] parameters for $C_n$mim were transferred without modifications, while parmaters for the FSI were modifed using the TFSI parameters as discussed below. The partial charges for FSI were fit to describe the electrostatic potential on a grid of points around it as well as the molecular gas phase dipole moment from quantum chemistry (QC) calculations at MP2/cc-pvTz level following our previous work [87] but with polarizabilities set to zero. The FSI bond lengths and bend angles were taken from the APPLE&P [87] without modification. The F-S bond (FSI) was 1.605 Å and the O-S bond (FSI) was 1.44 Å. The lengths of the other bonds were from our previous ref. [90]. The dihedral angle parameters were determined by fitting the gas phase conformational energy surface of model molecules as determined from QC calculations as previously described for the APPLE&P. [87] The dihedral energy between F-N-S-N atoms of FSI was: $E_{dihedral}$ (θ) [kJ/mol]= −1.7280cos(θ)+6.8157cos(2θ)+1.6297cos(3θ). The N atoms of the FSI had an attached dummy atom at a distance of 0.65 Å along the S-N-S bisector with a zero mass and no van-der-Waals interactions. The charge on the dummy atom was +0.197e. The S-S repulsion-dispersion interactions were adjusted to improve the ion self-diffusion coefficients of [pyr_{13}][TFSI], [pyr_{14},TFSI] and [N_{4111}][TFSI] as a function of temperature. The C-C repulsion-dispersion parameters were adjusted to obtain correct ion packing probed through iso-surfaces of TFSI and FSI oxygen atom densities, density of [C_2mim][TFSI] and [C_2mim][FSI] as well as transport properties obtained from fully atomistic simulations with the APPLE&P force field. The other force-field parameters utilized in this work and not previously reported in refs. [85] and [86] are given in Tables A1-2 .

To validate the developed nonpolarizable UA/EA force field extensive simulations of bulk [C_2mim][FSI] RTILs were conducted using the new force field and the fully atomistic, polarizable APPLE&P force fields. A cubic simulation cell with periodic boundary conditions contained 150 ionic pairs of [C_2mim][FSI]. The RTIL initial configurations were created in the gas phase corresponding in a cell with linear dimensions of approximately ~100 Å. The dimensions of the simulation cells were then reduced to yield estimated densities at 393 K and followed by 1 ns equilibration run in the NPT ensemble. The Ewald summation method was used for electrostatic interactions between charge-charge and charge-induced dipole interactions (for the APPLE&P simulations) using 8^3 k-vectors. The induced dipole-induce dipole interactions were calculated within the cutoff radius of 11 Å. A multiple timestep

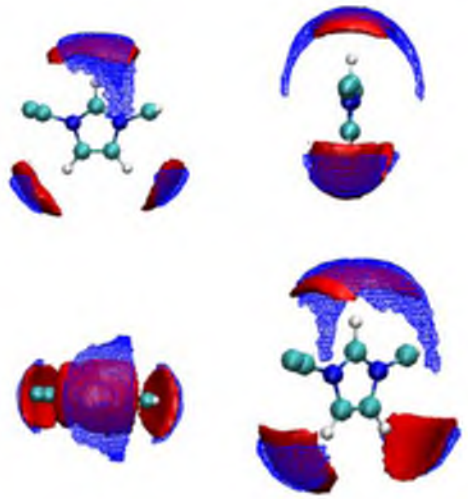

Fig. A1. The iso-surface $\rho/\rho_{bulk}=5$ of the oxygen of FSI anion 3-D probability distribution function in [$C_n$mim][FSI] as obtained from MD simulations using the UA/EA force field used in this work (solid red iso-surface) and the fully atomistic APPLE&P force field (f1e24Lp) at 298 K.

Table A1a
The electrostatic charges and the van der Waals parameters for FSI atoms. The van der Waals self-energy is: $E_{vdw\sim nonbonded} = Aexp(-B*r)-C/r^6+D/r^{12}$

Atom	Charge (e)	A [kJ/mol]	B ($Å^{-1}$)	C (kJ/mol/$Å^6$)	D(kJ/mol/$Å^{12}$)
F	−0.221	29781.294	3.417	630.612	735.168
S	0.865	36074.029	2.500	8015.163	31293.672
N	0.622	30643.616	2.790	2380.361	8359.471
O	−0.466	66622.250	3.644	1000.268	339.576

Table A1b
The force-field parameters for the intramolecular bend energy, $E_{angle} = 1/2\, K_\theta\, [(\theta - \theta_0)\pi/180]^2$

angles	K_θ (kJ/mol/rad)	θ_0 (deg)
F S-N-	903.744	102.200
F S-O=	1075.288	103.900
O=S-N-	870.272	112.600
O=S-O=	799.144	119.300
S-N-S-	732.200	125.200

Table A2
Thermodynamic and transport properties of the [C_2mim][FSI] from MD simulations employing combined nonpolarizable UA/EA (in bold) and fully atomistic the APPLE&P (regular font) force fields. The following properties are shown in table: density ρ, heat of vaporization H_{vap}, ion self-diffusion coefficients D, finite simulation box size correction to ion self-diffusion coefficient ΔD_{FSC} and ion conductivity λ)

T (K)	force field t	sim. length (ns)	ρ (kg/m^3)	H_{vap} (kJ/mol)	D_+ (10^{-10} m^2/s)	D (10^{-10} m^2/s)	ΔD_{FSC} (10^{-10} m^2/s)	λ (mS/cm)
393	**UA/EA**	**12**	**1332**		**5.23**	**4.55**	**0.88**	**94.3**
393	APPLE&P	16	1347		4.39	3.88	0.65	76.2
333	**UA/EA**	**18.5**	**1387**		**1.88**	**1.56**	**0.32**	**40.2**
333	APPLE&P	16.8	1395		1.72	1.53	0.29	36.6
298	**UA/EA**	**18**	**1421**	**143.4**	**0.94**	**0.73**	**0.14**	**22.1**
298	APPLE&P	18	1426	134.6	0.70	0.62	0.13	17.0

integration with an inner timestep of 0.5 fs (bonded interactions), a middle time step of 1.5 fs for all nonbonded interactions within a truncation of 7.0 Å and an outer timestep of 3.0 fs for all nonbonded interactions between 7.0 Å and 11 Å as well as for the reciprocal part of the Ewald summation was employed. The Nose-Hoover thermostat and barostat were used to control temperature and pressure with the corresponding frequencies of 10^{2} and 0.5×10^{3} fs. Induced dipoles were calculated via a direct iteration scheme with a predictor method. Brownian dynamics simulations of ion pairs were performed at 298 K for 2-4 ns to yield the gas phase ion pair energies.

Simulations using the developed UA/EA force field predicted the [C_2mim][FSI] density, ion self-diffusion coefficients, and conductivity in a good agreement with the fully atomistic many-body polarizable APPLE&P force field as shown in Table A2. A comparison of the iso-surface of the probability of finding oxygen atom of FSI anion around C_2mim cation is shown for UA/EA and APPLE&P in Fig. A1. The UA/EA nonpolarizable force field yields more localized positions of FSI anion above the C_2 hydrogen than the APPLE&P force field with a lesser probability of finding the FSI anion directly above and below the imidazolium ring. In general, we consider the ion packing to be similar in simulations with UA/EA and APPLE&P force fields. We conclude that the developed nonpolarizable UA/EA force field adequately predicts ionic liquid density, heat of vaporization, structure and dynamics, yet computationally much less expensive than the many-body polarizable APPLE&P force field.

References

[1] G. Wang, L. Zhang, J. Zhang, A review of electrode materials for electrochemical supercapacitors, J. Chem Soc Rev 41 (2012) 797.
[2] P. Simon, Y. Gogotsi, Materials for electrochemical capacitors, Nature Materials 7 (2008) 845.
[3] F. Béguin, V. Presser, A. Balducci, E. Frackowiak, Carbons and electrolytes for advanced supercapacitors, Advanced Materials 26 (2014) 2219.
[4] J.R. Miller, Valuing reversible energy storage, Science 335 (2012) 1312.
[5] G. Feng, S. Li, V. Presser, P.T. Cummings, Molecular insights into carbon supercapacitors based on room-temperature ionic liquids, J. Phys. Chem. Lett. 4 (2013) 3367–3376.
[6] Y. Simon, B. Gogotsi, B. Dunn, Where do batteries end and supercapacitors begin? Science 343 (2014) 1210–1211.
[7] K. Naoi, W. Naoi, S. Aoyagi, J.-I. Miyamoto, T. Kamino, New generation "nanohybrid supercapacitor", Accounts of Chemical Research 46 (2013) 1075–1083.
[8] M. Yeager, W. Du, R. Si, D. Su, N. Marinkovic, X. Teng, Highly efficient K $0.15MnO_2$ birnessite nanosheets for stable pseudocapacitive cathodes, Journal of Physical Chemistry C 116 (2012) 20173–20181.
[9] H.S. Choi, J.H. Im, T. Kim, J.H. Park, C.R. Park, Advanced energy storage device: A hybrid BatCap system consisting of battery-supercapacitor hybrid electrodes based on $Li_4Ti_5O_{12}$-activated-carbon hybrid nanotubes, Journal of Materials Chemistry 22 (2012) 16986–16993.
[10] P.M. Biesheuvel, M.Z. Bazant, Nonlinear dynamics of capacitive charging and desalination by porous electrodes, Physical Review E - Statistical, Nonlinear, and Soft Matter Physics 81 (31) (2010) 502.
[11] H. Guan, L.Z. Fan, H. Zhang, X. Qu, Polyaniline nanofibers obtained by interfacial polymerization for high-rate supercapacitors, Electrochimica Acta 56 (2010) 964–968.
[12] C. Peng, S. Zhang, D. Jewell, G.Z. Chen, Carbon nanotube and conducting polymer composites for super capacitors, Progress in Natural Science 18 (2008) 777–788.
[13] C.M. Ionica-Bousquet, W.J. Casteel Jr., R.M. Pearlstein, G. GirishKumar, G.P. Pez, P. Gomez-Romero, M.R. Palacín, D. Munoz-Rojas, Polyfluorinated boron cluster – $[B_{12}F_{11}H]_2$ – based electrolytes for supercapacitors: Overcharge protection, Electrochemistry Communications 12 (2010) 636–639.
[14] J. Li, H. Xie, Y. Li, J. Liu, Z. Li, Electrochemical properties of graphene nanosheets/polyaniline nanofibers composites as electrode for super capacitors, Journal of Power Sources 196 (2011) 10775–10778.
[15] J. Mu, B. Chen, Z. Guo, M. Zhang, Z. Zhang, P. Zhang, C. Shao, Y. Liu, High voltage supercapacitors using hydrated graphene film in a neutral aqueous electrolyte, Nanoscale 3 (2011) 5034–5040.
[16] X. Yang, Y.S. He, G. Jiang, X.Z. Liao, Z.F. Ma, High voltage supercapacitors using hydrated graphene film in a neutral aqueous electrolyte, Electrochemistry Communications 13 (2011) 1166–1169.
[17] A. Safavi, S.H. Kazemi, H. Kazemi, Electrochemically deposited hybrid nickel-cobalt hexacyanoferrate nanostructures for electrochemical supercapacitors, Electrochimica Acta 56 (2011) 9191–9196.
[18] M. Aghazadeh, S. Dalvand, Large-scale and facile electrochemical preparation of β-$Co(OH)_2$ nanocapsules and investigation of their supercapacitive performance, Large-CScale and Facile Journal of the Electrochemical Society 161 (2014) D18–D25.
[19] M.E. Plonska-Brzezinska, L. Echegoyen, Carbon nano-onions for supercapacitor electrodes: Recent developments and applications, Journal of Materials Chemistry A 1 (2013) 13703–13714.
[20] C. Mondal, M. Ganguly, P.K. Manna, S.M. Yusuf, T. Pal, Fabrication of porous β-$Co(OH)_2$ architecture at room temperature: A high performance supercapacitor, Langmuir 29 (2013) 9179–9187.
[21] E. Coadou, L. Timperman, J. Jacquemin, H. Galiano, C. Hardacre, M. Anouti, Comparative study on performances of trimethyl-sulfonium and trimethyl-ammonium based ionic liquids in molecular solvents as electrolyte for electrochemical double layer capacitors, Journal of Physical Chemistry C 117 (2013) 10315–10325.
[22] G.P. Pandey, S.A. Hashmi, Ionic liquid 1-ethyl-3-methylimidazolium tetracyanoborate-based gel polymer electrolyte for electrochemical capacitors, Journal of Materials Chemistry A 1 (2013) 3372–3378.
[23] S. Bajus, A. Deyko, A. Bosmann, F. Maier, H.P. Steinruck, P. Wasserscheid, Low melting Li/K/Cs acetate salt mixtures as new ionic media for catalytic applications-first physico-chemical characterization, Dalton Transactions 41 (2012) 14433–14438.
[24] B. Liebmann, A. Friedl, J.F.C. Rodrigues, Lignocellulosic biomass dissolution and fractioning using ionic liquids as a solvent, Chemical Engineering Transactions 29 (2012) 553–558.
[25] A.B. Menhaj, B.D. Smith, J. Liu, Exploring the thermal stability of DNA-linked gold nanoparticles in ionic liquids and molecular solvents, Chemical Science 3 (2012) 3216–3220.
[26] K. Tsunashima, M. Fukushima, M. Matsumiya, Physicochemical properties of trialkylphosphonium-based protic ionic liquids, Electrochemistry 80 (2012) 904–906.
[27] F. Gharagheizi, P. Ilani-Kashkouli, A.H. Mohammadi, Computation of normal melting temperature of ionic liquids using a group contribution method, Fluid Phase Equilibria 329 (2012) 1–7.
[28] N. Shirshova, A. Bismarck, S. Carreyette, Q.P.V. Fontana, E.S. Greenhalgh, P. Jacobsson, P. Johansson, M.J. Marczewski, G. Kalinka, A.R.J. Kucernak, J. Scheers, M.S.P. Shaffer, J.H.G. Steinke, M. Wienrich, Structural supercapacitor electrolytes based on bicontinuous ionic liquid-epoxy resin systems, Journal of Materials Chemistry A 1 (2013) 15300–15309.
[29] A. Hess, G. Barber, C. Chen, T.E. Mallouk, H.R. Allcock, Organophosphates as solvents for electrolytes in electrochemical devices, ACS Applied Materials and Interfaces 5 (2013) 13029–13034.
[30] J.H. Jeon, R.K. Cheedarala, C.D. Kee, I.K. Oh, Dry-type artificial muscles based on pendent sulfonated chitosan and functionalized graphene oxide for greatly enhanced ionic interactions and mechanical stiffness, Advanced Functional Materials 23 (2013) 6007–6018.
[31] T. Ruther, K.R. Harris, M.D. Horne, M. Kanakubo, T. Rodopoulos, J.P. Veder, L.A. Woolf, Transport, electrochemical and thermophysical properties of two N-donor-functionalised ionic liquids, Chemistry - A European Journal 19 (2013) 17733–17744.
[32] D.S. Silvester, Recent advances in the use of ionic liquids for electrochemical sensing, Analyst 136 (2011) 4871–4882.
[33] Y. Kumar, S.A. Hashmi, G.P. Pandey, Lithium ion transport and ion-polymer interaction in PEO based polymer electrolyte plasticized with ionic liquid, Solid State Ionics 201 (2011) 73–80.
[34] J. Luo, J. Hu, W. Saak, R. Beckhaus, G. Wittstock, I.F.J. Vankelecom, C. Agert, O. Conrad, Protic ionic liquid and ionic melts prepared from methanesulfonic acid and 1H-1,2,4-triazole as high temperature PEMFC electrolytes, Journal of Materials Chemistry 21 (2011) 10426–10436.
[35] T. Enomoto, S. Kanematsu, K. Tsunashima, K. Matsumoto, R. Hagiwara, Physicochemical properties and plastic crystal structures of phosphonium fluorohydrogenate salts, Physical Chemistry Chemical Physics 13 (2011) 12536–12544.
[36] K. Tsunashima, S. Kodama, M. Sugiya, Y. Kunugi, Physical and electrochemical properties of room-temperature dicyanamide ionic liquids based on quaternary phosphonium cations, Electrochimica Acta 56 (2010) 762–766.
[37] Z.H. Li, Q.L. Xia, L.L. Liu, G.T. Lei, Q.Z. Xiao, D.S. Gao, X.D. Zhou, Effect of zwitterionic salt on the electrochemical properties of a solid polymer electrolyte with high temperature stability for lithium ion batteries, Electrochimica Acta 56 (2010) 804–809.
[38] X. Chen, H. Pan, H. Liu, M. Du, Nonenzymatic glucose sensor based on flower-shaped Au@Pd core-shell nanoparticles-ionic liquids composite film modified glassy carbon electrodes, Electrochimica Acta 56 (2010) 636–643.
[39] J. Huang, A.F. Hollenkamp, Thermal behavior of ionic liquids containing the FSI anion and the Li + cation, Journal of Physical Chemistry C 114 (2010) 21840–21847.
[40] L. Xi, D. Ren, J. Luo, Y. Zhu, Electrochemical analysis of ascorbic acid using copper nanoparticles/ polyaniline modified glassy carbon electrode, Journal of Electroanalytical Chemistry 650 (2010) 127–134.
[41] T.J. Abraham, D.R. Macfarlane, R.H. Baughman, L. Jin, N. Li, J.M. Pringle, Towards ionic liquid-based thermoelectrochemical cells for the harvesting of thermal energy, Electrochimica Acta 113 (2013) 87–93.
[42] P. Zhang, L. Hu, R. Lu, W. Zhou, H. Gao, Application of ionic liquids for liquid-liquid microextraction, Analytical Methods 5 (2013) 5376–5385.
[43] H. Li, J. Pang, Y. Yin, W. Zhuang, H. Wang, C. Zhai, S. Lu, Application of a nonflammable electrolyte containing Pp13TFSI ionic liquid for lithium-ion

batteries using the high capacity cathode material $Li[Li_{0.2}Mn_{0.54}Ni_{0.13}Co_{0.13}]O_2$, RSC Advances 3 (2013) 13907–13914.
[44] A.B. Pereiro, J.M.M. Araújo, S. Martinho, F. Alves, S. Nunes, A. Matias, C.M.M. Duarte, L.P.N. Rebelo, I.M. Marrucho, Fluorinated ionic liquids: Properties and applications, ACS Sustainable Chemistry and Engineering 1 (2013) 427–439.
[45] J. Zhang, S.S. Liu, H.L. Liu, Effect of ionic liquid on the toxicity of pesticide to Vibrio-qinghaiensis sp.-Q67, Journal of Hazardous Materials 170 (2009) 920–927.
[46] Y. Meng, V. Pino, J.L. Anderson, Exploiting the versatility of ionic liquids in separation science: Determination of low-volatility aliphatic hydrocarbons and fatty acid methyl esters using headspace solid-phase microextraction coupled to gas chromatography, Analytical Chemistry 81 (2009) 7107–7112.
[47] A. Sarkar, S. Trivedi, S. Pandey, Polymer molecular weight-dependent unusual fluorescence probe behavior within 1-butyl-3-methylimidazolium hexafluorophosphate$^+$ polyethylene glycol, Journal of Physical Chemistry B 113 (2009) 7606–7614.
[48] T.P.T. Pham, C.W. Cho, C.O. Jeon, Y.J. Chung, M.W. Lee, Y.S. Yun, Identification of metabolites involved in the biodegradation of the ionic liquid 1-butyl-3-methylpyridinium bromide by activated sludge microorganisms, Environmental Science and Technology 43 (2009) 516–521.
[49] M. Wang, M. Xu, D. Shi, R. Li, F. Gao, G. Zhang, Z. Yi, R. Humphry-Baker, P. Wang, S.M. Zakeeruddin, M. Gratzel, High-performance liquid and solid dye-sensitized solar cells based on a novel metal-free organic sensitizer, Advanced Materials 20 (2008) 4460–4463.
[50] J. Keskinen, E. Sivonen, S. Jussila, M. Bergelin, M. Johansson, A. Vaari, M. Smolander, Printed supercapacitors on paperboard substrate, Electrochimica Acta 85 (2012) 302–306.
[51] X. Xiao, T. Ding, L. Yuan, Y. Shen, Q. Zhong, X. Zhang, Y. Cao, B. Hu, T. Zhai, L. Gong, J. Chen, Y. Tong, J. Zhou, Z.L. Wang, WO_{3-x}/MoO_{3-x} core/shell nanowires on carbon fabric as an anode for all-solid-state asymmetric supercapacitors, Advanced Energy Materials 2 (2012) 1328–1332.
[52] M. Anouti, E. Couadou, L. Timperman, H. Galiano, Protic ionic liquid as electrolyte for high-densities electrochemical double layer capacitors with activated carbon electrode material, Electrochimica Acta 64 (2012) 110–117.
[53] R. Burt, G. Birkett, S. Zhao, A review of molecular modelling of electric double layer capacitors, Phys. Chem. Chem. Phys. 16 (2014) 6519–6538.
[54] Y.J. Lee, J. Lee, S. Kim, H.S. Park, Rendering high charge density of states in ionic liquid -gated MoS2 transistors, J. Phys. Chem. C 118 (2014) 18278.
[55] Z. Tang, L.E. Scriven, H.T. Davis, A three-component model of the electrical double layer, The Journal of Chemical Physics 97 (1992) 494.
[56] O. Pizio, S. Sokołowski, Z. Sokolowska, Electric double layer capacitance of restricted primitive model for an ionic fluid in slit-like nanopores: A density functional approach, Journal of Chemical Physics 137 (2012) 234705.
[57] P. Ballone, G. Pastore, M.P. Tosi, Restricted primitive model for electrical double layers: Modified HNC theory of density profiles and Monte Carlo study of differential capacitance, The Journal of Chemical Physics 85 (1986) 2943–2950.
[58] D. Henderson, S. Lamperski, L. Bari Bhuiyan, J. Wu, The tail effect on the shape of an electrical double layer differential capacitance curve, Journal of Chemical Physics 138 (2013) 144704.
[59] A.D. DeYoung, S.-W. Park, N.R. Dhumal, Y. Shim, Y.J. Jung, H.J. Kim, Graphene oxide supercapacitors: A Computer simulation study, J. Phys. Chem. C (2014), doi:http://dx.doi.org/10.1021/jp5072583 ASAP.
[60] K. Ma, C.E. Woodward, J. Forsman, Classical density functional study on interfacial structure and differential capacitance of ionic liquids near charged surfaces, J. Phys. Chem. C 118 (2014) 15825.
[61] S. Lamperski, J. Sosnowska, L.B. Bhuiyan, D. Henderson, Size asymmetric hard spheres as a convenient model for the capacitance of the electrical double layer of an ionic liquid, J. Chem. Phys. 140 (2014) 014704.
[62] Y.S. Han, S. Huang, T. Yan, A mean-field theory on the differential capacitance of asymmetric ionic liquid electrolytes, Journal of Physics: Condensed Matter 26 (284) (2014) 103.
[63] Q. Zhang, Y. Han, Y. Wang, S. Ye, T. Yan, Comparing the differential capacitance of two ionic liquid electrolytes: Effects of specific adsorption, Electrochemistry Communications 38 (2014) 44.
[64] J. Vatamanu, L. Cao, O. Borodin, D. Bedrov, G.D. Smith, On the influence of surface topography on the electric double layer structure and differential capacitance of graphite/ionic liquid interfaces, J. Phys. Chem. Lett. 2 (2011) 2267–2272.
[65] L. Xing, J. Vatamanu, G.D. Smith, D. Bedrov, Nanopatterning of electrode surfaces as a potential route to improve the energy density of electric double-layer capacitors: Insight from molecular simulations, J. Phys. Chem. Lett. 3 (2012) 1124–1129.
[66] T.A. Ho, A. Striolo, Capacitance enhancement via electrode patterning, J. Chem. Phys. 139 (2013) 204708.
[67] Y.Z. Su, Y.C. Fu, J.W. Yan, Z.B. Chen, B.W. Mao, Double layer of Au(100)/ionic liquid interface and its stability in imidazolium-based ionic liquids, Angew. Chem. Int. Ed. 48 (2009) 5148.
[68] R.T. Gore, T. Bond, W. Zhang, R.W.J. Scott, I.J. Burgess, Hysteresis in the measurement of double-layer capacitance at the gold–ionic liquid interface, Electrochem. Commun. 12 (2010) 1340–1343.
[69] Y. Su, J. Yan, M. Li, M. ZhanG, B. Mao, Electric double layer of Au(100)/imidazolium-based ionic liquids interface: Effect of cation size, J. Phys. Chem. C 117 (2013) 205–212.
[70] R. Atkin, N. Borisenko, M. Druschler, S.Z. El Abedin, F. Endres, R. Hayes, B. Huber, B. Roling, An in situ STM/AFM and impedance spectroscopy study of the extremely pure 1-butyl-1-methylpyrrolidinium tris(pentafluoroethyl) trifluorophosphate/Au(111) interface: Potential dependent solvation layers and the herringbone reconstruction, Phys. Chem. Chem. Phys 13 (2011) 6849.
[71] R. Hayes, N. Borisenko, M.K. Tam, P.C. Howlett, F. Endres, R. Atkin, Double layer structure of ionic liquids at the Au(111) electrode interface: An atomic force microscopy investigation, J. Phys. Chem. C 115 (2011) 6855.
[72] F. Endres, N. Borisenko, S.Z. El Abedin, R. Hayes, R. Atkin, The interface ionic liquid(s)/electrode(s): In situ STM and AFM measurements, Faraday Discuss 154 (2012) 221.
[73] J.I. Siepmann, M. Sprik, Influence of surface topology and electrostatic potential on water/electrode systems, J. Chem. Phys 102 (1995) 511.
[74] S.K. Reed, O.J. Lanning, P.A.J. Madden, Electrochemical interface between an ionic liquid and a model metallic electrode, Chem. Phys 126 (2007) 084704.
[75] J. Vatamanu, O. Borodin, G.D. Smith, Molecular dynamics simulations of atomically flat and nanoporous electrodes with a molten salt electrolyte, Phys. Chem. Chem. Phys. 12 (2010) 170–182.
[76] J. Vatamanu, O. Borodin, G.D. Smith, Molecular dynamics simulation studies of the structure of a mixed carbonate/LiPF 6 electrolyte near graphite surface as a function of electrode potential, J. Phys. Chem. C 116 (2012) 1114–1121.
[77] L. Xing, J. Vatamanu, O. Borodin, G.D. Smith, D. Bedrov, Electrode/electrolyte interface in sulfolane-based electrolytes for Li ion batteries: A molecular dynamics simulation study, J. Phys. Chem. C. 116 (2012) 23871–23881.
[78] M. Kawata, M. Mikami, Rapid calculation of two-dimensional Ewald summation, Chem. Phys. Lett. 340 (2001) 157–164.
[79] M. Kawata, U. Nagashima, Particle mesh Ewald method for three-dimensional systems with two-dimensional periodicity, Chem. Phys. Lett. 340 (2001) 165–172.
[80] M. Kawata, M. Mikami, U. Nagashima, Computationally efficient method to calculate the Coulomb interactions in three-dimensional systems with two-dimensional periodicity, J. Chem. Phys. 116 (2002) 3430.
[81] M. Kawata, M. Mikami, U. Nagashima, Comment on 'Rapid calculation of the Coulomb component of the stress tensor for three-dimensional systems with two-dimensional periodicity', J. Chem. Phys. 115 (2001) 4457.
[82] W.G. Hoover, Canonical dynamics: Equilibrium phase-space distributions, Phys. Rev. A 31 (1985) 1695–1697.
[83] G.J. Martyna, M.E. Tuckerman, D.J. Tobias, M.L. Klein, Explicit reversible integrators for extended system dynamics, Mol. Phys. 87 (1996) 1117–1157.
[84] T.R. Forester, W. Smith, Molecular simulations of the electric double layer structure, differential capacitance, and charging kinetics for N-methyl-N-propylpyrrolidinium bis(fluorosulfonyl)imide at graphite electrodes, J. Comput. Chem. 19 (1998) 102–111.
[85] J. Vatamanu, O. Borodin, D. Bedrov, G.D. Smith, Molecular dynamics simulation study of the interfacial structure and differential capacitance of alkylimidazolium bis(trifluoromethanesulfonyl)imide [Cnmim][TFSI] ionic liquids at graphite electrodes, J. Phys. Chem. C 116 (2012) 7940–7951.
[86] J. Vatamanu, O. Borodin, G.D. Smith, Molecular simulations of the electric double layer structure, differential capacitance, and charging kinetics for N-methyl-N-propylpyrrolidinium bis(fluorosulfonyl)imide at graphite electrodes, J. Phys. Chem. B 115 (2011) 3073–3084.
[87] O.J. Borodin, Polarizable force field development and molecular dynamics simulations of ionic liquids, Phys Chem. B 113 (2009) 11463–11478.
[88] S. Lamperski, C.W. Outhwaite, L.B. Bhuiyan, The electric double-layer differential capacitance at and near zero surface charge for a restricted primitive model electrolyte, J. Phys. Chem. B 113 (2009) 8925.
[89] J. Vatamanu, L. Xing, W. Li, D. Bedrov, Influence of temperature on the capacitance of ionic liquid electrolytes on charged surfaces, Phys. Chem. Chem. Phys. 16 (2014) 5174–5182.
[90] D. Bedrov, J. Vatamanu, Z. Hu, J. Ionic liquids at charged surfaces: Insight from molecular simulations, Non-Crystalline Solids (2014) . http://dx.doi.org/10.1016/j.jnoncrysol.2014.08.007.
[91] J. Vatamanu, O. Borodin, G.D. Smith, Molecular insights into the potential and temperature dependences of the differential capacitance of a room-temperature ionic liquid at graphite electrodes, J. Am. Chem. Soc. 132 (14) (2010) 825–14833.
[92] Z. Hu, J. Vatamanu, O. Borodin, D. Bedrov, A molecular dynamics simulation study of the electric double layer and capacitance of [BMIM][PF_6] and [BMIM][BF_4] room temperature ionic liquids near charged surfaces, Phys. Chem. Chem. Phys. 15 (2013) 14234–14247.
[93] C. Cannes, H. Cachet, C.D. Chouvy, C. Deslouis, J.D. Sanoit, C.L. Naour, V.A. Zinovyeva, Double layer at [BuMeIm][Tf2N] ionic liquid-Pt or-C material interfaces, J. Phys. Chem. C 117 (2013) 22915–22925.
[94] E. Uesugi, H. Goto, R. Eguchi, A. Fujiwara, Y. Kubozono, Electric double-layer capacitance between an ionic liquid and few-layer graphene, Nature (2014), doi:http://dx.doi.org/10.1038/srep01595.
[95] C. Merlet, M. Salanne, B. Rotenberg, New coarse-grained models of imidazolium ionic liquids for bulk and interfacial molecular simulations, J. Phys. Chem. C 116 (2012) 7687.
[96] X. Liu, Y. Han, T. Yan, Temperature effects on the capacitance of an imidazolium-based ionic liquid on a graphite electrode: A molecular dynamics simulation, ChemPhysChem (2014) , doi:http://dx.doi.org/10.1002/cphc.201402220 ASAP.
[97] N. Gregori, A.A. Kornyshev, M.V. Fedorov, The anatomy of the double layer and capacitance in ionic liquids with anisotropic ions: Electrostriction vs lattice saturation, J. Electroanal. Chem. 649 (2010) 261.
[98] D. Weingarth, A. Foelske-Schmitz, R. Kotz, Cycle versus voltage hold – Which is the better stability test for electrochemical double layer capacitors? Journal of Power Sources 225 (2013) 84–88.

[99] G. Raabe, J. Kohler, Thermodynamical and structural properties of imidazolium based ionic liquids from molecular simulation, J. Chem. Phys 128 (2008) 154509.
[100] S. Zhang, N. Sun, X. He, X. Lu, X. Zhang, Physical properties of ionic liquids: Database and evaluation, J. Phys. Chem. Ref. Data 35 (2006) 1475.
[101] V. Ivanistsev, M. Fedorov, Interfaces between charged surfaces and ionic liquids: Insights from molecular simulations, The Electrochemical Society Interface 23 (2014) 65–69.
[102] M. Mezger, H. Schroder, H. Reichert, S. Schramm, J.S. Okasinski, S. Schooder, V. Honkimaki, M. Deutsch, B.M. Ocko, J. Ralston, M. Rohwerder, M. Stratmann, H. Dosch, Molecular layering of fluorinated ionic liquids at a charged sapphire (0001) surface, Science 322 (2008) 424.
[103] M. Mezger, B.M. Ocko, H. Reichert, M. Deutsch, Temperature dependence of multilayering at the free surface of ionic liquids probed by X-ray reflectivity measurements, Proc. Natl. Acad. Sci. U.S.A. 110 (2013) 3733.
[104] N. Nishi, T. Uruga, H. Tanida, T. Kakiuchi, Temperature dependence of multilayering at the free surface of ionic liquids probed by X-ray reflectivity measurements, Langmuir 27 (2011) 7531.
[105] R. Hayes, N. Borisenko, M.K. Tam, P.C. Howlett, F. Endres, R.J. Atkin, Double layer structure of ionic liquids at the Au(111) electrode interface: An atomic force microscopy investigation, Phys. Chem. C 115 (2011) 6855.
[106] A.M. Smith, K.R.J. Lovelock, N.N. Gosvami, P. Licence, A. Dolan, T. Welton, S.J. Perkin, Monolayer to bilayer structural transition in confined pyrrolidinium-based ionic liquids, Phys. Chem. Lett. 4 (2013) 378–382.
[107] S. Bhuiyan, J. Wu, D. Henderson, Monte Carlo simulation for the double layer structure of an ionic liquid using a dimer model: A comparison with the density functional theory, J. Phys. Chem. B 116 (10) (2012) 364–10370.
[108] S. Woelki, H.K. Kohler, H. Krienke, A singlet-RISM theory for solid/liquid interfaces part I: Uncharged walls, J. Phys. Chem. B 111 (2007) 13386–13397.
[109] J.J. Howard, J.S. Perkyns, B.M. Pettitt, The behavior of ions near a charged wall-dependence on ion size, concentration, and surface charge, J. Phys. Chem. B 114 (2010) 6074–6083.
[110] G.I. Guerrero-Garcia, E. Gonzalez-Tovar, M. Chavez-Paez, M. Lozada-Cassou, Overcharging and charge reversal in the electrical double layer around the point of zero charge, J. Chem. Phys 132 (2010) 054903.
[111] M.V. Fedorov, A.A. Kornyshev, Towards understanding the structure and capacitance of electrical double layer in ionic liquids, Electrochim. Acta 53 (2008) 6835.
[112] S. Baldelli, Surface structure at the ionic liquid-electrified metal interfac, Acc. Chem. Res 41 (2008) 421.
[113] S. Perkin, L. Crowhurst, H. Niedermeyer, T. Welton, A.M. Smith, N.N. Gosvami, Self-assembly in the electrical double layer of ionic liquids, Chem. Commun. 47 (2011) 6572–6574.
[114] R.M. Lynden-Bell, A.I. Frolov, M.V. Fedorov, Electrode screening by ionic liquids, Phys. Chem. Chem. Phys. 14 (2012) 2693–2701.
[115] M.Z. Bazant, B.D. Storey, A.A. Kornyshev, Double layer in ionic liquids: Overscreening versus crowding, Phys. Rev. Lett 106 (2011) 046102.
[116] A.A. Kornyshev, Double-layer in ionic liquids: Paradigm change? J. Phys. Chem. B 111 (2007) 5545–5557.
[117] K.B. Oldham, A Gouy-Chapman-Stern model of the double layer at a (metal)/(ionic liquid) interface, J. Electro Anal. Chem 131 (613) (2008) .

CHAPTER 5

CONCLUSION OF MD SIMULATION ON SUPERCAPACITORS

A computational low-cost and efficient united atom/explicit atom force field was utilized. MD simulation has been conducted on various Electric Double Layer Capacitor (EDLC) systems with varying Room Temperature Ionic Liquids (RTILs) as well as different structures and materials of electrodes. A comparative MD simulation study of the EDL structure and DC as a function of electrode potential was conducted for [BMIM][BF_4] and [BMIM][PF_6] on basal, prismatic graphite as well as Au (001) and Au (011) surfaces. The DC of these two electrolytes on basal graphite are very similar, and more variations were observed on the Au (001) surface. Different topography of gold surfaces did not change significantly the DC for [BMIM][BF_4] system. However, different topography of graphite surfaces gave two very different DCs. The variations of DC simulated by us are 4 to 8 μF cm^{-2}, and no large DC (up to 25 μF cm^{-2}) was observed in our studies. Also, the effect of possible chemisorption of the anion on the electrode surface has been investigated. With strong absorption of the anion, a bell-shaped DC was observed. However, without chemisorption it was U-shaped near PZC. Meanwhile DC's position shift and value changed slightly as well.

The structures of electrodes also have a strong effect on the capacitance of EDLCs. MD simulation has been conducted on similar RTILs of N-methyl-N- propylpyrrolidinium [pyr_{13}] and bis(trifluoromethylsulfonyl)imide (TFSI), as well as [BMIM][PF_6] on both curvature electrodes (fullerenes, nanotube, nanowire) and atomic flat electrode surfaces, and the correlations between their corresponding integral capacitance (IC) and integral charge densities was demonstrated. Nanowire electrode systems have the largest capacitance, followed by fullerene systems. Nanotube electrode systems have the smallest capacitance among curvature systems, but they are still larger than that of atomic flat electrode systems.

A systematic comparative study of DC and the EDL structure formed near atomically flat and corrugated surfaces with two similar series of electrolytes: [$C_n$mim][FSI] and [$C_n$mim][TFSI] (n = 2, 4, 6, 8) was conducted using MD simulation. The effect of the length

of the alkyl tail and different anions has been examined. On atomically flat surfaces, we observed very weak, almost constant DC depending on electrode potential for all electrolytes with different lengths of alkyl tails and anions. However, on the rough surfaces of the DC of FSI anion systems, there shows a bell-shaped DC for RTILs with cations with alkyl tail lengths of n = 2, 4, and then it transitions to camel-shaped DCs for cations with longer alkyl tails, n = 6, 8. However, RTILs with the TFSI anion have camel-shaped curves for all systems. To better understand the correlations between EDL structures and shapes of DC, the cumulative charge densities inside EDLs were calculated. Detailed explanations regarding electrode accumulation have been demonstrated as well as over screening phenomenon at low voltages.